Impact Analysis and Design Development for Air-Dropped Antarctic Seismo-Geodetic Ice Penetrator

by

Alex S. Miller

S.B., Physics and Electrical Engineering and Computer Science,
Massachusetts Institute of Technology (2021)

Submitted to the Department of Aeronautics and Astronautics
in partial fulfillment of the requirements for the degree of

Master of Science in Aeronautics and Astronautics

at the

MASSACHUSETTS INSTITUTE OF TECHNOLOGY

June 2023

© Alex S. Miller, MMXXIII. All rights reserved.

The author hereby grants to MIT permission to reproduce and to distribute publicly paper and electronic copies of this thesis document in whole or in part in any medium now known or hereafter created.

Authored by: Alex S. Miller
Department of Aeronautics and Astronautics
May 23, 2023

Certified by:
Jeffrey A. Hoffman
Professor of the Practice
Thesis Supervisor

Accepted by:
Jonathan P. How
Professor of Aeronautics and Astronautics
Graduate Committee Chair

Impact Analysis and Design Development for Air-Dropped Antarctic Seismo-Geodetic Ice Penetrator

by

Alex S. Miller

Submitted to the Department of Aeronautics and Astronautics
on May 23, 2023, in partial fulfillment of the
requirements for the degree of
Master of Science in Aeronautics and Astronautics

Abstract

Existing measurement tools for ice shelves and other glaciated regions have limited capability to measure dynamic events in remote areas. The Seismo-Geodetic Ice Penetrator (SGIP) offers a method for rapid deployment of a broadband seismometer and Global Navigation Satellite System (GNSS) positioning system designed to sense ice shelf resonant forcings caused by ocean gravity waves and atmospheric waves. Additionally, SGIP will track seismic indications of calving and rifting, facilitating better estimates of sea level rise. During operation, SGIP is dropped from an aerial vehicle, reaching a terminal velocity of 42 $\mathrm{m\,s^{-1}}$; during impact with the snowpack surface SGIP experiences an average acceleration of approximately 500 $\mathrm{m\,s^{-2}}$. Upon impact, a fore-body section separates from the upper aft-body "flare" section and continues several meters into the ice shelf, while the aft-body remains at the surface with a set of communications antennas. The SGIP platform is compared to previously envisioned and tested penetrator systems. Impact modeling of SGIP into glacial firn is detailed, with a focus on fast simulation run-times for design exploration. Designs of snow spikes and a rigid antenna mast are detailed, analyzed and tested. Results from a full-scale prototype hardware test in Juneau, Alaska are discussed.

Thesis Supervisor: Jeffrey A. Hoffman
Title: Professor of the Practice

Acknowledgments

Thank you to Prof. Jeffrey Hoffman for advising this thesis work, providing guidance, thoughtful systems design comments, astronaut stories and detailed writing feedback on this thesis.

Thank you to Mike Brown for designing the drop test experiments in this thesis, collecting drop test data which are presented and contextualized here and providing feedback on models and experiment design. Thank you to Aaron Makikalli for designing the SGIP full system wind tunnel experiment on the scale penetrator model and for wonderful brainstorming sessions. Thank you to Cesar Meza for designing and building the small drop test model, and to Yatin Chandar for brainstorming about the SGIP antenna mast and designing and building the wind tunnel scale model penetrator. Thank you to Dhiman Mondal for compiling the antenna performance data. Beyond technical contributions to this thesis, thank you to Mike and Aaron for the fun after-work hangouts and bonding at the climbing gym.

Thank you to the Haystack-MIT SGIP, including Chris Eckert for mentoring me about mechanical design, as well as Parker Steen, Pedro Elosegui, Dhiman Mondal, Chester Ruszczyk and John Glover. Thank you to Dan Poe and Charlotte Lowey for setting the stage for this work. Thank you to Jeffrey Hoffman, Pedro Elosegui, Rachel Miller and Corrina Wycoff for comments on a draft of this work.

Thank you for my parents Rachel Miller and Stephen Miller for their unwavering support through every part of my academic and personal journey and encouraging me through messy engineering projects at home. Thank you to Miriam and Peter Selig, and Margaret and Donald Miller as well for their encouragement. Thank you to Quimby, Pekoe and Jazz!

Thank you to Nicolas Orndorff and Clara Orndorff for learning with me while designing, building and testing ROVs on AMNO & CO. Thank you to Rick Rupan, Fritz Stahr, Wes Thompson and Jill Zande for organizing the MATE ROV competition and providing many years of inspiration. Thank you to Martin Klein for always asking how we can make things better.

Thank you to my internship and professional mentors including Trevor Shannon, Andre Prager, Doug Patterson, Martin Garthwaite, Emre Karagozler, Gerik Kubiak, Artem Goncharuk and Kevin Smith.

Thank you to the undergraduate professors and instructors who guided my learning including advisors Prof. Joel Voldman and Prof. Yen-Jie Lee as well as Christian Cardozo, Paola Rebusco, Jeremy Orloff, Prof. Marcus Thompson, Prof. Sara Seager, Prof. Steven Leeb, Prof. Chris Terman, and Prof. Vladan Vuletic.

Thank you to many primary and secondary school teachers who were instrumental to my academic journey thus far including but not limited to Mr. Clark, Mrs. Miller (no relation), Mr. Beal, Mr. Wood, Mr. Schilperoort, Ms. Zoog, Dr. Dunlap. Mr. Miller (no relation), Mr. NK, Mr. Tsutakawa, Mr. Stever and Mr. Shaw. Thank you to Peter Williams.

Thank you to the communities and friends who have supported me and been wonderful friends over the past several years in university and graduate school, including but not limited to Avi B., Dahlia D., Joe S., Oomi P., Skylar J., Sharon L., Alex K., H. Powers, Oomi P., Jack R., Alejandro D., Annie W., Rujul G., Hope D., Sophia D-G., Christina L., Marla O., Ciara M., Olivia B.R., Mira S., and Constantin A. I would also like to extend a warm thank you to many older friends including Aileen Z., Tiffany S., Isabella d. L., Brock F., Neva O., Simone L., Nicole B., Sophia T., Anna Z., Leah Z., Anna G., Alice T. and William L.

Thank you to the Fannie and John Hertz foundation for funding and community. This material is also based upon work supported by the National Science Foundation (NSF) Award No. 1931131 "A New Instrument and Measurement Approach to Cryo-Seismogeodesy: Monitoring Antarctic Ice Shelf Stability Using Ice Penetrators." and the NSF Graduate Research Fellowship under Grant No. 2141064.

Contents

1 Introduction **21**

1.1 Non-Technical Summary 21

1.2 Motivation 21

1.3 Background 24

1.3.1 History of Penetrators 24

1.3.2 Research Use Statement 26

1.3.3 Designing a Seismo-Geodetic Ice Penetrator 27

2 Impact Mechanics and Testing **33**

2.1 Motivation and Background 33

2.2 Modeling Inputs 36

2.2.1 Penetrator Sizing 36

2.2.2 Density Profiles 37

2.3 Modeling Workflow 38

2.4 Drop Testing 40

2.4.1 Small Scale Drop Testing 40

2.5 Simple Numerical Models 41

2.5.1 Simple Young Model 41

2.5.2 Compaction Model 43

2.6 Finite Element Models 55

2.6.1 Small Scale Model 55

2.6.2 Full Scale Model 56

2.7 Full Scale Testing at Juneau Icefield 57

2.7.1 First Test . . . 58
2.7.2 Second Test . . . 59
2.8 Conclusions and Discussion . . . 61

3 Design, Analysis and Testing of Antenna Mast for Ice Penetrator 69
3.1 Design of Antenna Mast . . . 69
3.1.1 Motivation . . . 69
3.1.2 Prototype Mast Design, Detailed . . . 70
3.1.3 Previous Design Iterations of Static Mast . . . 75
3.2 Analysis of Static Mast . . . 78
3.2.1 Buckling Calculations: Axial Loads . . . 79
3.2.2 Radial Loads . . . 82
3.2.3 Aerodynamics . . . 83
3.3 Manufacturing and Assembly . . . 86
3.3.1 Fit checks and Assembly . . . 86
3.3.2 Procurement of fiberglass tubing . . . 87
3.4 Testing . . . 88
3.4.1 Water Absorption Testing . . . 88
3.4.2 Lanyard Retraction Testing . . . 91
3.4.3 Aerodynamic Testing . . . 91
3.4.4 Radio Frequency Interference Testing . . . 98
3.4.5 Juneau Full-Scale Testing . . . 99
3.5 Proposed Design Changes After Field Testing . . . 99
3.6 Conclusions . . . 100

4 Design and Construction of Snow Spikes 101
4.1 Introduction and Snow Spike Requirements . . . 101
4.2 Design of Snow Spikes . . . 103
4.3 Testing of Snow Spikes . . . 104
4.3.1 Snow Density Measurement . . . 105
4.3.2 Experimental Procedure for Snow Spike Test . . . 106

4.3.3 Aerodynamics of Snow Spikes with SGIP System 108
4.3.4 Snow Spike Field Test Results 109
4.4 As-built Snow Spike Design for Alaska 115
4.5 Conclusions 116

5 Discussion and Conclusions **119**
5.1 Conclusions 119
5.2 Discussion 119
5.2.1 Minimum SGIP path to Antarctica 119
5.2.2 Proposed System Design Changes 120

A Small Drop Test Plots **123**

B Resources **131**

List of Figures

1-1 (a) The Ross Ice Shelf (RIS) [53]. (b) Ice shelves are subject to resonant forcings from atmospheric waves and ocean gravity waves [47]. Due to the timescales too fast for satellite data and sparse in-situ sensors, these forcings are poorly understood. 23

1-2 Concept of operations of air-dropped ice penetrator. SGIP is dropped out of a helicopter, reaches a terminal velocity of 42 $\mathrm{m\,s^{-1}}$ and hits an ice shelf, causing the fore-body and aft-body to separate. 29

1-3 As-built full-size prototype of the Seismo-Geodetic Ice Penetrator (SGIP). 30

1-4 Pictures of prototyped SGIP subassemblies including (a) battery pack unit. (b) battery cell rack with battery-weight-equivalent steel plates installed for initial structural testing. (c) top plate of sealed fore-body section. (d) top-view of aft-body with top plate removed, showing coiled umbilical cable. (e) angled view of aft-body, showing adaptable aerodynamic plate which can be size-selected for surface firn conditions. 31

2-1 Key measurements of simplified penetrator geometry. 37

2-2 Snow and firn density profiles used for modeling SGIP impact. 39

2-3 Model workflow for SGIP impact studies. 39

2-4 Small-scale model, 0.025 m radius, 2.1 kg mass, penetrator used for drop testing. An interior 3-axis accelerometer measures impacts and is easily removable in the field with thumbscrews on the top. 40

2-5 Example drop test data referencing to Table 2.2. Complete data are in Appendix A. Acceleration profiles are filtered with a 20 Hz low-pass filter in solid colors for clarity, with the original in the background. . 42

2-6 Density profiles measured in small drop tests detailed in Table 2.2, calculated by measuring the mass of a known volume. For the indoor drop tests 1—10, this plot shows an example profile for drop 3 to compare with the other snow packs; each drop had its own measurement reading as noted in Table 2.2. 43

2-7 Example of Young Equation (2.1) applied to as-built SGIP model tested in Juneau with drop velocity of 42 $\mathrm{m\,s^{-1}}$ over a range of S values (a) with only the fore-body section. (b) with both the fore-body and the fore-body bonded to the aft-body "flare". Note the significant increase in acceleration which occurs upon the flare impact, after which the fore-body-only models continue into the snow. 44

2-8 Compaction model features an infinite grid of 1D elastic elements with modulus E that depends nonlinearly on the material density. 45

2-9 Flowchart describing a nonlinear compaction model. 46

2-10 Comparison of small drop test parameters which are listed in Table 2.2 between drops 4, 17 and 26, each in a different snow pack. Note that dense slush in drop 4 has a significant underestimate in penetration distance, likely due to the different mode of energy absorption involved. 53

2-11 Impact performance comparison of the SGIP design analyzed by Poe with the as-built prototype with an impact velocity of 42 $\mathrm{m\,s^{-1}}$ on Ross Ice Shelf and Taku Glacier profiles. (a) Shows a simulation with only the fore-body. (b) Shows a simulation with the aft-body bonded to the fore-body. 54

2-12 Comparison of impact conditions of the as-built SGIP prototype at a variety of impact velocities using nonlinear compaction model in the Taku Glacier with (a) only the fore-body. (b) the fore-body bonded to the aft-body. 54

2-13 Small-scale three-dimensional finite element analysis model, with around 15k nodes, and dimensions matching the small-scale penetrator with paint bucket impact enclosure. This simulation shows an animation of drop 26, in Table 2.3, at times (a) 0 s, (b) 0.02 s, (c) 0.04 s, (d) 0.06 s. 56

2-14 Full-scale three-dimensional finite element analysis model, with around 100k nodes. This simulation shows the as-built SGIP prototype impacting firn with the flare bonded to the fore-body to inform shear pin sizing at (a) 0 s, (b) 0.02 s, (c) 0.05 s, (d) 0.08 s. 57

2-15 Orientation profile for SGIP entire prototype drop 5/10/2023 test drop onto the Taku Glacier, Juneau Icefield. The penetrator experienced axial roll rotation around 1 Hz for the last 27 s of the drop, with significant yaw and pitch oscillations. 59

2-16 Acceleration profiles (a) and orientation (b) of SGIP during first full-scale prototype test drop on Juneau Icefield 5/10/2023. The $t = 0$ point in both plots corresponds to when the penetrator made contact with the surface. Acceleration profile in (a) is filtered with a 20 Hz low-pass filter in solid colors for clarity, with the original in the background. 63

2-17 Images from 5/10/2023 first test drop onto the Taku Glacier, Juneau Icefield. 64

2-18 Snow and firn density profiles used for modeling SGIP impact with measured snow density from SGIP drop testing on Taku Glacier 2023. 65

2-19 Nonlinear compaction model run on the measured profiles on from the SGIP Taku Glacier shown in Figure 2-18 at an initial velocity of 42 $\mathrm{m\,s^{-1}}$ in comparison to the generic profile of the Taku Glacier (a) with only the fore-body section. (b) with both the fore-body and the fore-body bonded to the aft-body "flare". 66

2-20 Images from drop stage of the 5/16/2023 second test drop onto the Taku Glacier, Juneau Icefield. SGIP experienced a 0.25 – 0.5 Hz oscillation in pitch and yaw during the drop at a maximum amplitude of 20 °, which dampened over the first 30 s to < 5 °. Images (b) – (f) were taken at the maximum amplitude of oscillation during each time of the drop, showing the dampening effect. 67

2-21 Images from 5/16/2023 second test drop onto the Taku Glacier, Juneau Icefield. 68

3-1 SGIP antenna mast design pictured in an angled view with major components labeled. 71

3-2 Top tubular interface joint design featuring a ridged gluing interface, captive nut interfaces to the payload deck and holes for rivets to be used during assembly. 75

3-3 Top view of SGIP antenna mast featuring GNSS antenna, Iridium antenna and guide pole. 76

3-4 Closeup (a) of interior payload deck structure (b), showing corner braces, GNSS mounting, holes for wire routing and chamfered guide for helicopter lanyard. 76

3-5 Pre-PDR version 1 of SGIP antenna mast, featuring antenna radome. The mast was redesigned to have less area for snow accumulation and a more rigid upper boundary condition. 78

3-6 Buckling modes of as-built SGIP antenna mast when subjected to representative force distribution. Displacements are scaled up for illustrative purposes. 82

3-7 Buckling modes of V1 (PDR) SGIP antenna mast when subjected to representative force distribution. Displacements are scaled up for illustrative purposes. 82

3-8 Buckling modes of SGIP antenna mast when subjected to representative force distribution. Note that negative mode force values occur with forcing in the opposite direction of the applied force shown in (e). Displacements are scaled up for illustrative purposes. 84
3-9 Set of nylon tube joints manufactured for the SGIP mast with standardized adhesive interface. 87
3-10 Nylon tube joints before and after sanding. Sanding causes limited surface melting, but leaves a surface texture that is still rough and porous, thus appropriate for gluing. 88
3-11 A mock flare interface constructed for fixturing and assembly. 89
3-12 Cable structures installed on the SGIP antenna mast. (a) Bottom cable structures including anchor, thimble turnbuckle and saddle clamps. (b) Top cable structure including anchor, shackle, thimble and saddle clamps. 89
3-13 (a) Temporary surface staining from water on a Nylon 12 multijet fusion part; this staining evaporates on the order of 20 minutes. (b) Water absorption of nylon parts was tested by soaking parts. 91
3-14 Lanyard passing through guide pole during test. 92
3-15 Fixturing for the SGIP mast to the wind tunnel force measurement stand, showing the machined standoffs. 93
3-16 Arrangements of SGIP mast in the wind tunnel, showing coordinate systems, with the wind in the +X direction and the mast at angles (a) -30 deg. (b) 0 deg. (c) +30 deg. The mast can be adjusted within this angular range using the wind tunnel servo motors. 93
3-17 SGIP antenna mast in MIT Wright Brothers Wind Tunnel for aerodynamics testing. 94
3-18 Drag force data from wind tunnel test where (a) frag force increases linearly with dynamic pressure. (b) Drag force varies with azimuth angle within a 40 N range. 95
3-19 Data from wind tunnel testing of SGIP antenna mast showing (a) normal force. (b) side force. (c) yaw moment. 96

3-20 Free body diagram showing the mast with the relevant coordinate systems for calculating wind moments on the SGIP antenna mast and aft-body flare, side view. 97

3-21 Data from GNSS antenna testing on (a) 12/07/2022 and (b) 12/08/2022 without a microwave absober. (c) 12/10/2022 and (d) 12/11/2022 with a added microwave absorbent material below the GNSS antenna. 98

3-22 SGIP antenna mast after first prototype deployment on the Juneau Ice Field with an angled impact of around 15 °with an acceleration profile on the nose shown in Figure 2-16. Shear loads were much higher expected and caused (a, b, c) fracture on the MJF bottom components both at the site of the fiberglass tubes and the fastener holes. (d) bending of the antenna support mount. The structure was kept held down by the cable structures. The top MJF parts, fiberglass tubes and the payload deck were all intact. 100

4-1 Free body diagram depicting wind force on SGIP mast, with torques defined on around the pivot. 102

4-2 (a) Tubular snow spike design with a straight tip. (b) Tubular snow spike design with a large conical tip. (c) Bent sheet metal snow spike design. 105

4-3 Custom-made snow scoop for measuring snow density. 106

4-4 Illustration of the density measurement during field testing. (a) A sample is taken from the snow pack at the desired depth. (b) Alternatively a sample may be taken from the surface. (c) A plastic scraper is used to remove excess snow from the measurement scoop. (d) The sample is weighed using a scale. 106

4-5 Testing snow spikes with a digital force gauge. (a) Insertion testing with the force gauge used to drive the spike into the snow. (b) Sideways pull testing with a 0.91 m lever arm. (c) Vertical pull testing, lifting the spike out of the snow. 107
4-6 Scale model (0.41x) of SGIP used for testing aerodynamic stability in the wind tunnel. (a) Full assembly. (b) Scaled spike model. 108
4-7 Wind tunnel data taken on 5/12/2023 of a scale-model SGIP prototype with and without snow spikes. Data are scaled to the full-scale prototype. (a) Drag force varies linearly with dynamic pressure. (b) Higher yaw (beta) angles lead to higher drag force. (c) Roll moments with and without snow spikes trend in the opposite direction, but are both very low in magnitude. (d) Yaw moments increase with yaw angle. 110
4-8 Test of snow spike design with large conical tip, shown in Figure 4-2 (b), where only minimal backfill was observed. 111
4-9 Free body diagram illustrating the snow spikes and attached lever arms used to conduct force and moment tests in the field. Static equations are defined around the pivot shown. 114
4-10 As-built snow spike design featuring additional detachable interface used in Alaska drop tests. 117

A-1 Example drop test data referencing to Table 2.2. 124
A-2 Example drop test data referencing to Table 2.2. 125
A-3 Example drop test data referencing to Table 2.2. 126
A-4 Example drop test data referencing to Table 2.2. 127
A-5 Example drop test data referencing to Table 2.2. 128
A-6 Example drop test data referencing to Table 2.2. 129

List of Tables

2.1 Dimensions of penetrator models considered in impact simulation. The symbol ** denotes that measurements were taken at the top of the conical flare section, not including the full aerodynamic structure. . . 37

2.2 Test drops of small model penetrator into snow. Rows with ** denote tests that punched through the snowpack and hit frozen soil. 42

2.3 Finite element model results in comparison to drop test data. Note that a similar distance traveled by the penetrator indicates a similar average acceleration. The discrepancies on drops 1 – 10 are likely due to significantly slushier snow compared to the material parameters in the FEA model. 56

3.1 Specification for SGIP antenna mast with corresponding driving requirements. 72

3.2 Relevant Requirements for SGIP Antenna Mast. 73

3.3 Interfaces for SGIP Antenna Mast 77

4.1 Requirements for SGIP snow spikes. 104

4.2 Insertion force testing of snow spikes. 111

4.3 Shear force testing of snow spikes. 112

4.4 Removal testing of snow spikes. 113

4.5 Margin calculations for SGIP snow spikes, assuming 0.5 m radius from center of flare to structural tipping point. 116

Chapter 1

Introduction

1.1 Non-Technical Summary

In Antarctica, where a glacier meets the ocean, it forms a massive sheet of floating ice called an ice shelf. Ice shelves are flexible like springboards, and can crack and break under stress. As the planet heats up, ice shelves are breaking more frequently. This affects how much the sea level will rise in the future. Ice shelves also respond to the forces of ocean waves and atmospheric pressure waves, but these movements are too fast for satellites to capture.

To measure these movements, we need to place seismometers on ice shelves. But walking on ice shelves is difficult and dangerous, so we developed a method to drop seismometers from a helicopter into the ice shelves.

This thesis explains our research into how these seismometers hit ice shelves, how we designed an antenna tower to get data from the seismometer, how we used snow spikes to keep the antenna tower stable in the wind, and what we learned from a trial drop in Alaska.

1.2 Motivation

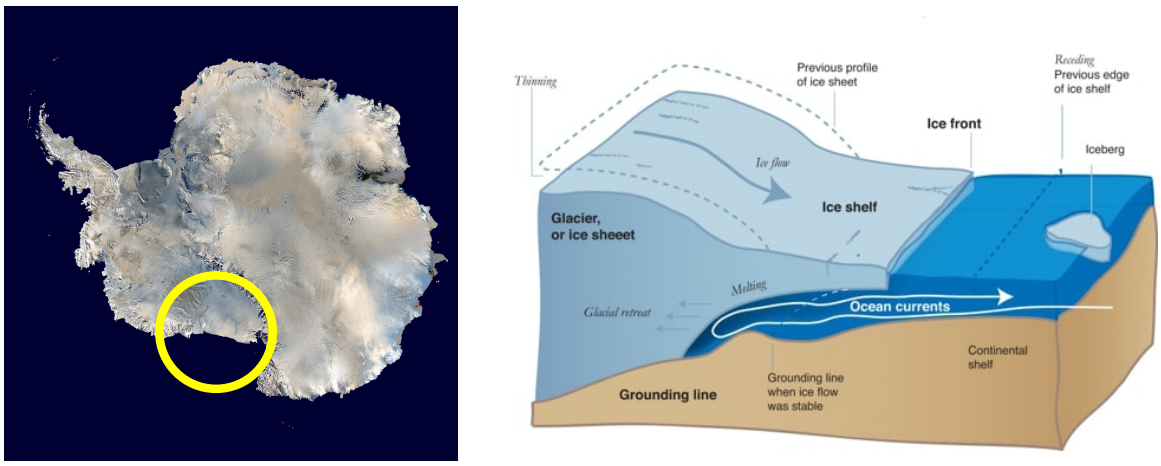
Although glaciers and ice shelves cover >10 % of Earth's land surface, current geophysical glacial dynamics data are limited [9]. Ice shelves, such as the Ross Ice

Shelf (RIS) shown in Figure 1-1 (a), experience resonant forcings from atmospheric events, ocean gravity waves, and ocean swells [8][11][49][14]. Additionally dynamic events such as calving and ice shelf collapse can occur on time scales on the order of days, with seismic content observable to the order of 1 — 30 Hz[31]. These waves may interact nonlinearly with the ice shelf itself as well as the resonant cavity under the ice shelf which stretches to the grounding line, depicted in Figure 1-1 (b). Understanding these resonant forcings is critical to modeling the dynamic behavior of ice shelves, since the ice shelf behavior during forcings may be used to construct more accurate models of ice shelf mechanics [49]. By better understanding resonant forcings, calving and other dynamic events, the structure of ice shelves may be better modeled, leading to better estimates of sea level rise.

Long timescale phenomena such as ice flow and slower rifting events may be measured through remote sensing techniques including synthetic aperture radar (SAR) and satellite image correlation techniques as well as in-situ Global Navigation Satellite System (GNSS) receivers [33][45]. Temporal resolution of satellite-based techniques is limited by the number of satellite passes, which is on the order of <10 per day; in-situ GNSS techniques are limited by averaging durations too long to observe dynamic events.

For events such as calving that may be seen from aerial imaging, continuous-flying solar-powered aerial systems are being investigated to provide more frequent SAR passes, providing a middle-ground between in-situ sensing and satellite systems [41][20]. Major research stations such as McMurdo and Amundsen-Scott have more permanent seismometers nearby, but the density of seismic data on crevassed areas more prone to dynamic events is limited by difficulty of deployment [44]. Recently, fiber optic Distributed Acoustic Sensing (DAS) has also been demonstrated on both alpine glaciers and on the Antarctic, but the expense, difficulties of deployment and high volumes of data have limited reach to near research stations [25] [56].

For short timescale phenomena such as resonant forcings and seismic events during calving, a substantial amount of work has been done in modeling, with more limited in-situ observation [27] [49]. Seismometry efforts in ice shelves have been increasing,



(a) (b)

Figure 1-1: (a) The Ross Ice Shelf (RIS) [53]. (b) Ice shelves are subject to resonant forcings from atmospheric waves and ocean gravity waves [47]. Due to the timescales too fast for satellite data and sparse in-situ sensors, these forcings are poorly understood.

but are limited in sensor density, especially in heavily crevassed and hard to access areas. Prior seismic arrays have been on the order of tens of sensors [13] [15]. Prior observation has found significant interactions with wind (5 — 25 Hz) [14], swell-triggered seismicity (0.5 — 20 Hz) [8], swell-induced motion (0.025 — 0.14 Hz) [13] and interactions with ocean gravity waves (0.0001 — 0.01 Hz). Most of these observations have been from the past decade, with minimal temporal baseline; by increasing the temporal baseline of these measurements over a greater density, better models can be constructed of ice shelf dynamics.

To address this data gap, MIT and Haystack Obervatory have formed the seismo-geodetic ice penetrator project (SGIP), which is an air-dropped system to deliver a broadband seismometer to glaciated areas and ice shelves. An air-dropped system may be used to reach areas which are conducive to land travel due to crevasses or instability. Additionally, future versions of SGIP may be mass-produced to facilitate unprecedented in-situ sensor coverage of glaciated regions. SGIP is designed for a first scientific deployment on the Ross Ice Shelf (RIS), but may be adapted for use on other ice shelves and glaciated areas. The first prototype of SGIP was tested

on the Juneau Icefield in May 2023 in preparation for RIS deployment in 2024.

1.3 Background

1.3.1 History of Penetrators

Development and study of air-dropped penetrators began for military applications, such as ballistics into soil, cement and other building materials. As reviewed by Lorenz [36], during WWII, this manifested into weapons which were designed to penetrate through structures and create significant seismic disturbance; these "Earthquake Bombs" such as the 10160 kg "Grand Slam" had dimensions specifically tailored to their respective target material. Militaries kept advancing research into the late 20^{th} century for deeply penetrating bombs such as the GBU-28. The first wide-spread penetrator-based sensor system was the "Igloo White" project which deployed a fleet of seismometers during the Vietnam War. These Air-Delivered Seismic Intrusion Detector (ADSID) units included a battery, radio transmitter and microphone. A package size of 1.3 m and 20 kg, these units had deployable aerodynamic drag fins and antenna structures that unfurled during the drop [36].

Starting in the 1970's, NASA began concept studies and development of instrumented penetrators for planetary environments. Mars presents an opportune target for penetrator missions since the atmosphere with density around 0.2 $\mathrm{kg\,m^{-3}}$ is thick enough to significantly slow down the penetrator, while thin enough to avoid serious thermal issues. In contrast, the thicker atmospheres of Venus and Saturn's moon Titan, at approximately 65 $\mathrm{kg\,m^{-3}}$ and at 10 $\mathrm{kg\,m^{-3}}$ respectively, have been shown to slow penetrators too much before impact and to cause rapid thermal changes [21][32]. Although many Mars penetrator concepts were developed, the first major flight vehicle development effort was for the Russian Mars-96 mission, which consisted of two 120 kg units with a significant inflatable "ballute" aft-body to slow the impacter from 1372 $\mathrm{m\,s^{-1}}$ to the designed impact speed of 60 — 80$\mathrm{m\,s^{-1}}$. Upon impact, a small fore-body containing a seismometer, neutron detector and

X-ray spectrometer was to detach from the aft-body. Like on Earth, wind noise is the most significant source of seismic noise on Mars; thus, achieving coupling under the surface is critical to seismic data quality. Unfortunately, the Mars-96 mission was lost during launch and never rebuilt [36]. Concurrently, NASA Jet Propulsion Laboratory developed the Deep Space 2 (DS-2) penetrator system. DS-2 featured a small 670 g fore-body and 1740 g aft-body and was expected to impact at 140 — 210 $\mathrm{m\,s^{-1}}$. DS-2 included a heat shield which encapsulated the entire structure and was designed to crack on impact. DS-2 was instrumented with a soil sampling system connected to a microcontroller and a set of accelerometers for measuring the impact conditions in both the fore-body and aft-body. Unfortunately, both DS-2 probes were not heard from after deployment and the mode of failure is unknown [51] [6] [36]. In addition to penetrator concepts for Mars, several concepts for lunar penetrators were also proposed, such as Lunar-A. Since Earth's moon doesn't have an atmosphere, deorbiting and/or slowing the penetrator requires rockets, adding significant system complexity. Lunar-A proposed a single-rocket system for deorbiting, but didn't have a propulsion system for significantly reducing impact velocity; thus impact velocity was designed for 300 $\mathrm{m\,s^{-1}}$. Penetrator systems for icy moons would have similar de-orbit challenges. [46] [36]. Since planetary penetrator design depends highly on surface material properties which are spatially variable, launching as many low-cost penetrators is likely a critical component of a successful mission.

Additional testing on planetary penetrators has been conducted by the Europa Kinetic Penetrator team at University of Washington, which incorporates a two-stage penetrator design where the first penetrator breaks the upper surface with the goal of reducing accelerations for the secondary penetrator. Testing was conducted using a gas gun into ice at speeds up to 2000 $\mathrm{m\,s^{-1}}$ and simulations were conducted into concrete to mimic the cryogenic ice [46]. Later studies characterized the crater geometry created by the probe at Taku Glacier [19].

Air-dropped Antarctic penetrators were pioneered by Matsushima et al, with further analysis done by Poe. The Matsushima penetrator was a 14.5 kg, 0.12 m diameter, 0.945 m long unit, which was designed for a terminal velocity of up to

60 $\mathrm{m\,s^{-1}}$, as calculated by Poe [38] [43]. Results were further synthesized by Poe, showing impact accelerations of up to 1430 $\mathrm{m\,s^{-2}}$.

The Aircraft-Deployable Ice Observation System (ADIOS) described by Jones and Gudmundsson was a set of air-dropped penetrators designed to deliver GNSS payloads to Pine Island Glacier. ADIOS was 2.5 m long, including 1.5 m of antenna structure, and in the program 37 units were built, of which 26 survived impact. ADIOS was designed for simple deployment from an aircraft with a tubular design which had simple fold-out snow brakes and was slowed to a terminal velocity of 42 $\mathrm{m\,s^{-1}}$ using a disk-band parachute. In drops where only the front portion impacts the snow, Jones cites a maximum acceleration of 900 $\mathrm{m\,s^{-2}}$, and in drops where the snow brakes also impact, then Jones cites an acceleration of 9000 $\mathrm{m\,s^{-2}}$. Thus, because ADIOS lacks an aft-body section, the main payload systems must bear the full acceleration of the snow brakes during deeper impacts. Like SGIP, ADIOS transmits data via Iridium and is powered by several lithium sodium chloride batteries. Compared to SGIP, the lack of a seismometer means that ADIOS collects data at 6 samples/day rather than >30 Hz, significantly reducing the data volume and power budget for transmission [28]. The lack of a detachable fore-body/aft-body interface makes for easier deployment and lower cost compared to SGIP, but requires a higher acceleration rating on the payload; this architecture would be insufficient with a seismic payload since a detachable fore-body/aft-body interface is needed to reduce wind noise.

While penetrators are often easy to deploy and can yield excellent coupling for seismic payloads, air-dropped sensor units which are not designed to penetrate are used for other applications such landing on the surface to collect data in hard-to-reach areas of volcanos [52]. Air-dropped systems, such as dropsonds for atmospheric data collection, may also collect data during the drop phase [23].

1.3.2 Research Use Statement

Technology development for the goals of environmental and planetary science requires evaluation of related interests in other fields. While evaluating the ethics of basic research requires multidisciplinary foresight, evaluating more applications-focused

research, such as SGIP, requires understanding alternative applications to anticipate the impact on stakeholders.

The author partakes in research into penetrators with the goal of advancing climate science, space architecture for icy moon exploration, and geodesy. The technology developed in SGIP is not designed for military applications nor was it funded by military organizations. Military ballistics research and testing generally involve impact energy at least 10x that of SGIP, with more traditional impact materials such as steel, concrete and soil as discussed in Section 1.3.1. Since the design of penetrators is intrinsically linked with the material properties of the impact medium, research on SGIP is not directly applicable to ballistic weapons development. While small air-dropped payloads such as land-mines can be made similar in size and mass to SGIP but have limited application in snow and firn. Additionally, the need for concealment would negate the use of the fore-body/aft-body architecture demonstrated in SGIP, leading to numerous major architectural differences.

1.3.3 Designing a Seismo-Geodetic Ice Penetrator

To deliver a broadband seismometer and GNSS receiver to ice shelves and other hard-to-reach glaciated areas, the team at MIT and Haystack Observatory devised the seismo-geodetic ice penetrator (SGIP). SGIP is designed to take high-time-resolution (>30 Hz) in-situ data of glacial dynamics for an operating time of one year. This platform is designed to be dropped from a helicopter or other aerial vehicle, reach a terminal velocity of around 42 $\mathrm{m\,s^{-1}}$, passively aerodynamically stabilize, then hit the glacial firn.

Upon impact with the glacial firn, SGIP will split into two pieces: the fore-body section with batteries, seismometer, control electronics and crushable shock-absorbing material will penetrate several meters into the firn; an aft-body "flare" section bearing an antenna mast and snow spikes will stay at the surface to facilitate data transmission over Iridium satellite network. Since the dominant source of noise for surface seismic sensing is from wind, the splitting of SGIP upon impact isolates the seismometer from the wind forces that will be present on aft-body [7] [14]. The air-dropped

system architecture was picked for simplicity and to achieve seismic coupling between the fore-body and the glacial snow pack or firn. The concept of operations is depicted in Figure 1-2.

In other concurrent work by the SGIP team, significant modeling and testing was performed on critical SGIP components. These efforts include Brown's modeling of crushable materials to protect the seismometer during impact, modeling and testing of the shear pins that connect the fore-body to the aft-body. [12]. Additional work by Makikalli involved evaluating the thermodynamics of battery and SGIP system to minimize snow melting which could decrease coupling of the seismometer, and modeling and testing the aerodynamics during the drop from the helicopter to understand the system terminal velocity and aerodynamics stability [37]. These aforementioned aspects of design and analysis are intrinsically linked. For instance, calculations of impact mechanics inform the modeling of crushable materials for the seismometer and the required radius of the impactor. Additionally, aerodynamic constraints inform the penetration mechanics and shape of the penetrator unit. Thus, in designing SGIP, analyses were performed iteratively with involvement of the entire team.

Manufacturing of SGIP was conducted at Haystack Observatory, resulting in the as-built full-size prototype shown in Figure 1-3. Detailed views of SGIP prototype subsystems such as a battery cell, battery cell rack, top plate of fore-body, coiled umbilical and aft-body are shown in Figure 1-4. To facilitate year-long operations, SGIP is sized to hold 260 Lithium Thionyl Chloride (Li/SOCl2) primary batteries, consisting of a 17.7 kW h capacity. The first prototype of SGIP has a total system mass of 132 kg, consisting of a 64 kg, 0.11 m radius fore-body and a 68 kg, 0.75 m radius aft-body.

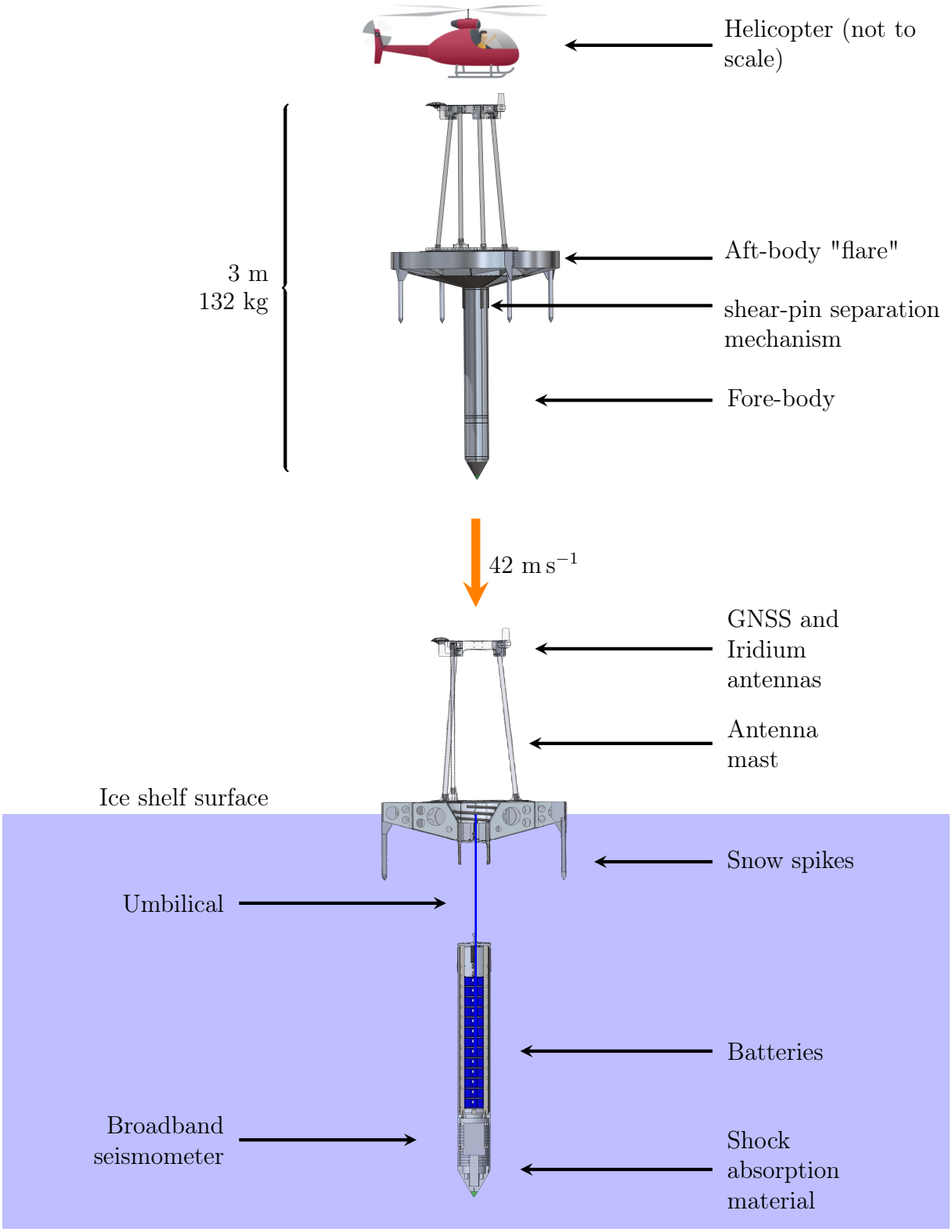
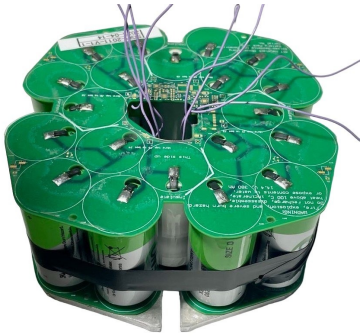


Figure 1-2: Concept of operations of air-dropped ice penetrator. SGIP is dropped out of a helicopter, reaches a terminal velocity of 42 m s^{-1} and hits an ice shelf, causing the fore-body and aft-body to separate.



Figure 1-3: As-built full-size prototype of the Seismo-Geodetic Ice Penetrator (SGIP).



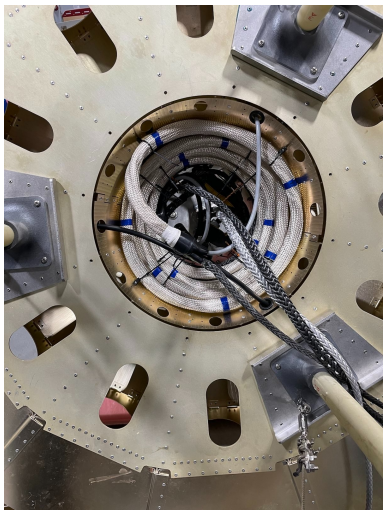
(a)



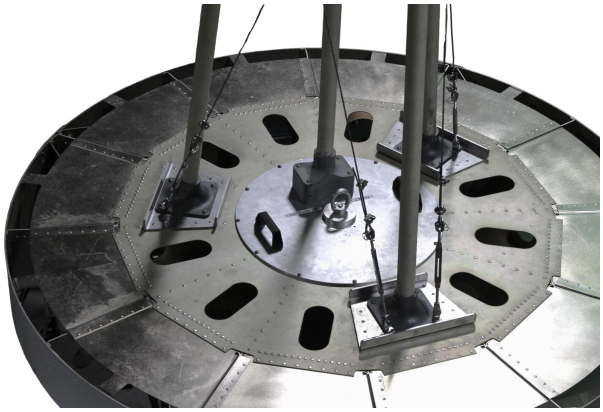
(b)



(c)



(d)



(e)

Figure 1-4: Pictures of prototyped SGIP subassemblies including (a) battery pack unit. (b) battery cell rack with battery-weight-equivalent steel plates installed for initial structural testing. (c) top plate of sealed fore-body section. (d) top-view of aft-body with top plate removed, showing coiled umbilical cable. (e) angled view of aft-body, showing adaptable aerodynamic plate which can be size-selected for surface firn conditions.

Chapter 2

Impact Mechanics and Testing

2.1 Motivation and Background

Understanding the impact interaction is critical for any penetrator system design, including SGIP. During the impact phase of SGIP operations, the fore-body must enter the firn without tipping, then the aft-body must hit the firn, causing the fore-body and aft-body to separate. This separation is critical for collecting data from the SGIP seismometer with minimal wind noise. If SGIP doesn't penetrate enough, then the system may tip over, and will be not achieve seismic coupling. Even a total penetration may allow the seismometer to be affected by wind noise if the penetration is not sufficiently deep. If SGIP penetrates too far, then recovery of the fore-body will be more challenging during field testing. Thus, for an SGIP body length of 1.3 m, ideal penetration distance would be between 1.8 m and 4 m.

Understanding shock loads from impact is critical for component design and sizing. For instance, the payload seismometer and other sensitive payloads have acceleration limits which require inelastic crushable structures sized with respect to the impact. Additionally, shear pins for fore-body and aft-body separation are also sized using acceleration values from impact calculations. The SGIP system frontal area is roughly proportional to acceleration; impact calculations and drop testing may inform the frontal area of future interactions of SGIP. To attain the desired penetration distance with an acceptable acceleration on the fore-body and aft-body structures, a desired

terminal velocity is determined, thus driving the size requirement of the flare.

Despite the importance of impact modeling for penetrator design, modeling impacts into soft materials like snow and firn presents numerous unsolved challenges that have plagued past penetrator systems. Indeed, as detailed in Section 1.3.1, the Matsushima penetrators all had significant payload failures during impact, the "Igloo White" ADSID penetrators had a significant failure of around 20 % and in the ADIOS deployment, only the 26 out of 37 deployed units survived impact [36] [38] [28]. While some of the high failure rates can be attributed to surface features such as trees, for ADSID and crevasses for ADIOS, many of the sensor failures likely occurred during the impact phase. Given the high failure rates of other penetrator architectures, in order for an array of penetrators to effectively deploy a distributed sensor network it must be composed of a significant number of units. That is, due to uncertain impact criteria it is much more favorable to build a large array of low-cost penetrators than a small array of high-cost penetrators. By further understanding this impact phase, higher penetrator yield rates may be obtained, by better selection of impact sites and by facilitating adjustments to design and operations to meet local impact material properties.

Modeling and testing impact mechanics into snow and firn presents unique challenges compared to more traditional ballistics materials such as ballistic gel, sand, cement and metals. Since water is liquid at room temperature, conducting impact mechanics on snow and firn requires cold temperatures and a known history of the target material temperature. The mechanisms of impact energy absorption in snow and firn are complex; energy may be absorbed through compaction, fracture, and friction between grains. While some materials, like sand, may be modeled well as a granular material and other materials like metal or foam may be modeled well as a bulk solid, snow and firn can behave either as a granular material or a bulk solid depending on the snow grain structure. While impact mechanics of metals, soil and cement have been relevant topics for military study, impact into snow has not received nearly as much research, likely because it is not used as a primary construction material for military assets.

Prior modeling efforts of impact into snow have fallen into one of three approaches, listed in increasing fidelity, capability and respective runtimes. The first approaches to modeling impact into firn and snow consisted of curve fitting to field test data with relatively little physical insight. The standard of empirical fitting to testing data is work by Young [58], which outlines a set of penetration equations which predict a final penetration depth based on impactor mass, area, nose length, impact velocity and a fudge-factor for the rate of energy absorption of the material. The Young equation for "ice and frozen soil" and at velocities $<$61 $\mathrm{m\,s^{-1}}$ is reprinted in Equation (2.1). These equations are fit based on a dataset for S values < 60, where the penetrator travels $>$3 diameters into the target material, following a simple ballistic trajectory [58].

$$z = 0.00024\ SN \left(\frac{m}{A}\right)^{0.6} \ln\left(1 + 2.15 * 10^{-4} v^2\right) \ln\left(50 + 0.29 m^2\right) \quad [\mathrm{m}] \tag{2.1}$$

where

S is a dimensionless factor to denote the penetrability of the target material.

N is a dimensionless nose performance coefficient. For conic nose shapes, this is given as $N = \frac{L_n}{4d_n} + 0.56$, where L_n is the length of the nose, and d_n is the diameter of the nose.

m [kg] is the mass of the penetrator.

A [$\mathrm{m^2}$] is the frontal area of the penetrator.

v [$\mathrm{m\,s^{-1}}$] is the impact velocity of the penetrator.

The next level up in fidelity and complexity from empirical model fits are simple physical models of penetration which posit a modality of energy absorption. For penetration into ice, the "plug model" is common example, which calculates an area which shears in the impact material per length that the impactor travels through the medium. For impacts into snow, models typically use compaction in the vertical

direction, compaction in the horizontal direction, granular interactions, friction, or bulk shear effects in models.

More complex physical models use finite element analysis (FEA) simulations. Since impact mechanics is a transient event with large material deformations, finite element techniques must use explicit solvers, leading to long runtimes. Generic finite element packages like Ansys Explicit Dymamics can model behaviors like bulk compression and fracture, but struggle to model particle-like behaviors like cratering and spalling. For these phenomena, particle-like models can be a better fit, such as those using smooth particle hydrodynamics (SPH); however, SPH models are much more difficult to ground in measured material properties of snow. The most sophisticated and realistic models of snow and firn have been developed for computer graphics applications, such as the movie Frozen, and use the material point method (MPM), which has several updates which blend the advantages of traditional bulk finite element methods with particle models [54]. MPM models can realistically model almost all methods of snow energy absorption and dissipation, but are difficult to ground in tested snow material properties and have runtimes orders of magnitude higher than other methods. These most sophisticated methods are best for modeling one-off events where there are large deformations and several modes of energy absorption, such as avalanches [22]. For SGIP work, the main focus of simulation and impact modeling studies is to make rapid systems design and operations decisions; thus, an emphasis is given to less computationally-expensive methods.

2.2 Modeling Inputs

2.2.1 Penetrator Sizing

In this chapter, several different penetrator models relevant to SGIP are considered, each with different dimensions and mass measurements. In modeling impacts, penetrator geometry was simplified to a set of six measurements depicted in

Figure 2-1. The full-size models include the as-built prototype SGIP model, tested in Alaska in May 2023 and a model described by Poe in past SGIP work, featuring a significantly lower mass flare and longer fore-body. The dimensions for the full-size models as well as a scale model are listed in Table 2.1.

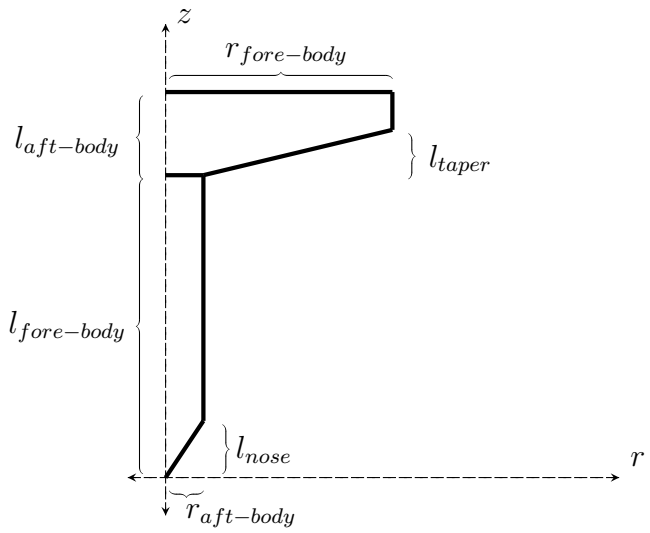


Figure 2-1: Key measurements of simplified penetrator geometry.

Table 2.1: Dimensions of penetrator models considered in impact simulation. The symbol ** denotes that measurements were taken at the top of the conical flare section, not including the full aerodynamic structure.

	$r_{fore-body}$ (m)	$r_{aft-body}$ (m)	$l_{fore-body}$ (m)	$l_{aft-body}$ (m)	l_{nose} (m)	l_{taper} (m)	$m_{fore-body}$ (kg)	$m_{aft-body}$ (kg)
As-built prototype, Alaska 2023	0.11	0.6 **	1.30	0.30	0.15	0.16	64	68
Poe model	0.1	0.55	2.28	0.29	0.21	0.12	66	26
Small-scale model	0.025	NA	0.25	NA	0.045	NA	2.1	NA

2.2.2 Density Profiles

In modeling impact mechanics in snow and firn, density is a key driving parameter; in most models, including simple models such as those described in Section 2.5, essential material properties such as speed of sound, elastic modulus, and Poisson ratio have a strong dependence on density. This link is also a key weakness in the snow modeling

field. Most models, including those in this thesis, assume that material properties between snow density of multiple samples are the same, whereas there are many crucial confounding variables such as grain size, grain structure, and the temperature history of the sample. This degeneracy makes it difficult to compare models across different types of snow and to compare modeling and calibration efforts from different research teams. Nevertheless, density data is much more widely available than more detailed particle data because it is taken in standard snow pit measurements, so this degeneracy is acknowledged and noted in interpretation by denoting the type of snow in datasets. In the SGIP impact cases, the materials of interest are surface snow and low density firn which have experienced minimal surface melt and refreeze cycling. For full-scale modeling, data are taken from measurements on the Taku Glacier in April by McGrath [39] as $410 \pm 45\ \mathrm{kg\,m^{-3}}$, with a generally increasing trend contextualized by Pelto [42]; models were run on a corresponding linear fit shown in Figure 2-2. For the Ross Ice Shelf, a density profile was taken from Lightenberg, [34], which was chosen for comparison to past models by Poe [43]. This interpolated model is also pictured in Figure 2-2.

2.3 Modeling Workflow

In modeling the impact of SGIP into snow, a variety of approaches are taken which are compared and inform the design and operations decisions of the test articles. Since opportunities to test-drop full-scale SGIP prototypes into snow are infrequent and expensive, most testing opportunities would be using a smaller model penetrator. Using drop data from the small-scale penetrator, both FEA and other physical models may be calibrated and validated, then the parameters in the models can be used in a corresponding full-scale model. To inform design and concept of operations (CONOPS) changes, emphasis on developing both FEA models and other physical estimates is important since most physical estimation methods have runtimes of <1 s, whereas explicit FEA models have runtimes of 30 min — 24 h. The set of different steps in modeling the SGIP impact is depicted in Figure 2-3.

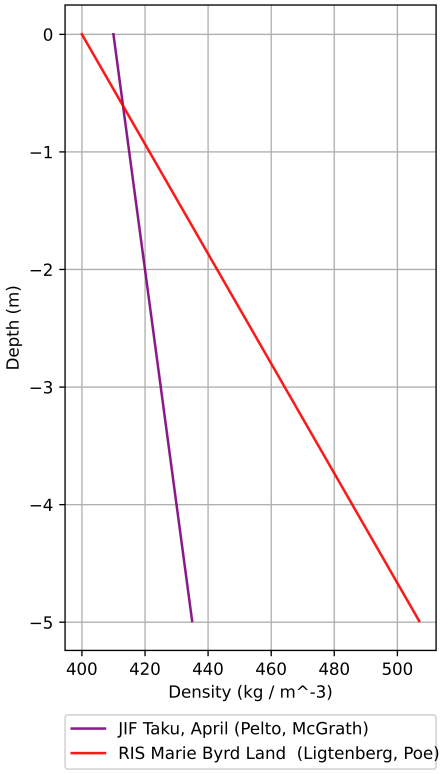


Figure 2-2: Snow and firn density profiles used for modeling SGIP impact.

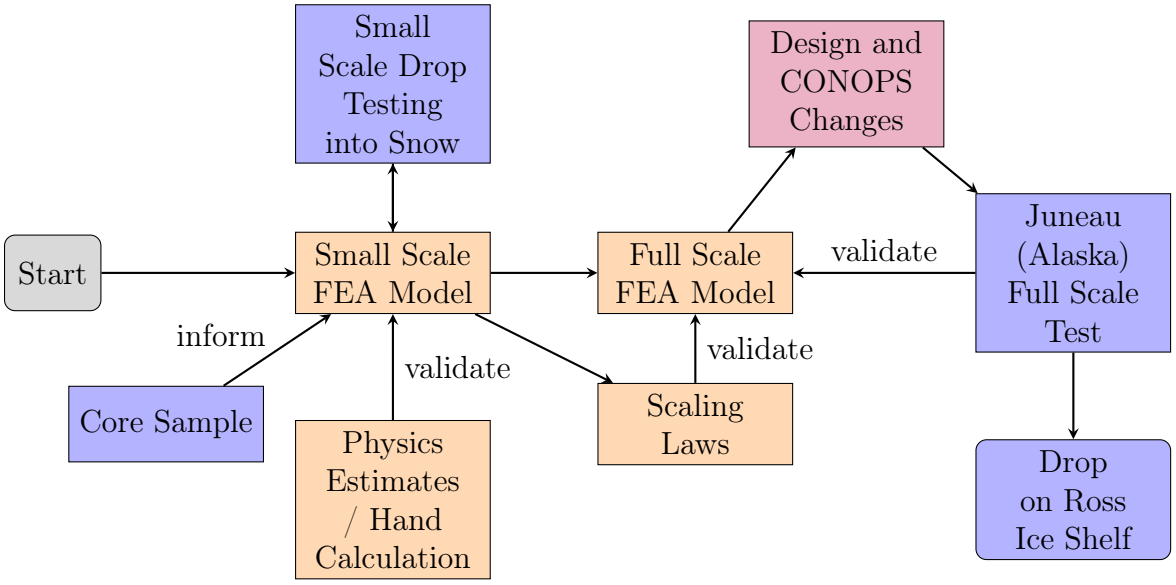


Figure 2-3: Model workflow for SGIP impact studies.

2.4 Drop Testing

While impact analysis and simulation are invaluable for rapid design exploration and study, there is no substitute for testing. Due to the many modalities of snow energy absorption and the degeneracy of the material descriptors used in modeling, drop testing provides the best validation for modeling efforts and the best indicator of penetrator performance in representative media. In this work, the concept of degeneracy is used to refer to a mapping where there is more than one possible distinct output for a given input.

2.4.1 Small Scale Drop Testing

Due to the prohibitive expense of frequent full-scale testing, most SGIP design testing was conducted on a small-scale model with dimensions listed in Table 2.1. The SGIP team constructed this model out of steel an a removable interior 2000 $\mathrm{m\,s^{-2}}$ rated Gulf Coast Data Concepts X200-4, 3-axis accelerometer which is based on the Analog Devices ADXL375. This accelerometer is accessible using two thumb screws for easy field operations. An eyebolt is placed at the top of the penetrator to tie off paracord, allowing for easy release and recovery of the penetrator in deep snow.



Figure 2-4: Small-scale model, 0.025 m radius, 2.1 kg mass, penetrator used for drop testing. An interior 3-axis accelerometer measures impacts and is easily removable in the field with thumbscrews on the top.

A set of 32 drop tests was conducted on 2/4/2022, 2/7/2022 and 3/9/2023 by the SGIP team in a variety of snow density profiles with results detailed in Table 2.2. The 2/4/2022 and 2/7/2022 tests were done indoors at MIT using snow collected from a recent snowfall. Releases were made consistently through a PVC drop tube into a 5 gallon bucket. The high >600 $\mathrm{kg\,m^{-3}}$ snow density can attributed to slushy-consistency snow that had experienced melting in the indoor environment; because of the melting, the density increased in subsequent trials in this test. The 3/9/2023 tests were conducted in Big Sky, Montana into two snowpacks; procedures for measurement and characterization of these are described in Section 4.3.1. The snow density profiles used for small drop testing are shown in Figure 2-6. To attain a 3 m maximum drop height in these field tests, the small model was released, in some cases from a ski pole with a pulley attached to the end, and in other cases from a tree branch with a pulley attached. Due to this less-constrained drop system, these test series have more angular variability from vertical compared to the 2022 tests. In the lowest density snow at higher drop heights, the model was observed impacting the frozen soil layer beneath the snow. During the 3/9/2023 Big Sky drops 11-32, the compaction around the small penetrator impact sites was measured in comparison to the surrounding density profiles to calibrate impact models; these measurements were within the error margin of the measuring techniques used. Examples of acceleration profiles from this series of small test drops are shown in Figure 2-5 with the complete set of plots in Appendix A.

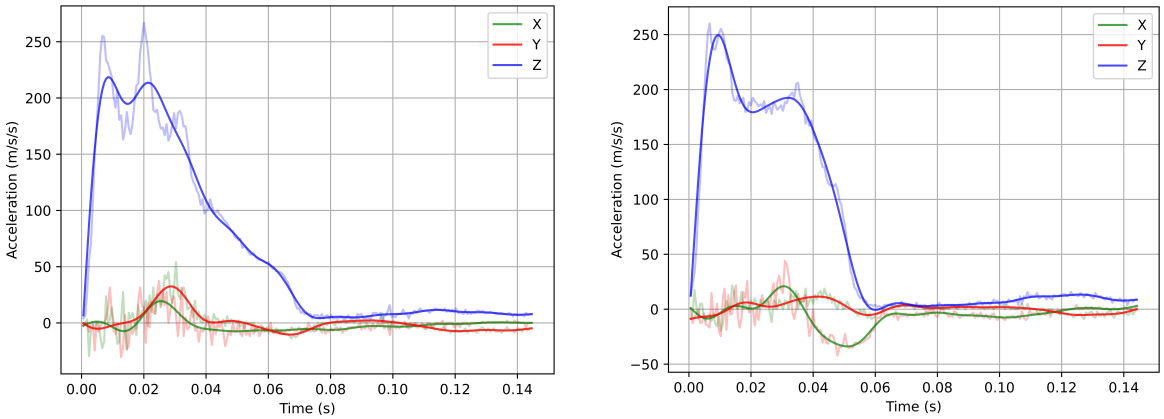
2.5 Simple Numerical Models

2.5.1 Simple Young Model

The simplest model of penetration is the Young model shown in Equation (2.1); this is a 1D model with no direct material property inputs. The Young model was elaborated upon by adding a variable penetrator area which models the shape of SGIP. The original Equation (2.1) only gives a final depth of penetration, so the

Test Date (d/m/y)	Test Number	Drop material density ($kg\,m^{-3}$)	Body Mass (kg)	Body Radius (m)	Body Length (m)	Peak Axial Acceleration ($m\,s^{-2}$)	Peak Lateral Acceleration ($m\,s^{-2}$)	Average Axial Acceleration ($m\,s^{-2}$)	Observed penetration distance (m)	Drop Height (m)	Drop Velocity ($m\,s^{-1}$)
2/4/2022	1	559	2.9	0.05	0.195	78	100	40	0.30	1.1	4.7
	2	559-606	2			250	244	68	Not measured	1.3	5.0
	3					193	172	86		3.3	8.1
2/7/2022	4	606				157	62	109	0.30	2.9	7.6
	5	624				262	54	116	0.20	3.1	7.7
	6	645				255	46	146	0.19	2.8	7.5
	7	645				281	90	133	0.17	3.0	7.7
	8	663				287	112	108	0.18	3.0	7.7
	9	663				267	114	112	0.18	2.8	7.5
	10	676				246	86	124	0.17	2.2	6.6
3/9/2023	11	Big Sky Profile 1: 0 - 0.15 m: $170 \pm 21\,kg\,m^{-3}$ (N=4) 0.15 - 1.0 m: $283 \pm 9\,kg\,m^{-3}$ (N=4)				1464 **	2173 **	20	Not measured	3.0	7.6
	12					65	150	31		1.8	5.9
	13					1905 **	2040 **	15		0.4	2.7
	14					60	304	17		0.6	3.4
	15					634 **	638 **	16		0.5	3.1
	16					25	142	13		0.3	2.4
	17					63	119	21		0.2	2.2
	18					40	100	17		0.4	2.8
	19					66	128	16		0.3	2.5
	20					73	48	32		0.1	1.4
	21					127	86	59		0.4	2.7
	22					81	39	37		0.6	3.4
	23	Big Sky Profile 2: 0 - 0.15 m: $335 \pm 40\,kg\,m^{-3}$ (N=6) 0.15 - 1.0 m: $413 \pm 26\,kg\,m^{-3}$ (N=4)				135	86	67		0.7	3.8
	24					167	87	68		1.4	5.3
	25					188	235	98		1.9	6.2
	26					259	249	41		2.7	7.3
	27					235	403	96		2.6	7.2
	28					91	247	39		2.5	7.0
	29					181	271	39		2.5	7.0
	30					230	138	118		2.7	7.3
	31					217	124	89		3.0	7.7
	32					301	846	79		3.1	7.9

Table 2.2: Test drops of small model penetrator into snow. Rows with ** denote tests that punched through the snowpack and hit frozen soil.



(a) Drop 5

(b) Drop 6

Figure 2-5: Example drop test data referencing to Table 2.2. Complete data are in Appendix A. Acceleration profiles are filtered with a 20 Hz low-pass filter in solid colors for clarity, with the original in the background.

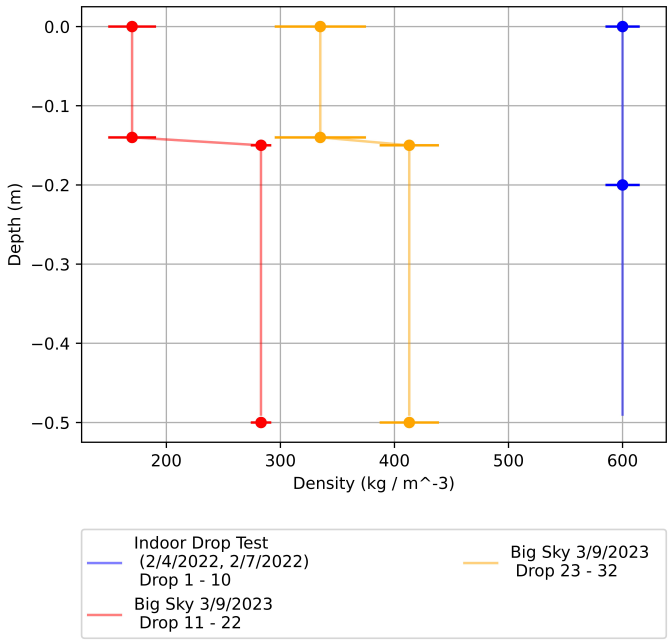
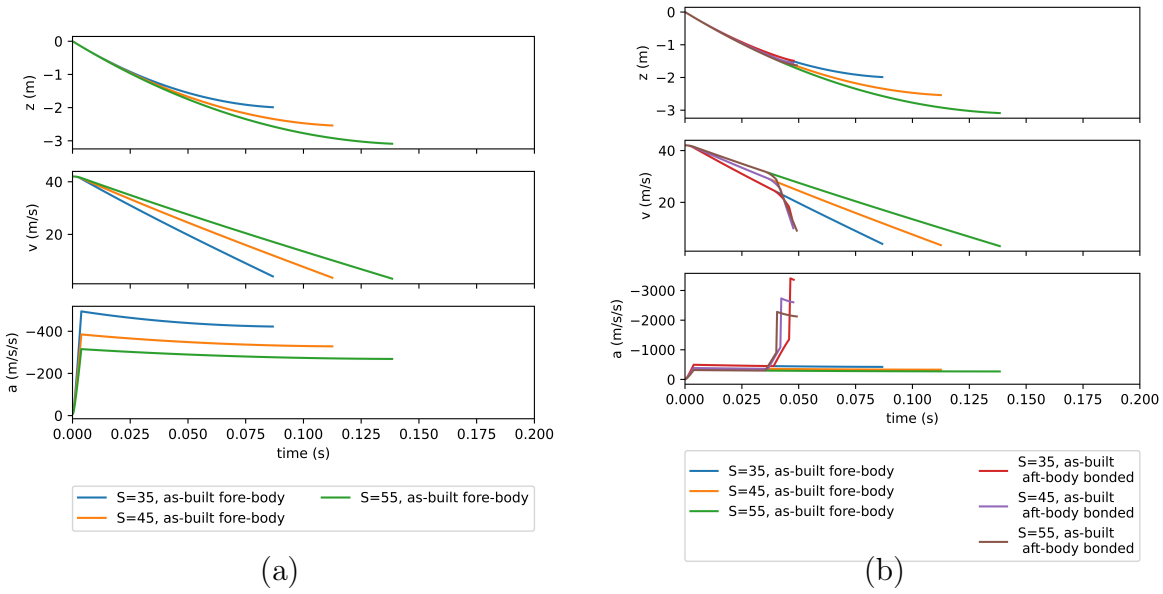


Figure 2-6: Density profiles measured in small drop tests detailed in Table 2.2, calculated by measuring the mass of a known volume. For the indoor drop tests 1—10, this plot shows an example profile for drop 3 to compare with the other snow packs; each drop had its own measurement reading as noted in Table 2.2.

equation was evaluated for discrete increments of penetration to yield a full position, velocity and acceleration time-series. For impact into firn, prior results indicate that S values of 36 — 40 are appropriate, with the range likely higher in softer surface snow. A result of this discretized model is shown in Figure 2-7 for the full-size as-built prototype for S values 35 — 55, and an example impact velocity of 42 $\mathrm{m\,s^{-1}}$ with and without the flare.

2.5.2 Compaction Model

While the Young model presents a simple 1D phenomenology of impact mechanics, useful design decision making requires a more full-featured model which can directly correlate to measurable snow material properties. Thus, a nonlinear compaction model is presented which predicts a full impact trajectory based on the impact material elastic modulus, speed of sound and impactor initial velocity and dimensions.



(a) (b)

Figure 2-7: Example of Young Equation (2.1) applied to as-built SGIP model tested in Juneau with drop velocity of 42 $\mathrm{m\,s^{-1}}$ over a range of S values (a) with only the fore-body section. (b) with both the fore-body and the fore-body bonded to the aft-body "flare". Note the significant increase in acceleration which occurs upon the flare impact, after which the fore-body-only models continue into the snow.

The nonlinear elastic compaction model uses a set of elastic "spring" elements which are arranged radially around the site of impact, such as shown in Figure 2-8. During impact, these elements deform radially, with the nose cone forcing these elements outwards; it is assumed in this model that there is no vertical transport of material. The model splits the impact material into discrete and non-interacting radial slices; in each slice there there is a known volumetric change from the penetrator going through the target material. Although the slices are shaped like an annulus, the compaction is solved as a set of 1D problems arranged radially. Since the elastic modulus is highly nonlinear with strain, the energy absorption in a volumetric element is calculated by a series of infinitesimal elastic deformations, each at a different strain and corresponding elastic modulus. By adding up all of the compacting elements, the amount of energy absorbed in each vertical layer slice may be calculated and used to form a complete impact trajectory. This iterative process is depicted in Figure 2-9.

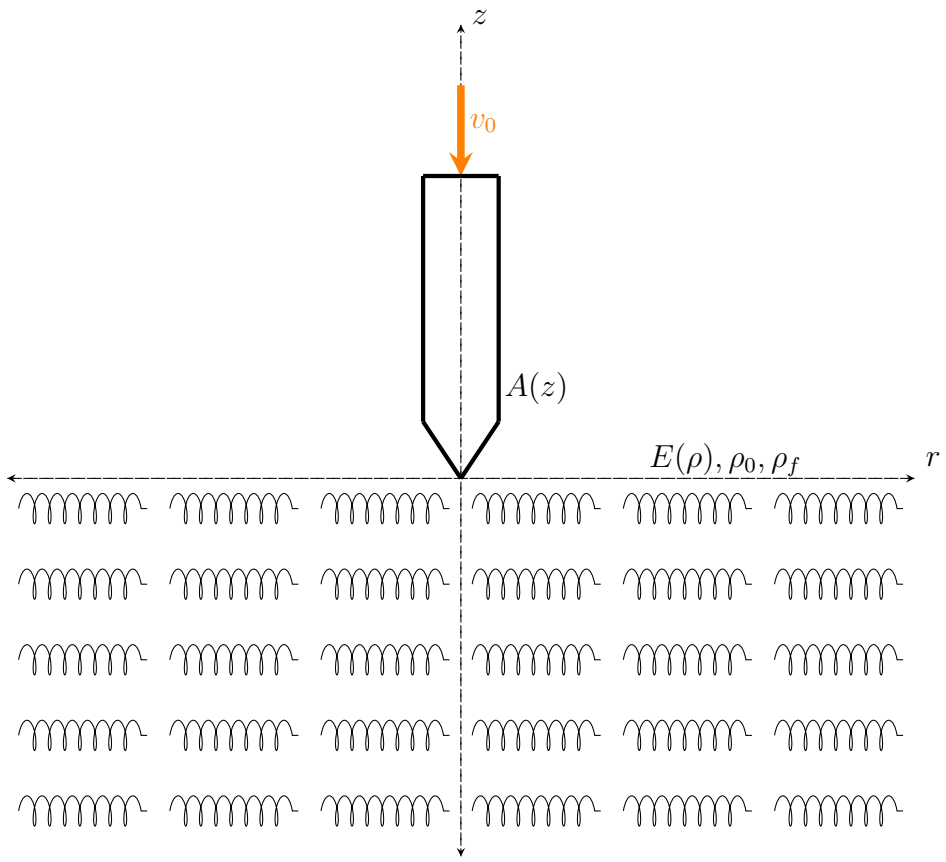


Figure 2-8: Compaction model features an infinite grid of 1D elastic elements with modulus E that depends nonlinearly on the material density.

Assumptions and Justification

This nonlinear compaction model makes the following assumptions, each of which has the following implications on model applicability.

1. All energy absorbed during impact is absorbed through compaction. This model neglects other energy absoption modalities in snow and firn such as frictional interaction during particle transport and fracture. Thus, this model is most applicable to surface snow and firn with densities below 600 $\mathrm{kg\,m^{-3}}$ and no significant crust or ice lens features. For impact materials with fracturing features at the surface, this model may be superimposed with another model on a layer-by-layer basis.

2. All is absorbed in the radial direction. Since this system is modeled as an infinite

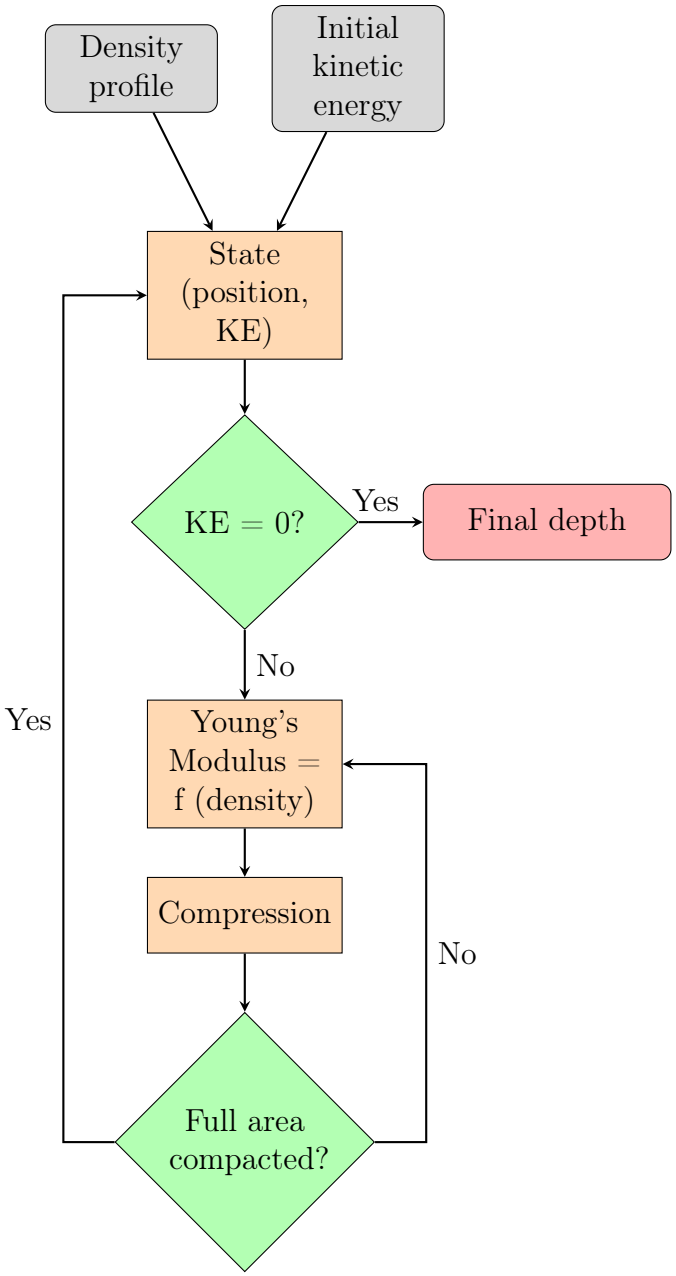


Figure 2-9: Flowchart describing a nonlinear compaction model.

network of compressive elements that only compress in the radial direction, it is implied that there is no vertical transport of snow or firn during impact. This assumption is close to valid for nose-cone shapes with $\frac{l_{nose}}{r_{fore-body}} > 1$ with an ideal ratio being significantly higher; that is, pointier nose geometries are better transporting material radially rather than vertically. In most impacts, there is an area of newly-compressed material directly in front of and to the side

of the penetrator; the ratio of these depends on the total depth of penetration. Thus, this elastic compaction model is most valid for impacts that reach a depth of $|z| > 6r_{fore-body}$.

3. Impact is nonlinear and elastic. This model models inelastic energy by iteratively evaluating small elastic deformations individual material elements with an elastic modulus which is nonlinear with respect to the strain without consideration of strain rate. In reality, the deformations are inelastic and strain rate dependant.

Mathematical Overview and Model Inputs

In an elastic deformation of snow, the elastic modulus is given by a power law shown in Equation (2.2); this forms a nonlinearity where the material becomes stiffer the more it has been compacted [24]. In this model the elastic modulus is used rather than the bulk modulus because the compression is uniaxial and shear is neglected.

$$E = c\rho^k \quad [\text{Pa}] \tag{2.2}$$

where

ρ [kg m^{-3}] is the density of snow or firn.

c is a non-dimensional fitting constant, derived through material testing [24].

k is a non-dimensional fitting constant, derived through material testing [24].

The nonlinear elastic model considers deformations in uniaxial strain, depicted in Equation (2.3).

$$\varepsilon = \frac{l}{l_{cell}} \tag{2.3}$$

where

l [m] is the deformed length of a cube of material along the radial axis of the penetrator.

l_{cell} [m] is the original undeformed length of a cube of material.

In a generalized cube of impact media, a strain is applied which changes the density of the impact media. The relation between strain and density is expressed in Equation (2.4).

$$\rho = \frac{m_{cell}}{l_{cell}^2(l_{cell} + \varepsilon l_{cell})} \quad [\mathrm{kg\,m^{-3}}] \tag{2.4}$$

where

m_{cell} [kg] is the mass of the cube under consideration, which is invariant through deformation, and is calculated using the starting density and volume.

During a generalized uniaxial compaction of a cube of material from an initial density to a final density, the final strain is calculated in Equation (2.5).

$$\varepsilon_f = \frac{\rho_0}{\rho_f} - 1 \quad [\ ] \tag{2.5}$$

where

ρ_0 [$\mathrm{kg\,m^{-3}}$] is the density of the cube of snow before compaction.

ρ_f [$\mathrm{kg\,m^{-3}}$] is the density of the cube of snow after compaction.

From Equation (2.3), the initial strain before any compaction occurs in each cube of impact material is given in Equation (2.6).

$$\varepsilon_0 = 0 \quad [\ ] \tag{2.6}$$

In a compaction event with a defined starting and ending strain, the change in volume in a cube is shown in Equation (2.7).

$$dV_{cell} = l_{cell}^3 \varepsilon_f = l_{cell}^3 \left(\frac{\rho_0}{\rho_f} - 1 \right) \quad [\mathrm{m^3}] \tag{2.7}$$

In a simple 1D compaction of a cube, the energy stored in that cube is given in Equation (2.8). Note that the elastic modulus is depicted as a function of density which is a function of strain, the variable of integration.

$$u_{cell} = \int_{\varepsilon_0}^{\varepsilon_f} E(\rho(\varepsilon))\varepsilon d\varepsilon \quad [\text{J}] \tag{2.8}$$

By plugging in Equation (2.2), this expression yields Equation (2.9).

$$u_{cell} = \int_{\varepsilon_0}^{\varepsilon_f} c\left(\frac{m_{cell}}{l_{cell}^2(l_{cell}+\varepsilon l_{cell})}\right)^k \varepsilon d\varepsilon \quad [\text{J}] \tag{2.9}$$

An advantage of using a power law fit for the elastic modulus nonlinearity is that this expression may be solved analytically, enormously speeding up computation times compared to a numerical integration procedure. This new expression is shown in Equation (2.10).

$$u_{cell} = -c\frac{m_{cell}^k}{l_{cell}^{2k}}\left[\frac{(\varepsilon+1)(\varepsilon(l_{cell}-1)+1)\left(\frac{1}{l_{cell}\varepsilon+l_{cell}}\right)^k}{(k-2)(k-1)}\right]\Bigg|_{\varepsilon_0}^{\varepsilon_f} \quad [\text{J}] \tag{2.10}$$

In the oversimplified case where all cubic cells within the same layer z are compacted to the same final strain, the total energy per layer may be written simply in Equation (2.11). This is an oversimplification which will be explored and amended later, but is useful conceptually and for making faster runtime solvers. By totalling up the energy absorbed in all layers through this procedure, the complete impact mechanical trajectory may be simulated.

$$u_{layer} = u_{cell}\frac{A_{penetrator}|_z}{l_{cell}^2} \quad [\text{J}] \tag{2.11}$$

Final Compacted Condition

In the simplest formulation of the nonlinear compaction model, a simplification is made which implies that all cells in each vertical layer are compacted to the same final strain, and corresponding final density. This is clearly an oversimplification because material further away from the penetrator should be compacted less than material directly next to the penetrator. In many cases such as quick design studies, this may be an appropriate simplification because it leads to much faster runtimes. However, a significant issue is that it leaves a free parameter for ρ_f or ε_f, the final compacted

condition. Fortunately, this parameter may be evaluated experimentally if needed to validate models, unlike the free S parameter in the Young model. Nevertheless, it is a valuable to exercise see what bounds there are on this final compacted condition and to find a value of $\varepsilon_f(r)$ which depends on r.

Due to the nature of uniaxial compression occurring in the nose-cone region of the impactor, an upper bound of the furthest away compacted element on each z may be found using the speed of sound in the impact medium. This is calculated in Equation (2.12).

$$r_{sound} = \frac{v_{sound}}{v_{penetrator}} l_{cone} \quad [\mathrm{m}] \tag{2.12}$$

where

l_{cone} [m] is the length of the nose cone of the penetrator, depicted in Figure 2-1 with numbers in Table 2.1.

v_{sound} [$\mathrm{m\,s^{-1}}$] is the speed of sound in snow.

$v_{penetrator}$ [$\mathrm{m\,s^{-1}}$] velocity of the penetrator evaluated at the height z of the layer of interest.

If it is assumed that the number of elements compacted is dictated by the speed of sound, across the elements in a layer affected during the compaction event, the average final strain between all of the elements is expressed in Equation (2.13). However, since the elastic modulus is nonlinear in strain, it is valuable to solve for the specific strain at each radius value. In reality, $\overline{\varepsilon_f}$ is a lower bound, since there might be factors in compression that prevent compaction all the way to r_{sound}, such as granular interactions between snow grains.

$$\overline{\varepsilon_f} = \frac{1}{\left(\frac{r_{sound}}{r_{penetrator}}\right)^2 - 1} \tag{2.13}$$

The corresponding lower bound average density across all compacted elements in a layer is given in Equation (2.14).

$$\overline{\rho_f} = \rho_0 + \frac{\rho_0}{\left(\frac{r_{sound}}{r_{penetrator}}\right)^2 - 1} \quad [\mathrm{kg\,m^{-3}}] \tag{2.14}$$

Since the nonlinear elastic model detailed here is in spherical coordinates, decay of strain is expected to roughly follow a rate of $\frac{1}{r}$, adjusted with some constants. Thus the form of $\varepsilon_f(r)$ is expected to follow that of Section 2.5.2.

$$\varepsilon_f(r) = \frac{a}{r+b} \tag{2.15}$$

where

a is a non-dimensional fitting constant.

$b << 1$ is a non-dimensional fitting constant to prevent divide-by-zero issues.

Using the general expression for the average value of a function, the average value of $\varepsilon_f(r)$ can be used to solve for a. This is shown in Equation (2.16) and Equation (2.17).

$$\overline{\varepsilon_f} = \frac{1}{r_{sound} - 0} \int_0^{r_{sound}} \frac{a}{r+b} dr = a \frac{\ln(r_{sound} + b) - \ln(b)}{r_{sound} - 0} \tag{2.16}$$

$$a = \overline{\varepsilon_f} \frac{r_{sound}}{\ln(r_{sound} + b) - \ln(b)} \tag{2.17}$$

Plugging the value of a from Equation (2.17) and the value of $\overline{\varepsilon_f}$ from Equation (2.14) into , an expression for the final strain in each element as a function of r is described in Equation (2.18).

$$\varepsilon_f(r) = \overline{\varepsilon_f} \frac{r_{sound}}{\ln(r_{sound} + b) - \ln(b)} \left(\frac{1}{r+b}\right) \tag{2.18}$$

Incorporating this final compaction condition, the energy absorbed in a cubic cell under nonlinear elastic compaction is given in Equation (2.19). This modified expression can replace Equation (2.10) in the same procedure where the compacted cells in each layer are added up, and then using all the layers the system is integrated

to yield an impactor trajectory.

$$u_{cell}|_r = c \int_{\varepsilon_0}^{\varepsilon_f(r)|_r} \left(\frac{m_{cell}}{l_{cell}^2 (l_{cell} + \varepsilon(r)|_r \, l_{cell})} \right)^k \varepsilon(r)|_r \, d\varepsilon \quad \text{[J]} \tag{2.19}$$

Results and Example Trajectories

The results of the nonlinear compaction may be evaluated for a variety of impact material density profiles, penetrator shapes, and impact conditions. When implemented in Python, this model has runtimes of < 1 s for models where the final compaction condition is averaged per layer, and < 10 s when the final condition depends on r.

In most cases, in comparison to experimental data, the compacted area of snow and firn is significantly smaller than that given by the calculated r_{sound}; this is likely due to granular interactions near the impact site. It is likely that the compaction strains around the impact site decay like $\frac{1}{n}$ where $1 < n < 2$; with longer l_{nose}, and the higher the penetration distance, n decreases. In the model implemented, the elastic modulus fitting parameters in the Equation (2.2) relation are set to $c = 0.93$ and $k = 2.3$ from Gerling [24]. As Gerling shows, these values are at the low end of the likely range for higher firn densities, and elastic modulus values could be as much as an order of magnitude more. These possible variations can be accounted for by calibrating the model to field conditions, and by measuring the final density at the impact site. For models that best fit experimental data, the averaged final strain is used for each cell in the layer. Example results are shown for a design comparison on impact between the SGIP design analyzed by Poe with the as-built prototype in Figure 2-11. Further comparisons between full-size SGIP model performance in different snow density profiles are shown in Figure 2-12. With this model, field density data can be collected and a predicted trajectory can be computed with minimal turnaround time; this capability can be used to guide future SGIP drop operations and rapid design studies. Like the Young model, the acceleration plots resemble the side-view cross-section of the penetrator, due to approximately linear dependence of acceleration on frontal area. In the small model cases, $\overline{\rho_f}$ was calibrated to be around

5 $\mathrm{kg\,m^{-2}}$, and in large model cases around 50 $\mathrm{kg\,m^{-2}}$. This calibration fits with a scaling of the final average strain ratio between the large model and the small model scales. Additionally, during field testing in Section 2.4.1, the compaction around the small penetrator impact sites for 11-32 was within the measurement error of the density measurement technique described in section 4.3.1, whereas in the large-scale Alaska drop tests in section 2.7, there was a very noticeable increase in density around the penetrator, including a thick layer caked to parts of the fore-body. The nonlinear compaction model was validated using data points 4, 17 and 26 from the small drop test sequence, as shown in Figure 2-10.

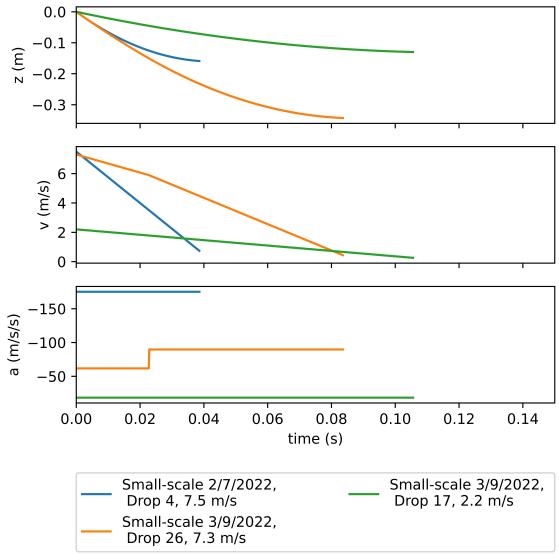
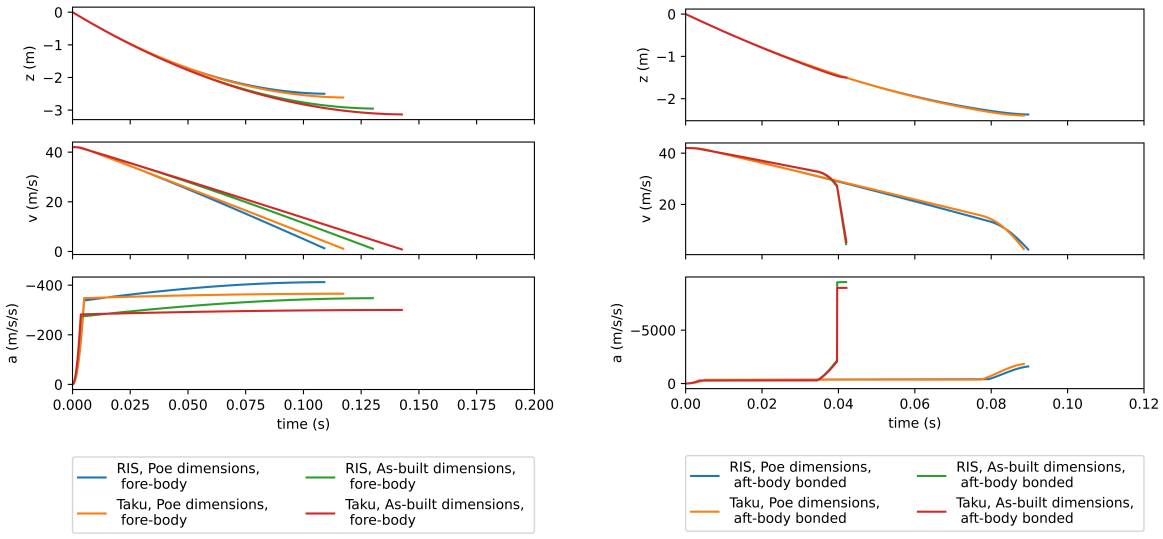


Figure 2-10: Comparison of small drop test parameters which are listed in Table 2.2 between drops 4, 17 and 26, each in a different snow pack. Note that dense slush in drop 4 has a significant underestimate in penetration distance, likely due to the different mode of energy absorption involved.

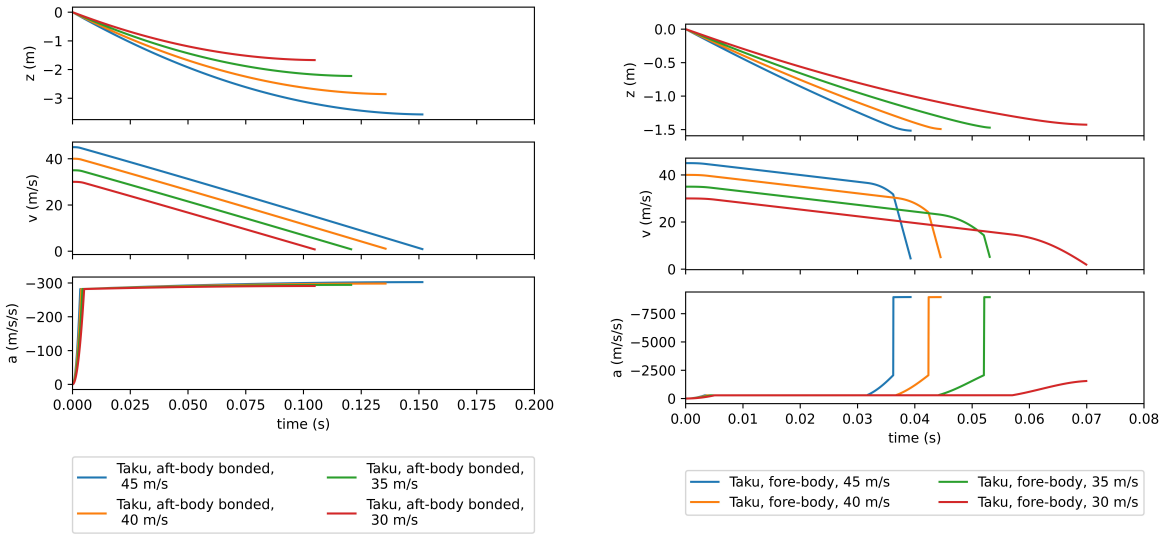
Limitations and Future Work

A critical limitation of this nonlinear compaction model is non-interaction between layers; this set of 1D models does not take into account shear interactions. This model is also only able to model simple straight impacts; in reality many impacts are angled, which has a significant effect on which areas are compressed. Additionally,



(a) (b)

Figure 2-11: Impact performance comparison of the SGIP design analyzed by Poe with the as-built prototype with an impact velocity of 42 $\mathrm{m\,s^{-1}}$ on Ross Ice Shelf and Taku Glacier profiles. (a) Shows a simulation with only the fore-body. (b) Shows a simulation with the aft-body bonded to the fore-body.



(a) (b)

Figure 2-12: Comparison of impact conditions of the as-built SGIP prototype at a variety of impact velocities using nonlinear compaction model in the Taku Glacier with (a) only the fore-body. (b) the fore-body bonded to the aft-body.

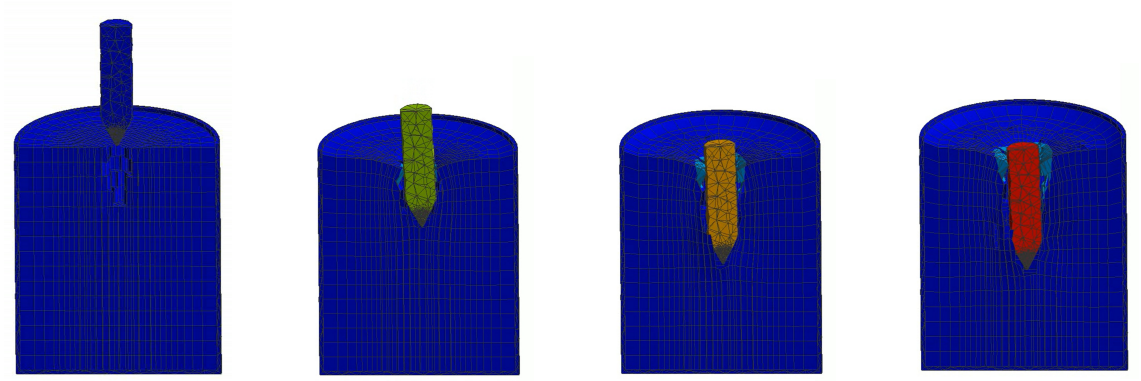
this model is only valid for soft snow and low density firn where granular interactions are minimal and where compaction is the dominant modality of energy absorption.

2.6 Finite Element Models

Since finite element analysis (FEA) models can model multiple modalities of energy absoption in impact media including compaction, fracture and frictional interactions, FEA methods can provide high fidelity simulations of impact events in more cases than the simplified analytical and empirical models previously covered. For small design studies, a three dimensional model was built in Ansys Explicit Dynamics 2021 R1 using practices developed by Poe [43].

2.6.1 Small Scale Model

To model results from small-scale drop testing into snow, a corresponding small-scale FEA model was constructed. This model has a rigid outer boundary condition in the shape of a 5 gallon bucket with a 0.38 m height and 0.15 m radius. Snowpack on the inside of the bucket was matched to relevant snow samples that were used during small drop testing. For instance, in the small drop tests conducted indoors with local Cambridge snow, densities were around 600 $\mathrm{kg\,m^{-3}}$. In this model the outer wall and penetrator were both modeled as fully rigid with snow bonded to the outer wall. These simulations had order of 15,000 nodes running in around 15 min on a 20 core desktop computer. These simulations were conducted with erosion control which eliminates nodes during material failure or if the simulation reaches minimum simulation time-step. As shown in Figure 2-13, average impact accelerations and penetration distances were shown to be similar to the analytical model and drop tests. While drop tests 1—10 showed significant cratering and spalling effects, simulations of small drop tests snowed no visible cratering or spalling. This is due to the FEA simulation modeling the snow as a bulk material rather than a set of particles.



(a) (b) (c) (d)

Figure 2-13: Small-scale three-dimensional finite element analysis model, with around 15k nodes, and dimensions matching the small-scale penetrator with paint bucket impact enclosure. This simulation shows an animation of drop 26, in Table 2.3, at times (a) 0 s, (b) 0.02 s, (c) 0.04 s, (d) 0.06 s.

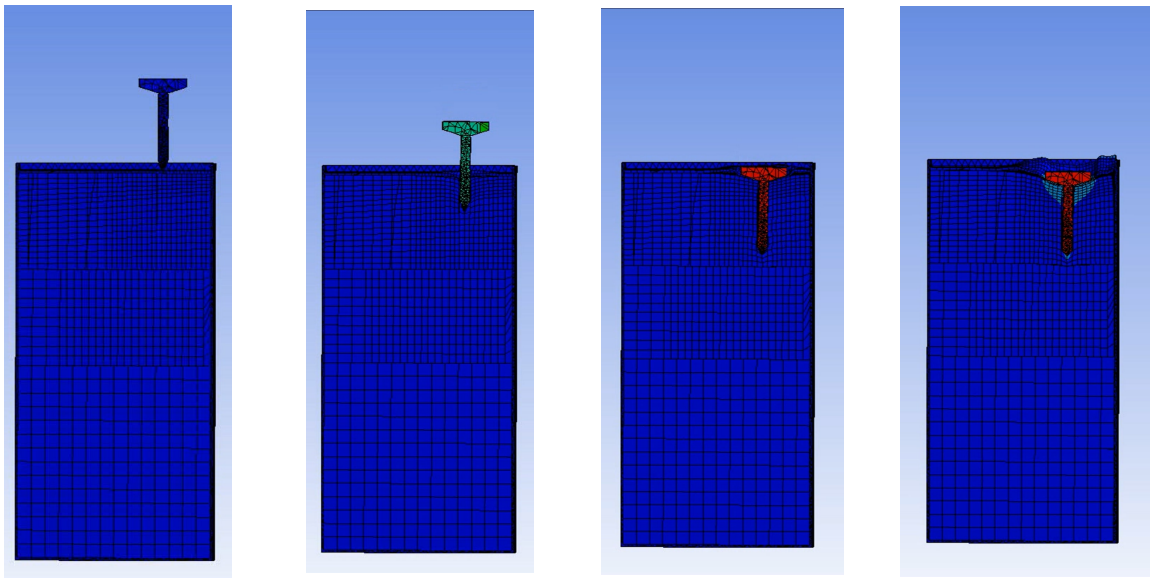
Table 2.3: Finite element model results in comparison to drop test data. Note that a similar distance traveled by the penetrator indicates a similar average acceleration. The discrepancies on drops 1 – 10 are likely due to significantly slushier snow compared to the material parameters in the FEA model.

Drop number	Snow density ($\mathrm{m\,s^{-2}}$)	Acceleration peak, modeled ($\mathrm{m\,s^{-2}}$)	Acceleration peak, tested ($\mathrm{m\,s^{-2}}$)	Distance, modeled (m)	Distance, tested (m)
4	606	419	160	0.21	0.30
5	624	395	267	0.22	0.20
6, 7	645	416	260	0.21	0.19
8, 9	663	544	287	0.18	0.18
17	See Figure 2-6	64	315	0.26	Not measured
26	See Figure 2-6	259	389	0.22	Not measured

2.6.2 Full Scale Model

In addition to the small-scale FEA model, a full-scale model was built to evaluate small numbers of impacts in more detail. The model implemented with the overburden, poisson ration, speed of sound and elastic modulus proprieties synthesized by Poe [43] using the density profiles detailed in Figure 2-2. The mesh ranges in size from 1 mm to 20 mm depending on the distance from the impact site. The penetrator and hard walls are modeled as rigid bodies, with the depth of the snowpack set to 8 m. Simulations were performed with both the aft-body bonded to the fore-body, and with only the fore-body. The bonded simulations are used to find an upper bound

for the shear pin forces for analysis such as that done by Brown [12]. The simulations with only the fore-body are used to understand the maximum depth of penetration.



(a) (b) (c) (d)

Figure 2-14: Full-scale three-dimensional finite element analysis model, with around 100k nodes. This simulation shows the as-built SGIP prototype impacting firn with the flare bonded to the fore-body to inform shear pin sizing at (a) 0 s, (b) 0.02 s, (c) 0.05 s, (d) 0.08 s.

2.7 Full Scale Testing at Juneau Icefield

While SGIP is originally designed for deployment and operation on the Ross Ice Shelf, Antarctica, shipping and transportation to Antarctica are slow and expensive; thus, the SGIP team decided to validate the structural prototype on the Juneau Icefield instead. The northwest branch of the Taku glacier was chosen due to its relatively flat topography, easy access from Juneau, prior crevasse surveying done by the Juneau Icefield Research Program, and a thick and consistent April snow pack similar to that expected on the Ross Ice Shelf.

2.7.1 First Test

The first full-scale drop test of the SGIP prototype was conducted on Juneau Icefield 5/10/2023. The system was attached to the helicopter hook with 30 m of tether, then dropped from the helicopter at an altitude of 2941 m at (58.63963N, 134.5554W) to an impact elevation of 1578 m at (58.62811N, 134.55916W). Conditions included a cloud ceiling around 2800 m with surface wind gusts up to 15 $\mathrm{m\,s^{-1}}$, and significant continuous wind at the drop height. During the drop, the penetrator was observed to rotate almost horizontal angle upon release before partially self righting; the penetrator began to roll significantly at a rate around 1 Hz and experienced oscillations in pitch and yaw around 50 °, as shown in Figure 2-15. This spinning continued until the snow spikes made contact with the snow pack. For this drop, the battery mass simulators were placed evenly throughout the fore-body, with center of mass of the fully assembled penetrator around 1.25 m from the nose tip (near the shear pin rails). During the spinning the penetrator was also precessing, leading to an impact angle of around 15 °. Due to this angled impact, the system had significant radial acceleration of up to 500 $\mathrm{m\,s^{-2}}$, leading to the shear pin blocks likely binding, then finally releasing. The peak acceleration experienced by the fore-body section was while the shear pins were still attached during binding at around 1000 $\mathrm{m\,s^{-2}}$. If not for the binding event, the likely maximum acceleration by the fore-body would be around 550 $\mathrm{m\,s^{-2}}$ as seen later in the acceleration profile. No video was recorded of this test due to camera tracking errors. Core data within 20 m the impact site are shown in Figure 2-2.

After the impact, the angle of the aft-body and mast were measured at 15 ° from the vertical axis at a depth of 0.09 m from the snow surface to the top of the aft-body. The angle of the fore-body after impact was measured at 25 °, with the depth of the nose at 2.5 m. Acceleration and orientation profiles during the impact stage are pictured in Figure 2-16 with the $t = 0$ in both plots corresponding to when the penetrator made contact with the surface. A set of photos after the impact are shown in Figure 2-17. Core data from the impact are shown in Figure 2-2. During

recovery, it was observed that there was a very noticeable increase in density around the penetrator, including a thick layer caked to parts of the fore-body.

Upon post-drop inspection, several components were damaged including the bottom joints which support the SGIP antennas mast; an analysis of these joints with suggestions for a material change is presented in Section 3.5. The flare panels experienced significant deformation, with many underside rivets popped out. One of the shear pin rails was bent significantly, likely due to limited binding during the angled and rotating impact, as analyzed in detail by Brown [12].

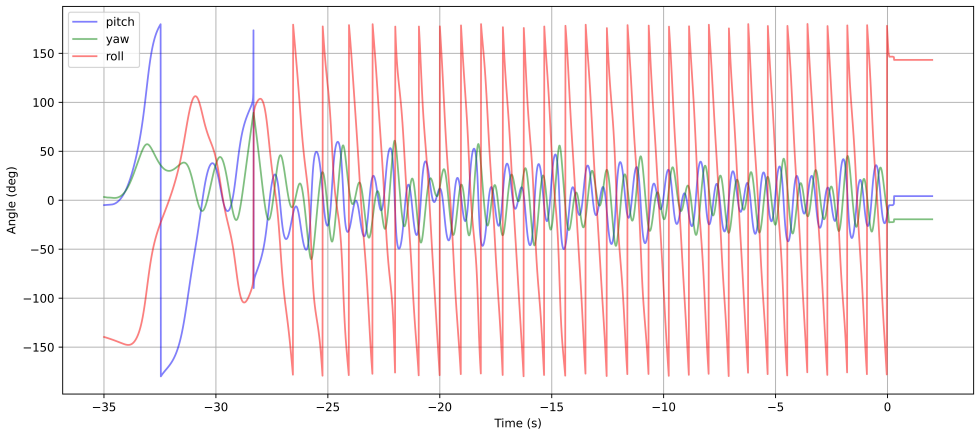


Figure 2-15: Orientation profile for SGIP entire prototype drop 5/10/2023 test drop onto the Taku Glacier, Juneau Icefield. The penetrator experienced axial roll rotation around 1 Hz for the last 27 s of the drop, with significant yaw and pitch oscillations.

2.7.2 Second Test

The second full-scale drop test of the SGIP prototype was conducted on Juneau Icefield 5/16/2023. After the first drop, the bent shear pin rail was bent back into place, and all of the battery mass simulators were moved to the first two battery racks, shifting the penetrator center of mass of the fully assembled penetrator downward to 1.04 m from the nose tip. Additionally the mast and snow spikes were removed; this reduced the total drop mass from 132 kg for the first drop to 118 kg for the second drop. Instead of attaching the 30 m helicopter tether to the lanyard through the mast, the lanyard was attached to a tie-point in the middle of the aft-body section.

The penetrator was released from an altitude of 3119 m at (58.62842N, 134.55806W), where it fell to an impact elevation of 1598 m at (58.62842N, 134.55806W). Compared to the first drop, wind conditions were much calmer, with little wind at the drop height.

During the drop, the penetrator experienced a 0.25 – 0.5 Hz oscillation in pitch and yaw at a maximum amplitude of 20 °, which dampened over the first 30 s to < 5 °. After the impact, the angle of the aft-body and mast were measured at 5.3 ° from the vertical axis. The angle of the fore-body after impact was measured at 10.9 °, with the depth of the nose at 2.25 m. A set of photos after the impact are shown in Figure 2-21. Core data 4.9 m from the impact site are shown in Figure 2-18. Due to a set-up error, no acceleration data were taken during this drop. During recovery, as with the last drop, it was observed that there was a very noticeable increase in density around the penetrator, including a thick layer caked to parts of the fore-body.

Between the first and second drop, there were three main changes that may have reduced the rolling motion of the penetrator; these changes are the removal of snow spikes, removal of the mast, and the lowered center of mass. Since in a three-dimensional system, pitch, yaw and roll are all coupled, moving the center of mass downward increases stability in all axes. Wind tunnel testing of the penetrator in Section 4.3.3 with more detailed analysis by Makikalli [37] contextualized the drag forces and rotational moments with and without snow spikes. The GNSS antenna mounted on top of the mast is a significant off-center drag surface, shown in Figure 3-3; this antenna is nominally in the low-pressure zone behind the aft-body, but during high pitch event such as that at the beginning of drop 1 in Figure 2-15, the mast was tilted into higher pressure zones several times, possibly contributing significantly to rotation. In Figure 2-15 that the rolling motion started during the first 10 s of the first drop, when the pitch and yaw angles were highest, and did not increase as significantly in rate once the penetrator was near vertical. Thus, in future iterations, it is recommended to move the center of mass downwards by reducing aft-body mass, and to further investigate GNSS antenna placement and snow spike symmetry. The alternative snow spike design in Figure 4-2 is symmetric and has only moderately

worse performance. Additionally, lightweight aerodynamic stabilization fins could be added to further reduce the possibility of rotation.

After the drop testing on Juneau Icefield, results of the drop acceleration profiles and measured final depths may be compared to model predictions. With the measured density profiles from the drops in Figure 2-18, the as-built penetrator geometry, and a drop velocity set to 42 $\mathrm{m\,s^{-1}}$, predicted drop trajectories with the nonlinear elastic compaction model are depicted in Figure 2-19. The real-world drops exhibited much lower penetration distances compared to the model; this is likely due to the large lateral accelerations involved in the impacts as well potential binding on the shear pins. Additionally, the nonlinear elastic compaction model predicts an especially far penetration for Alaska drop 1 because the lowest value of the measured density profile, around 320 $\mathrm{kg\,m^{-3}}$ is extrapolated to the rest of the impact depth > 2.1 m.

2.8 Conclusions and Discussion

The successful series of full-scale drop tests performed in Alaska were a culmination of several years of impact modeling and testing. In this section, several impact models for snow are implemented and compared, including the Young model, a nonlinear elastic compaction model, and an explicit finite element dynamics model. These models are further compared to small-scale drop tests, with a significant corpus of acceleration time-series data.

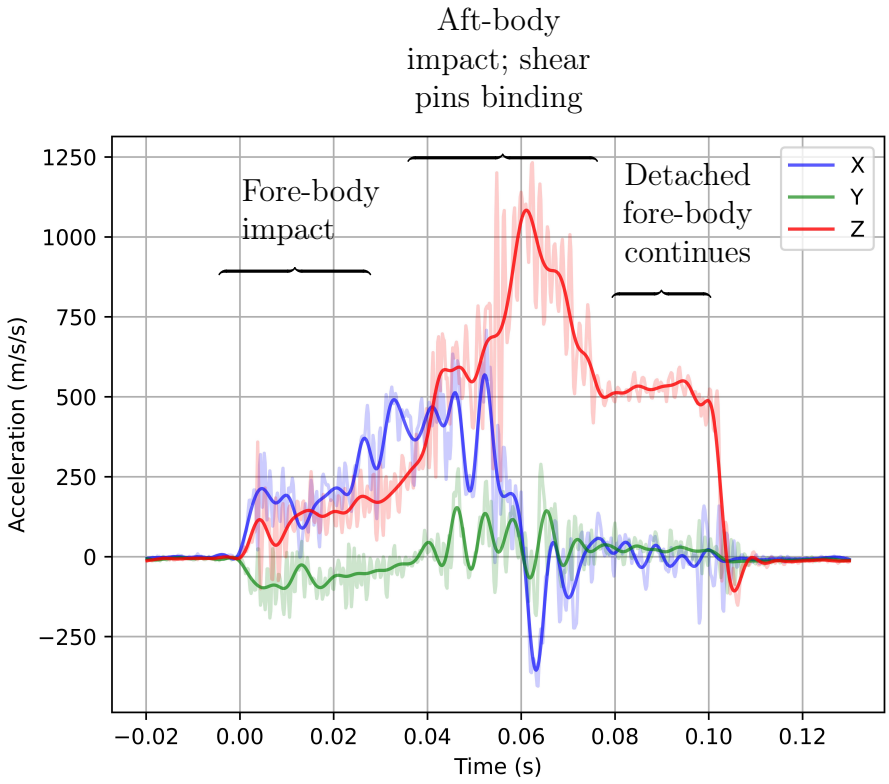
While these models are in the beginning stages of validation, future work remains to further validate the models. For instance, more small-scale drop tests were performed on the Taku Glacier which have yet to be analyzed. In addition, a more formal discussion of non-dimensional scaling laws such as the one performed by Wang [57] could add significant context to the small-scale drop test data and procedures. The nonlinear elastic compaction model could be taken even further by building a simple map application to use it for site mapping and drop area selection.

While the models discussed in this chapter are interested in the most basic impacts, further investigation of angled impacts would be useful for determining operating

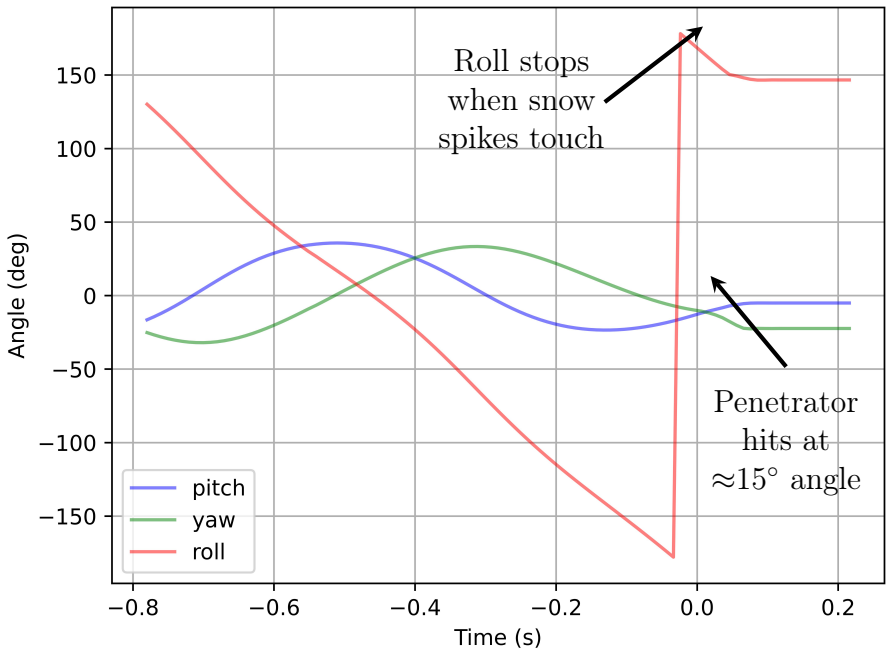
conditions. The finite element impact models here and by Poe [43] model some types of energy absorption during a tipping event, but a particle-based method such as MPM [54] or iSALE [16] could give much higher fidelity answers to specific impact-related questions.

Perhaps the most important future work of all is to simply drop more full-scale models, in well-documented snow pack, instrumented with a full suite of high speed cameras, and an accelerometer in both the fore-body and aft-body. Despite the success of the drop tests described in Section 2.7, both tests were missing important data sources; further testing should prioritize testing all data acquisition equipment thoroughly before the drop.

In future iterations of SGIP, impact performance may be further improved by reducing the radius of the fore-body or increasing $\frac{l_{nose}}{r_{penetrator}}$. While reducing the radius of SGIP is unlikely due to the seismometer size constraints, there are almost no negative systems implications of implementing a more-pointed nose section.



(a)



(b)

Figure 2-16: Acceleration profiles (a) and orientation (b) of SGIP during first full-scale prototype test drop on Juneau Icefield 5/10/2023. The $t = 0$ point in both plots corresponds to when the penetrator made contact with the surface. Acceleration profile in (a) is filtered with a 20 Hz low-pass filter in solid colors for clarity, with the original in the background.



(a) SGIP aft-body viewed from a distance after impact; evidence of cratering is minimal.



(b) Close-up view of SGIP antenna mast after initial clearing of snow on the left.



(c) Side-view after initial digging to remove SGIP showing the successful separation of the fore-body and aft-body.

Figure 2-17: Images from 5/10/2023 first test drop onto the Taku Glacier, Juneau Icefield.

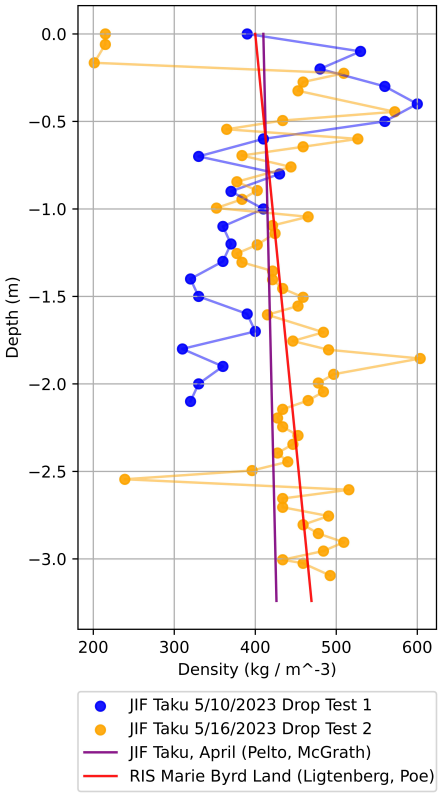
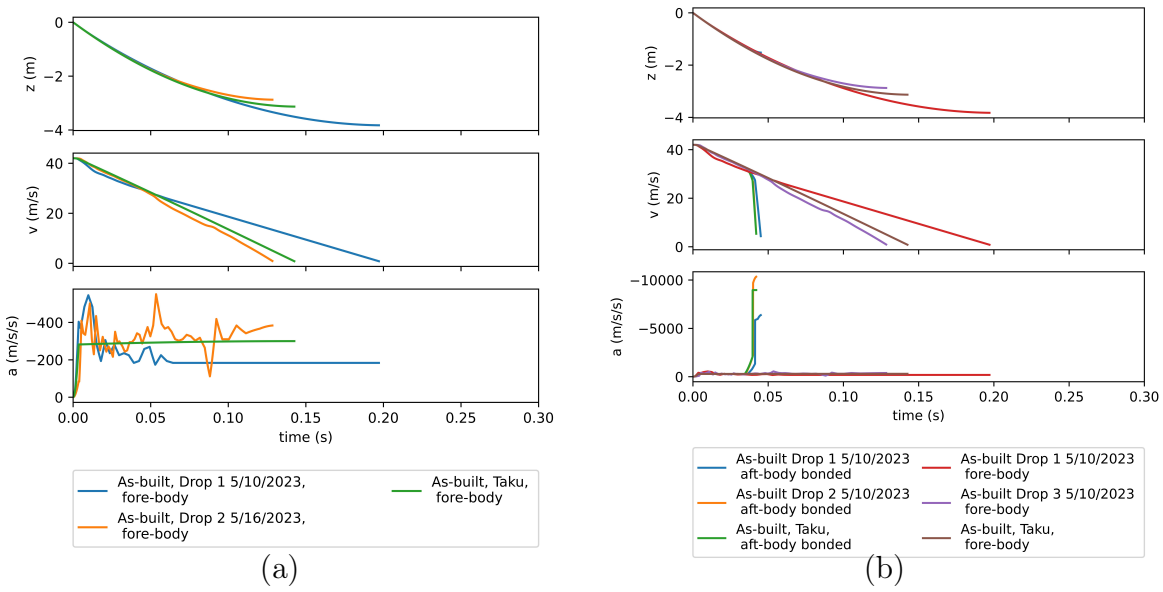


Figure 2-18: Snow and firn density profiles used for modeling SGIP impact with measured snow density from SGIP drop testing on Taku Glacier 2023.

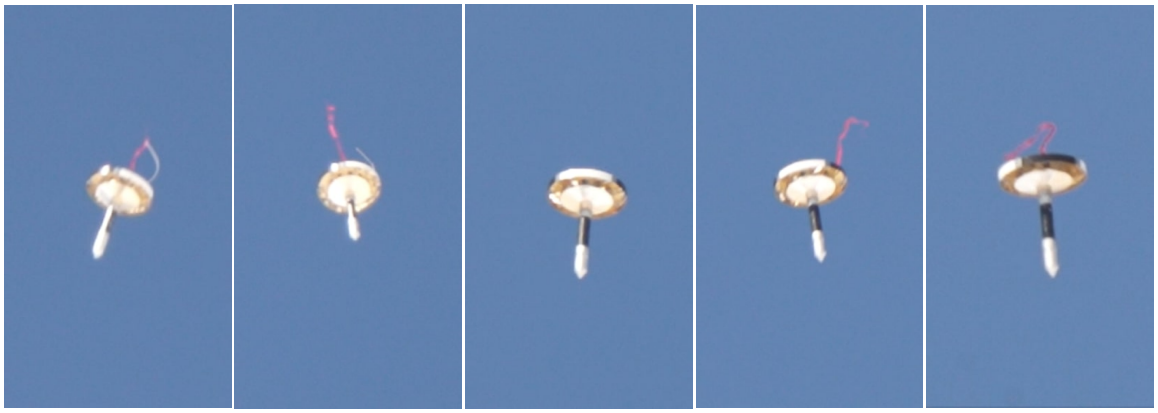


(a) (b)

Figure 2-19: Nonlinear compaction model run on the measured profiles on from the SGIP Taku Glacier shown in Figure 2-18 at an initial velocity of 42 $\mathrm{m\,s^{-1}}$ in comparison to the generic profile of the Taku Glacier (a) with only the fore-body section. (b) with both the fore-body and the fore-body bonded to the aft-body "flare".

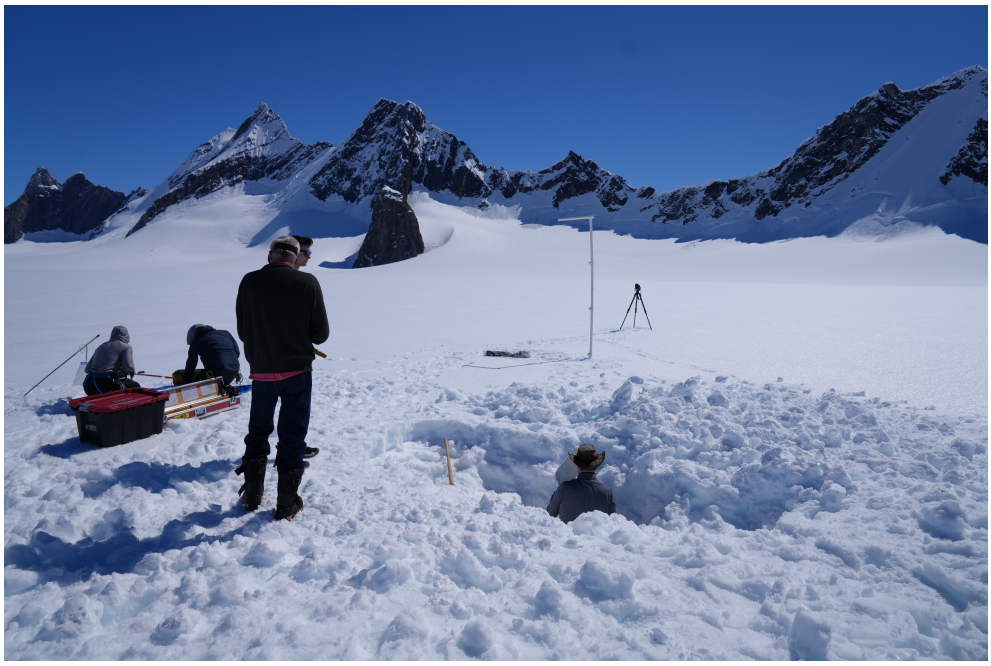


(a) Before drop

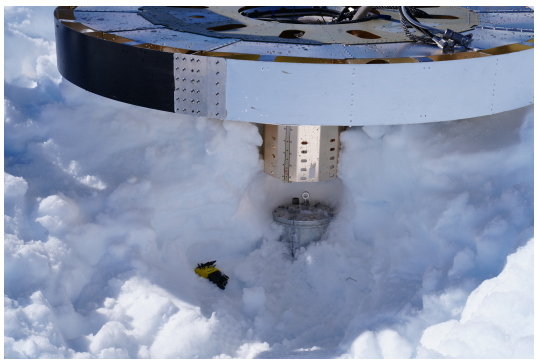


(b) 2 sec (c) 4 sec (d) 21 sec (e) 22 sec (f) 26 sec

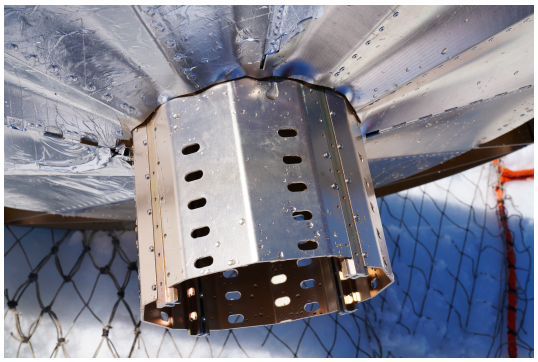
Figure 2-20: Images from drop stage of the 5/16/2023 second test drop onto the Taku Glacier, Juneau Icefield. SGIP experienced a 0.25 – 0.5 Hz oscillation in pitch and yaw during the drop at a maximum amplitude of 20 °, which dampened over the first 30 s to < 5 °. Images (b) – (f) were taken at the maximum amplitude of oscillation during each time of the drop, showing the dampening effect.



(a) Post-drop recovery process for SGIP prototype, digging a snow pit to retrieve the aft-body (center), retrieving, cutting and measuring a snow core sample (left), and dropping the small-scale penetrator model from a 3 m PVC pipe tower (rear).



(b) Side-view after initial digging to remove SGIP showing the successful separation of the fore-body and aft-body, with the umbilical disconnected.



(c) Close-up side-view of shear pin blocks and underside of aft-body after both impacts, showing bent aft-body panels.

Figure 2-21: Images from 5/16/2023 second test drop onto the Taku Glacier, Juneau Icefield.

Chapter 3

Design, Analysis and Testing of Antenna Mast for Ice Penetrator

3.1 Design of Antenna Mast

3.1.1 Motivation

To support the main goals of retrieving GNSS and seismic data from Ross Ice Shelf, those data must be successfully collected from a GNSS receiver and transmitted via Iridium to the SGIP operations team for the full year-long duration of the deployment. In this operations window, antennas must be held elevated above the height of Ross Ice Shelf annual snow accumulation, implying the need for a structure which rises above the aft-body flare. The Ross Ice Shelf experiences a maximum annual snow accumulation of ≈ 0.5 m; however, snowpack height varies greatly due near surface features due to blowing snow, and an antenna system with a height of >1 m is proposed to mitigate these effects [18][30][48]. In this section, the design of a antenna mast is derived with a focus on finding a low cost, easy-to-prototype solution which meets system requirements.

The SGIP antenna mast structure has important roles during all parts of SGIP operation. These roles are delineated and quantified in Table 3.1 as a companion to the following qualitative description. These specifications are derived from relevant

requirements compiled in Table 3.2. During the helicopter lifting and transport phase, a lanyard must pass through the mast, connecting the helicopter lifting hook to an eye-bolt on the fore-body. It is critical that the aft-body and antenna mast do not bear significant load during the helicopter lifting and transport phase to avoid loading the shear pins that connect the fore-body and aft-body. While SGIP is being released from the helicopter, the helicopter hook must release cleanly from the lanyard and stay clear of the antennas and mast structure. During the free-fall phase, the antenna mast must not interfere with SGIP's stable aerodynamic characteristics. While SGIP impacts the top layer of firn, the mast structure must be able to support the mast of the GNSS and Iridium antenna without buckling or getting damaged; furthermore, the shock transmitted to the antennas must be within an acceptable operations range. After the impact, the SGIP mast needs to keep the GNSS receiver antenna within sufficient positional accuracy to take geodesic quality measurements, even during high winds and must provide routing options to low-loss coaxial cables to support these antennas. Over the course of deployment the mast must not consume power to stay stationary, and must continue to support the SGIP Iridium and GNSS antennas above the height of the seasonal snow accumulation for the course of a full year.

3.1.2 Prototype Mast Design, Detailed

Meeting the specifications in Table 3.1, a design which incorporates fiberglass tubing as the primary structural elements with nylon 3D printed joints and a bent sheet aluminum payload deck was selected for further evaluation and prototyping. This mast design is pictured in Figure 3-1.

Structural fiberglass tubing offers an excellent strength to weight ratio, while being available in commercially-available form factors which allow for rapidly-scalable designs. Additionally, simple tube shapes lend themselves to standard buckling and aerodynamics calculations, increasing confidence in the design for the extreme environments involved. The mast structure is composed of three main structural fiberglass elements in a radially symmetric pattern, each angled at 6 ° to increase lateral rigidity; in addition to these main structural elements, a fiberglass guide pole

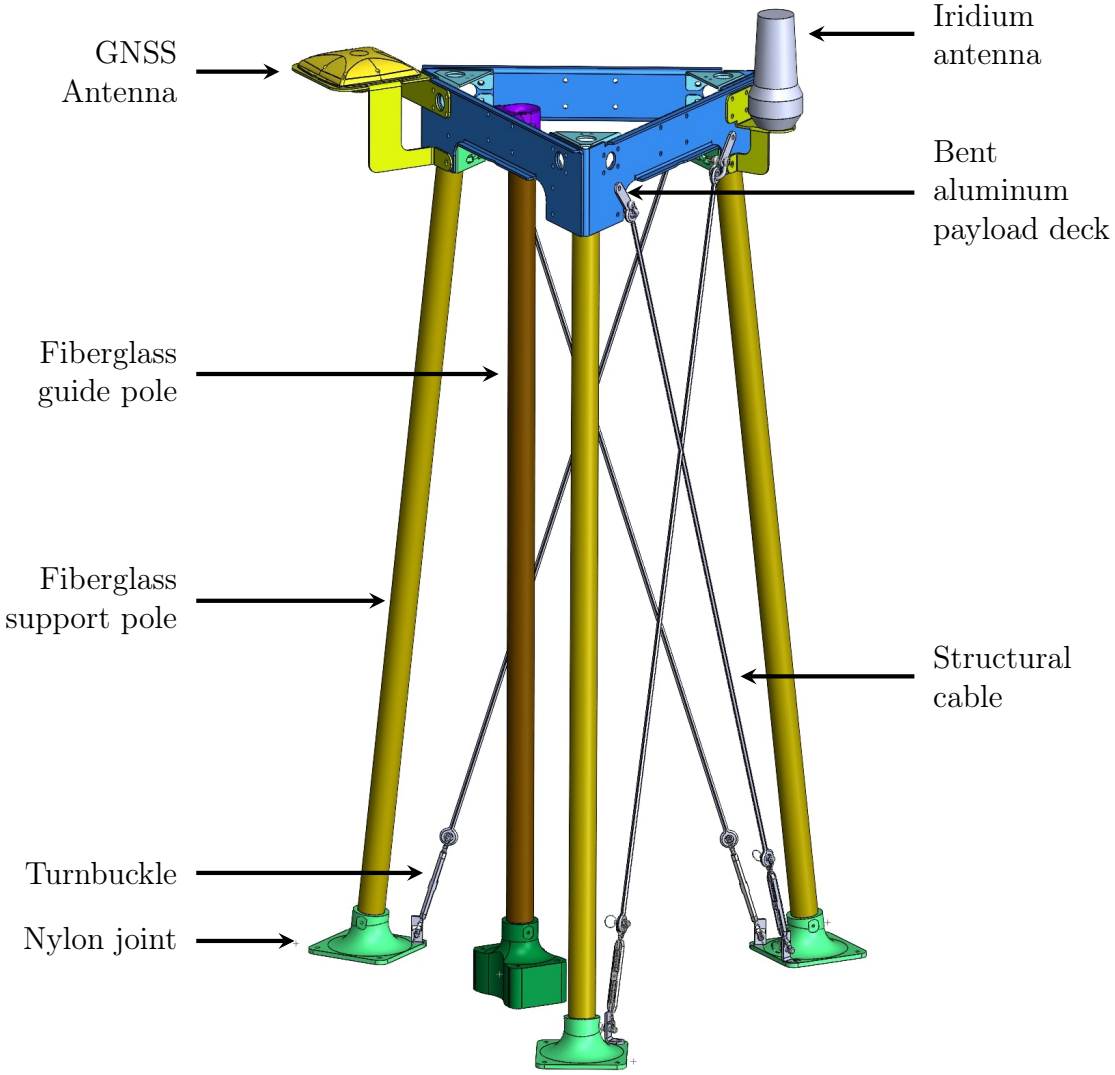


Figure 3-1: SGIP antenna mast design pictured in an angled view with major components labeled.

Table 3.1: Specification for SGIP antenna mast with corresponding driving requirements.

Category	Associated Requirement	Specification	Additional reasoning
Payload	PAY.1, PAY.11, COM.1, PAY.7	The mast must be able to carry a GNSS and Iridium antenna, and other environmental sensors.	NA
Tip Deflection, Wind Load	PAY.2, STR.1	At a maximum wind speed of 35.4 $\mathrm{m\,s^{-1}}$, maximum deflection of the top of the mast from vertical should be 10 cm or less.	Needed to get accurate GNSS position readings, since the GNSS receiver antenna is at the top of the mast.
Radial Deflection	TRAN.1 (pending)	The top of the mast must be able support the mass of the penetrator loaded radially.	The mast must withstand the weight of the penetrator while being lifted into the helicopter. This means that a lanyard may be loading the top part of the mast.
Minimum Height Above Snow	A.11	System must be over 1 m tall.	Above typical seasonal snow accumulation in Antarctica [18][30][48].
Electrical Cable	A.2, A.3	System must satisfy the minimum bend radius of a coaxial cable; around 8 cm, and support electrical cables for GPS, Iridium, ground cable and temperature sensor cables.	Minimum bend radius specification. [3]
Shock/Impact	STR.1	System must withstand 8000 $\mathrm{m\,s^{-2}}$ of shock.	Provide >1.6 safety factor for 5000 $\mathrm{m\,s^{-2}}$ impact onto in Antarctic firn.
Shock Absorption	A.10	System must provide shock absorption to GNSS and Iridium antennas to limit impact loads to under a 2 meter drop test on cement, or alternatively the IEC60068 specification.	Specified by antenna manufacturer [2].
Maximum height	AER.1	Mast system must be under 2 m tall.	Clearance for helicopter lifting.
Power	A.4, PWR-1	Power, if used for mast, must be self-contained in mechanical springs, primary chemical potential energy sources.	Main batteries on SGIP have limited capacity.
Capacity	A.2, A.3	The system should be able to support 4.0 kg of payload including the weight of the payload deck.	The payload carried will be a Topcon PG-F1 GNSS Antenna and an Iridium AT1621-142 Mast Antenna. Since the antennas together weigh 1.58 kg this requirement accounts for a wide design space of payload decks.
Aerodynamics	AER.1	SGIP must stabilize in no more than 5 s longer with the mast system than without the mast system during helicopter drop.	NA
Manual Deployment	A.7	System must be statically deployed or have a method of deploying manually,	In event of deployment failure, humans should be able to deploy the mast to test the rest of SGIP.
Passive Locking	A.4, PWR-1	System must be statically deployed, or must passively lock in deployed position.	Main batteries on SGIP have limited capacity.
Payload	PAY.1	The geodetic data shall be collected continuously.	
Payload	PAY.11	The orientation (tilt) of the GNSS antenna shall be measured to $\pm$ 1 $^\circ$	

adds further axial strength. To connect the SGIP unit to the helicopter hook during the transport and drop phases of operation, a Dyneema sling runs runs to an eye-bolt on the fore-body, through the aft-body, through the fiberglass guide pole to the helicopter hook. Since there are no connections from the lanyard to the aft-body or antenna structure, the fore-body/aft-body shear pins are not loaded during lifting. During the impact, the lanyard is pulled through the the guide pole unimpeded.

The fiberglass tubing components are joined to the aft-body and payload deck using a set of glass-bead-filled Nylon 12 multi-jet-fusion (MJF) 3D printed

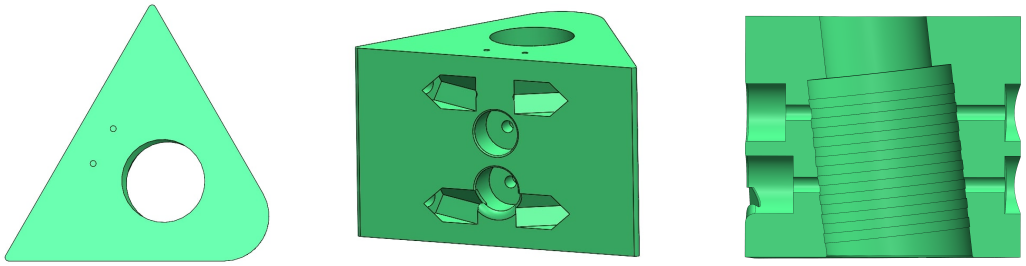
Table 3.2: Relevant Requirements for SGIP Antenna Mast.

Category	Number	Requirement
System Level 3	A.10	Survive impact with ice shelf from air drop
System Level 3	A.11	Survive and operate in Antarctic environment for one year
System Level 3	A.2	Collect broadband seismic data from the RIS
Payload	PAY.2	The geodetic data shall be geodetic-quality GNSS observables
System Level 3	A.4	Distribute stored power to operate continuously and autonomously
System Level 3	A.7	Be operated by a two-person team and weigh no more than 100 kg
Aerodynamics	AER.1	The penetrator shall have sufficient aerodynamic stability during flight to be able to dampen external aerodynamic forces to control trajectory
Power	PWR-1	The power system shall supply a continuous source of electrical power to all subsystem loads within their current and voltage operating ranges
Communications	COM.1	The system shall transmit and receive data from communications satellites
Communications	COM.6	The comms (active) system will be located to provide sufficient RF isolation to the GNSS (passive) system
Structures	STR.1	The system shall maintain structural integrity in all Antarctic conditions.
Thermal	THR.1	The system must be capable of operations within its survivable temperature range.
Payload	PAY.7	Meteorological variables (temperature, pressure, and humidity) shall be measured continuously.
Payload	PAY.1	The geodetic data shall be collected continuously
Payload	PAY.11	The orientation (tilt) of the GNSS antenna shall be measured to $\pm$ 1 $^{\circ}$.

components, pictured in Figure 3-2, with an adhesive and rivet interface to the tubing and a simple bolt interface to the aft-body and payload deck. MJF Nylon 12 printing was chosen for its toughness, acceptable isotropy (only slightly lower than selective laser sintering and significantly higher than fused deposition modeling), and compatibility with many classes of adhesive [40][59].

The joint components have a standardized ridge pattern which retains glue on the interior. During assembly, glue is applied, the tube is fitted into the joint, then holes are drilled for blind rivets and rivets are placed which keep the structure static while the adhesive is drying. For this application, Masterbond EP40ND adhesive was selected for its elastic properties, resilience to cracking, adhesion to both materials, and a rated temperature range of -73.3 to 176.7 °C [5]. Four different variations of these joint structures were designed, all with the same tubing interface, as shown in Figure 3-1.

At the top of the mast structure is a payload deck, viewed in Figure 3-3, composed of three identical sheets of laser cut and bent 5052 3.15 mm thick aluminum. This structure has a set of bent tabs designed to increase torsional rigidity of the structure, and is braced by six identical interior corner braces as shown in Figure 3-4 (a). GNSS and Iridium antennas rest on separate detachable mounts, which can be easily replaced and other sensors and antenna structures can be added. The GNSS antenna is placed nearest to the guide pole, since its low profile shape is least likely to snag on the helicopter lanyard, and the guide pole provides extra support since the GNSS antenna is the heavier payload. Due to its taller height the Iridium antenna was placed as far away from the guide pole as possible and at the lowest height possible while still elevating the interior antenna element above the grounded aluminum payload deck. The guide pole interface block features a significant chamfer to prevent lanyard swinging and twisting during the impact. The shape of the payload deck was designed to place most of the sheet metal components in the vertical configuration to have high rigidity during axial loads and to minimize snow accumulation. Wiring for the antennas can be routed through holes in the aft-body through the mast joints and structural fiberglass tubing up to the payload deck; holes in the GNSS and Iridium antenna mounts facilitate cable routing with over 8 cm bend radius. In addition to the larger antenna mounts, smaller sensors may be mounted inside of the aluminum corner brace pieces such as a proposed temperature and barometric pressure sensor. To improve antenna performance and to prevent large voltage potentials to form between the payload deck and the aft-body, a ground wire will run from the antenna



(a) Top view. (b) Angled front view. (c) Cross-section side view.

Figure 3-2: Top tubular interface joint design featuring a ridged gluing interface, captive nut interfaces to the payload deck and holes for rivets to be used during assembly.

structure down to the aft-body.

To further increase torsional rigidity of the structure, a set of four 3.15 mm thick stainless steel cables is fastened to the structure with quickly removable shackles and turnbuckles for tensioning. The cable structures are placed on the sides of the mast structure without the guide pole to reduce the likelihood of tangling the helicopter lanyard. To prepare for field operations, the mast structure can be disassembled by removing the structural cables, and unbolting the tubing interface blocks from both the payload deck and the aft-body. Similarly, replacement fiberglass structural tubes may be prepared by gluing to extra interface joints in advance of field testing. Interfaces from the mast to the aft-body and antenna systems are detailed in Table 3.3.

3.1.3 Previous Design Iterations of Static Mast

Pre-Preliminary Design Review (PDR) Version (V1)

The first SGIP static mast design, pictured in Figure 3-5, consisted of a series of G10 fiberglass tubes, joined to top and bottom plates via 3D printed pieces. One major consideration was being able to use a universal 3D printed part for as many of the plate-to-tube interfaces as possible to speed prototyping, and to decrease the cost of larger scale manufacturing. A second consideration was designing for minimum total part count; thus, the top plate was designed as a structural element which

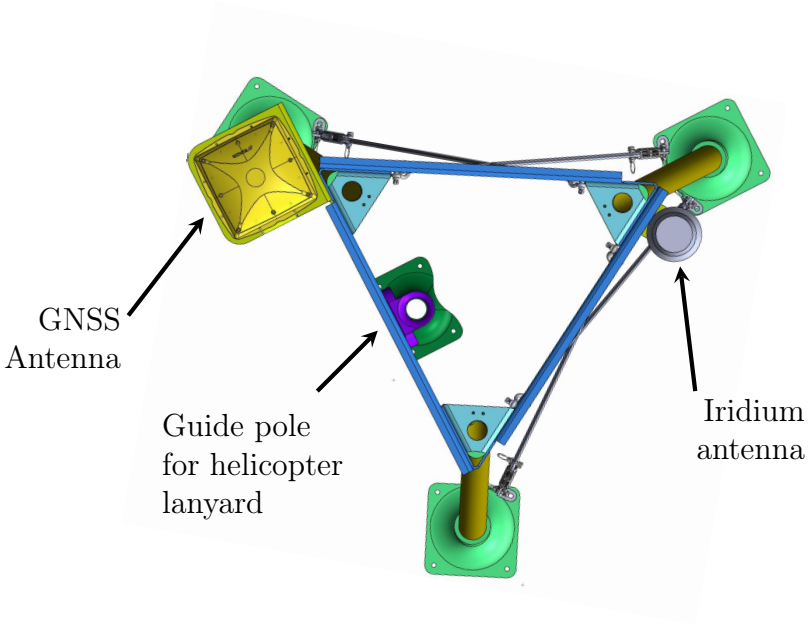


Figure 3-3: Top view of SGIP antenna mast featuring GNSS antenna, Iridium antenna and guide pole.

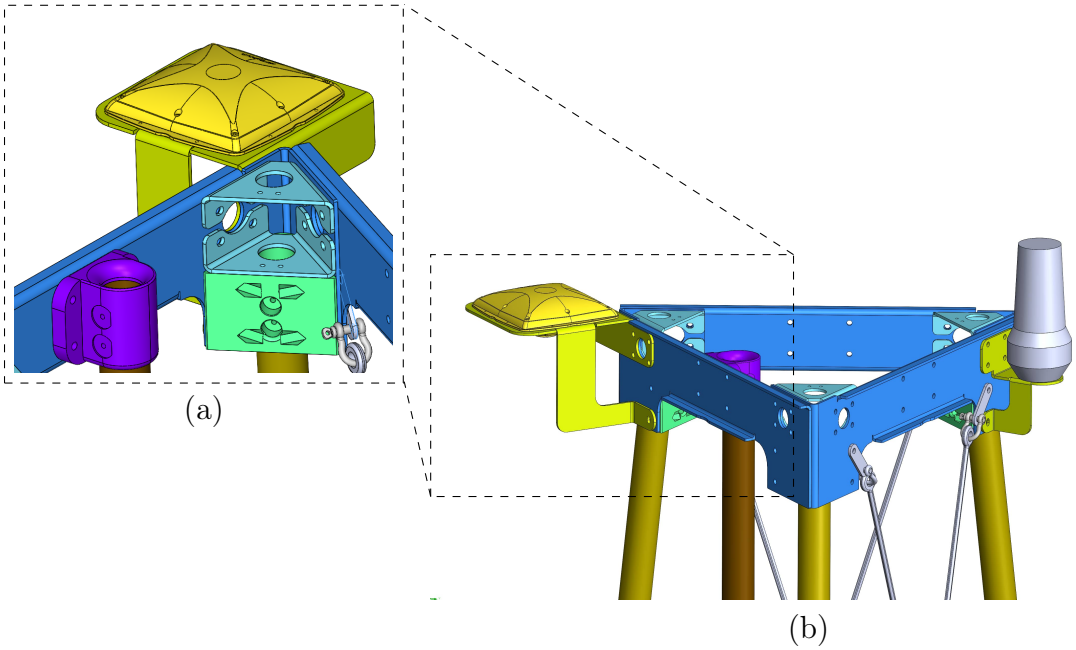


Figure 3-4: Closeup (a) of interior payload deck structure (b), showing corner braces, GNSS mounting, holes for wire routing and chamfered guide for helicopter lanyard.

would also hold all of the antennas. An optional radome was designed to prevent the helicopter hook from directly contacting the antennas and to help shed snow from the

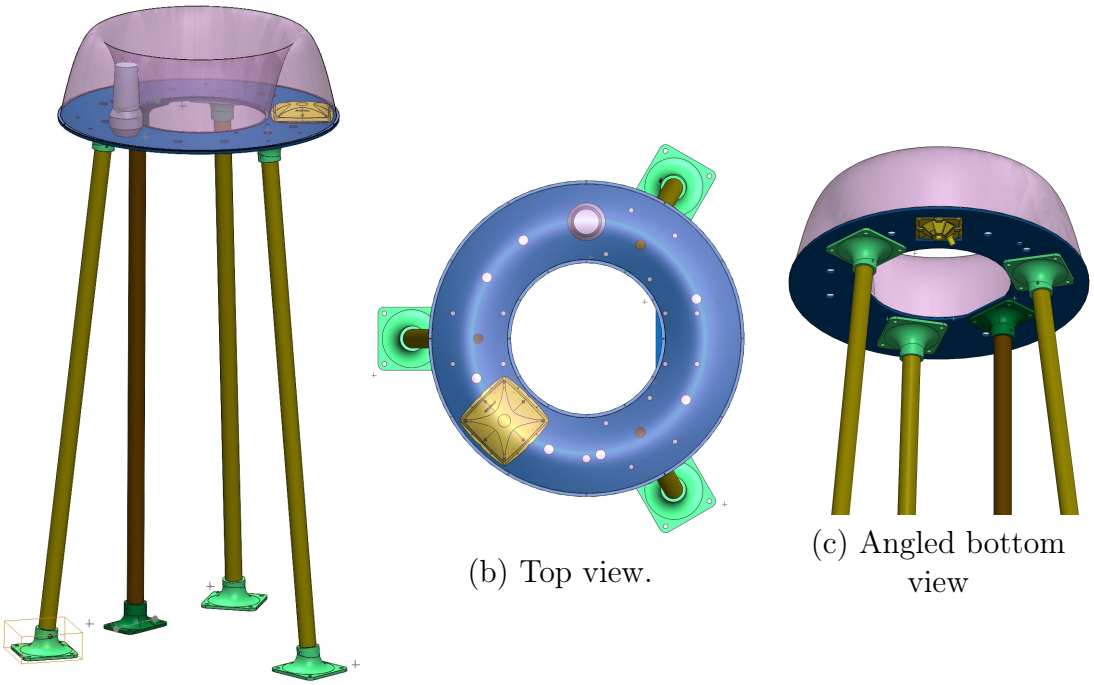
Table 3.3: Interfaces for SGIP Antenna Mast

Category	Interfaces with:	Details:	Additional Reasoning
Mechanical	Flare	• The flare must have a pre-arranged pattern of 3/8in-16 tapped holes • Flare must be flat on top. • Flare must be at least 6.35 mm thick to accept tapped holes.	NA
Mechanical	Sling	• The lanyard hook structure must fit through a 30 cm diameter hole • Lanyard hook structure must have a mass of less than 1 kg.	Needed to get accurate GNSS position readings, since the GNSS receiver antenna is at the top of the mast.
Mechanical	Antennas	• Iridium antenna will be mounted with a $\frac{3}{4}$ NPT threaded pipe segment, which will be secured using an NPT nut. • GNSS Antenna will be mounted with a hole pattern of 8 holes to the GNSS antenna flange. An additional 5/8 hole mounting option can be arranged. • Additional sensors may be mounted in the mast box section with an equilateral triangular footprint equal to that of the mast corner braces, and a height of 5 cm or less. Alternately these sensors may be accommodated with an add-on bracket with area less than 25sq in.	The mast must withstand the weight of the penetrator while being lifted into the helicopter. This means that a lanyard may be loading the top part of the mast.
Electrical	Antennas and sensors.	• Antennas will use LMR-400 COAX Cable or smaller, with one-time bend radius less than 28mm. • Other sensor wires will fit into a cable with 7mm or smaller, with a one-time bend radius less than 28mm. • Cables will be secured with cable glands within the mast system for strain relief. • Additional sensors will have cable diameter of 7mm or smaller.	Above typical seasonal snow accumulation in Antarctica.

top structure. This design was presented at a PDR on 07/05/2022; the feedback from the greater SGIP team was mostly positive, with the principle major concern being that the large area of the top plate, 0.2294 m^2, could cause significant accumulation of snow around the antennas.

Post-PDR Version (V2)

After the PDR, the concept went through a minor revision, resulting in the version which was then prototyped and tested. The new mast design was based on a very similar fiberglass tube and 3D printed joint construction to the original static mast design, but features a new payload deck design. The payload deck was designed to have a significantly smaller area of 0.062 m^2 rather than the previous 0.2294 m^2 to prevent snow accumulation. Additionally, the structural elements in the payload deck have a higher area moment of inertia to increase structural rigidity, cleaner paths for



(a) Angled side view.

(b) Top view.

(c) Angled bottom view

Figure 3-5: Pre-PDR version 1 of SGIP antenna mast, featuring antenna radome. The mast was redesigned to have less area for snow accumulation and a more rigid upper boundary condition.

internally routed cables, more adaptable removable antenna mounts, and increased rigidity of the tube-to-structure joints.

3.2 Analysis of Static Mast

To mitigate operational risk and increase understanding of the mast's performance characteristics, a series of analyses were performed. While testing is usually superior to analysis in risk mitigation for extreme environment applications, analysis promotes coverage of cases which are too difficult or expensive to test in their entirety while further informing which scenarios are most worthy of increased testing or design modification.

3.2.1 Buckling Calculations: Axial Loads

The main load case of the static mast is during impact of the penetrator into the ice shelf. During this event, the mast is loaded axially, with the mast responsible for supporting the payload. To sustain operations on the ice shelf after impact it is important that the mast is not damaged by the impact. To evaluate the resiliency of the mast to the impact acceleration event, the buckling load of the mast is calculated. Note that the structure would reach a buckling load before it fails, and that the buckling calculation provides a theoretical lower bound for mast tubing failure.

Hand Calculation

A hand calculation is performed using the Euler buckling method. For simplicity, a single supporting fiberglass beam in the mast structure is considered, as if it were positioned vertically. These results will then be interpreted for the full mast subsystem.

The area moment of inertia for cylindrical tubing is calculated in Equation (3.1). When values are applied to variables, they are assigned for all further uses of that variable unless stated otherwise.

$$I_{pipe} = \frac{\pi(D_{OD}^4 - D_{ID}^4)}{64} \quad \approx 5.3 * 10^{-8} \quad \text{m}^4 \tag{3.1}$$

where

$D_{OD} \approx 0.0381$ m, the outer diameter of the tubing.

$D_{OD} \approx 0.0317$ m, the inner diameter of the tubing.

Using this result, the radius of gyration is computed in Equation (3.2)

$$k_{gyration} = \sqrt{\frac{I}{A}} \quad \approx 0.0062 \quad \text{m} \tag{3.2}$$

where

$A \approx 0.0014$ m^2, is the cross sectional area of the tubing.

The slenderness ratio calculated in Equation (3.3) depicts the ratio of the effective length of the buckling structure to the radius of gyration; thus a higher slenderness ratio implies a longer and narrower structure.

$$S_{slenderness} = \frac{KL}{k_{gyration}} \quad \approx 210 \tag{3.3}$$

where

$K \approx 1.0$, which is selected to model a fixed boundary condition on the base of the tube, and a free boundary condition at the top of the tube, a conservative assumption considering the payload deck structure of the real system [50].

$L \approx 1.3$ meter, the measured length of the structure.

The critical slenderness ratio below which the Euler buckling approximation isn't applicable is given by Equation (3.4).

$$S_{critical} = \sqrt{\frac{2\pi^2 E}{\sigma_{yield}}} \quad \approx 36 \tag{3.4}$$

where

$E \approx 27 * 10^9$ Pa, is the elastic modulus of the material [26][17].

$\sigma_{yield} \approx 4.13 * 10^8$ Pa, is the fiberglass yield stress [26][17][1].

Noting that slenderness ratio, $S_{slenderness}$ is much higher than $S_{critical}$, the Euler buckling approximation is appropriate in this case. Given these parameters, the critical force under which the beam will buckle is calculated in Equation (3.5).

$$F_{crit} = \frac{\pi^2 EI}{(KL)^2} \quad \approx 8444 \quad \text{N} \tag{3.5}$$

For a possible example payload mass, the acceleration that the structure will buckle at may be calculated for a set of four of these beams.

$$a_{crit} = n_{tubes} \frac{F_{crit}}{m_{payload}} \quad \approx 8444 \quad \text{m s}^{-2} \tag{3.6}$$

where

$n_{tubes} = 4$, the number of tubes in the mast structure.

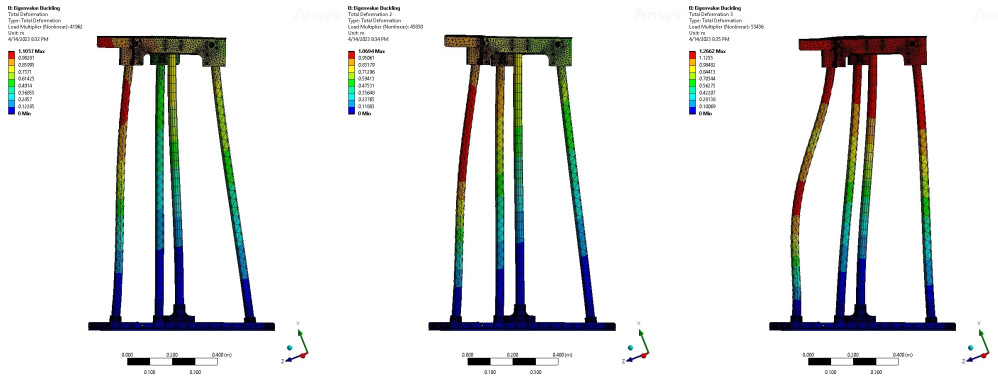
$m \approx 4$ kg, the mass of the payload deck including payload.

The above calculation makes the extremely conservative assumption that the boundary condition on the payload deck is free to translate. If that boundary condition were pinned, then $K \approx 0.8$, yielding $F_{crit} \approx 13194$ N per tube and $a_{crit} \approx 13194\ \mathrm{m\,s^{-2}}$ for a 4 kg mass. In this calculation, the mast tubing structures are presumed to be vertical, while three of them are actually at 6 ° angles; this would causes an expected derating of <5 %, and can be further analyzed in finite element models. By analyzing the shape of the buckled structure in a finite element model in the following section, these assumptions may be tested and further analyzed. Conservatively, based on the hand-calculations alone, the mast should be able to carry a 4 kg payload at accelerations up to 5000 $\mathrm{m\,s^{-2}}$ with a >1.6x safety factor.

Finite Element Model: Eigenvalue Buckling

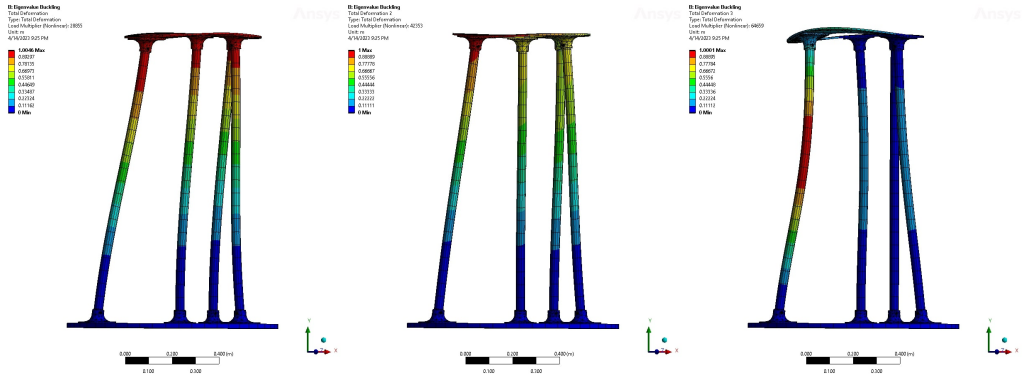
In addition to the hand calculation, a finite element model was constructed in Ansys Mechanical 2021 to preform an eigenvalue buckling analysis. Due to the large number of supports and stringers beneath the surface of the aft-body, the aft-body was approximated as a fully rigid structure. A point load was applied at the center of load point of the payload deck, near the GNSS mount corner of the structure. Buckling loads and mode shapes are depicted in Figure 3-6, with the lowest buckling mode at 41962 N. The buckling mode shapes exhibit a fixed boundary condition at the aft-body, and a boundary condition somewhere between fixed and free at the payload deck side. A buckling simulation was also performed on the PDR V1 design, with mode shapes much more closely resembling a free boundary condition, as depicted in Figure 3-7 and a significantly lower first buckling mode at 28855 N. Identification of the V1 payload deck as the weak link in the V1 system informed the design of the payload deck in the as-built model. In comparison with the hand-calculation performed above, the mode values are similar to those calculated with a $K \approx 0.88$,

suggesting a payload deck boundary condition slightly more favorable than a free condition.



(a) Buckling mode 1, 41962 N. (b) Buckling mode 2, 45830 N. (c) Buckling mode 3, 53436 N.

Figure 3-6: Buckling modes of as-built SGIP antenna mast when subjected to representative force distribution. Displacements are scaled up for illustrative purposes.



(a) Mode 1, 28855 N. (b) Mode 2, 42353 N. (c) Mode 3, 64659 N.

Figure 3-7: Buckling modes of V1 (PDR) SGIP antenna mast when subjected to representative force distribution. Displacements are scaled up for illustrative purposes.

3.2.2 Radial Loads

During field operations, initial helicopter pickups of the SGIP unit will likely be preformed with SGIP in a vertical configuration in a pre-made staging assembly.

However, in the event that SGIP needs to be set down, or needs to be picked up in a horizontal configuration, the SGIP antenna mast will bear significant load from the helicopter lanyard through the guide pole. These radial forces are may be as large as the weight of the penetrator, estimated at 1300 N. To understand the effects of radial loading on the mast system, an eigenvalue buckling simulation was performed in Ansys Mechanical 2021. In these simulations, the aft-body was set up as a rigid structure, with a load applied radially outwards at the top of the guide pole as pictured in Figure 3-8 (e). The results of these simulations in Figure 3-8 estimate a safety factor of >7 for helicopter pickup of SGIP in the horizontal configuration. Notably, compared to the axial loading detailed in Section 3.2.1, more of the deformation in the radial load case occurs in the payload deck region. In cases where SGIP may be buried horizontally under >1 m of snow or firn, digging to remove surface snow may be needed before hoisting to recover SGIP to prevent radially overloading the mast structure.

3.2.3 Aerodynamics

Given the year-long operations requirement for SGIP, it is essential that the structure can survive wind loads at all times of the year without tipping over or buckling. Thus, a hand-calculation of aerodynamic loads is performed.

Hand Calculation

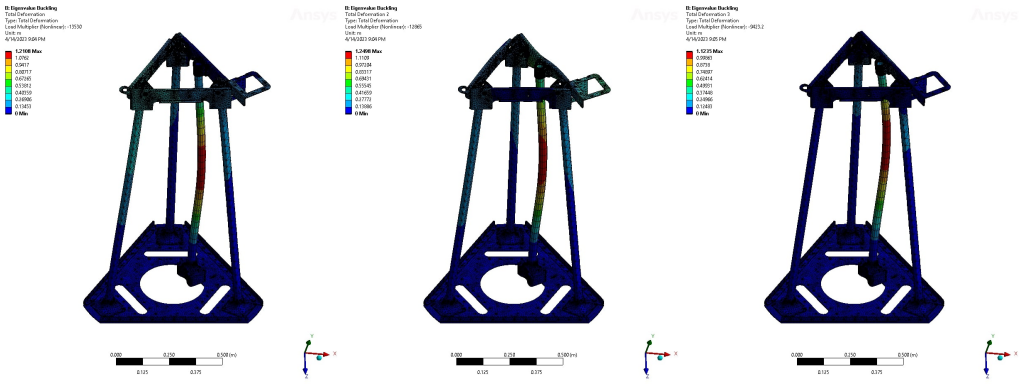
To calculate the density of air at Antarctic temperatures, Equation (3.7) is used, which assumes that the Antarctic air will be dry, and at sea level.

$$\rho = \frac{p}{R_{sp}T} \quad \approx 1.42 \quad \mathrm{kg\,m^{-3}} \tag{3.7}$$

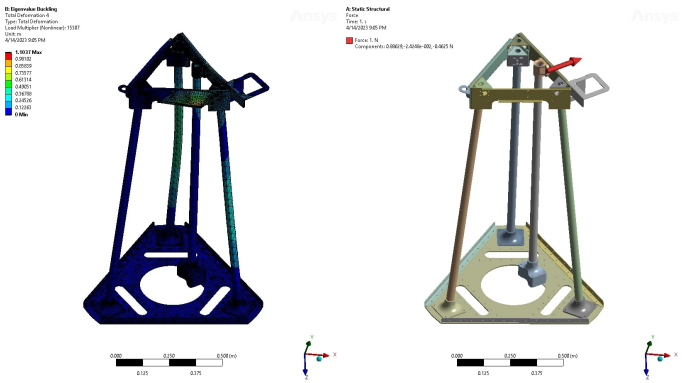
where

$T \approx 248.15$ K ≈ -25 °C is the temperature in the Antarctic environment.

$p \approx 101.33$ kPa is the static pressure of air.



(a) Mode 1, -13530 N. (b) Mode 2, -12865 N. (c) Mode 3, -9423 N.



(d) Mode 4, +15307 N. (e) Direction of applied force.

Figure 3-8: Buckling modes of SGIP antenna mast when subjected to representative force distribution. Note that negative mode force values occur with forcing in the opposite direction of the applied force shown in (e). Displacements are scaled up for illustrative purposes.

$R_{sp} \approx 287.1\ \mathrm{J\,kg^{-1}\,K^{-1}}$ is the specific gas constant.

With representative wind speeds on the Ross Ice Shelf, this corresponds to a dynamic pressure calculated in Equation (3.8).

$$q = \frac{1}{2}\rho v^2 \quad \approx 891.1 \quad \mathrm{kg\,m^{-2}} \tag{3.8}$$

where

$v \approx 35.4\ \mathrm{m\,s^{-1}}$ is the wind speed corresponding to the maximum wind gust speed on the Ross Ice Shelf [18].

To calculate the lateral aerodynamic forces on the tubing in the mast structure, equation Equation (3.9) is used.

$$F_{d-deck} = qc_{d-cylinder}A_{tube-combined} \quad \approx 182.98 \quad \text{N} \tag{3.9}$$

where

$c_{d-cylinder} \approx 1.20$ is the non-dimensional drag coefficient for a circular cylinder [35].

$A_{tube-combined} \approx 0.176$ m^2 is the combined effective area of all four supporting tubes structure.

To calculate lateral aerodynamic forces on the payload deck, equation Equation (3.10) is used.

$$F_{d-tubes} = qc_{d-plate}A_{deck} \quad \approx 90.98 \quad \text{N} \tag{3.10}$$

where

$c_{d-plate} \approx 1.28$ is the non-dimensional drag coefficient for a flat plate perpendicular to the direction of fluid flow [55] [10].

$A_{deck} \approx 0.079$ m^2 is the effective area of the payload deck, representing twice the area of a sheet metal side plate as a worst case scenario for an angled wind which hits both the front plate and back section of the payload deck.

To calculate lateral the aerodynamic forces on the tubing in the mast structure, equation Equation (3.11) is used.

$$\sum \tau_d = r_{tubes} \times F_{d-tubes} + r_{deck} \times F_{d-deck} \quad \approx 237.2 \quad \text{N m} \tag{3.11}$$

where

$r_{tubes} \approx 0.65$ m is the centroid height of the fiberglass tubes above the aft-body.

$r_{deck} \approx 1.3$ m is the centroid height of the payload deck above the aft-body.

The total pitch moment on the structure in the conditions detailed above is 267.85 N during a 35.4 $\mathrm{m\,s^{-1}}$ wind event. This corresponds to a worst-case scenario where the area of the payload deck is effectively doubled due to the tilt of the system; in a less conservative estimate with a realistic payload deck area for sideways airflow, an aerodynamic torque of 178.07 N m would be expected.

To prevent the aft-body and mast from tipping over, a set of spikes which sit at the edge of the aft-body to provide stabilization during radial loading is proposed in Chapter 4.

3.3 Manufacturing and Assembly

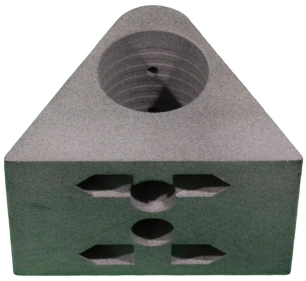
3.3.1 Fit checks and Assembly

In prototyping the SGIP static mast system, the goal was to identify the components most likely to need iteration and prototype those first in order to save cost and accelerate the critical development path. From initial design studies, the generic interface between the fiberglass tubing and nylon section joints was identified as most likely to need iteration. The initial fit test was slightly loose with 0.38 mm of clearance on all sides, so on subsequent versions the bore was made undersized by 0.050 mm and enlarged with a rotary tool sanding attachment. This yields a rough surface conducive to gluing and a slip fit which can be assembled without a mallet, but retains with considerable friction.

The second component to prototype was the payload deck, with a focus on ensuring that the sheet metal pieces fit together and had minimal flexure. Initial fit checks of the payload deck itself were successful. However, the Iridium mount and GNSS mount needed more slop in their hole patterns to adjust for the looser tolerances of the bending. This was accomplished by adding wider slots to the bottom holes in the GNSS and Iridium mount in the second round of manufacturing. The initial GNSS antenna mount was also submitted to the manufacturer with the wrong chirality; when inputting the bend directions the part can either come out as a "left"



(a) Bottom tube joint.



(b) Top tube joint.



(c) Guide pole bottom tube joint.



(d) Guide pole top tube joint.

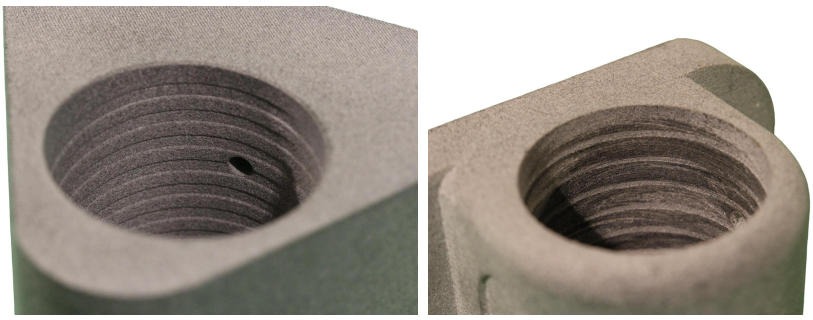
Figure 3-9: Set of nylon tube joints manufactured for the SGIP mast with standardized adhesive interface.

part or as a "right" part, and this was noted on the second round of manufacturing as well. It was also verified that the Iridium and GNSS antenna mounts fit the respective antennas.

After these smaller scale fit checks, the assembly of the mast system consisted of gathering the necessary hardware, bolting components together, and drilling the retention holes in the fiberglass. The stainless steel cable structures were assembled by measuring the necessary lengths, cutting the cables with a rotary tool, then using a drill and blow torch to create a finished end, as shown in Figure 3-12. The mast assembly was mounted onto a mock flare interface as shown in Figure 3-11 for easy transport.

3.3.2 Procurement of fiberglass tubing

While a key consideration of the SGIP static mast design was using easy-to-source parts, procuring the fiberglass tubing was unusually difficult due to both



(a) Before sanding. (b) After sanding.

Figure 3-10: Nylon tube joints before and after sanding. Sanding causes limited surface melting, but leaves a surface texture that is still rough and porous, thus appropriate for gluing.

limited supplier communication, manufacturing constraints, and supply-chain issues. Fiberglass tubing products like G10 are made on a mandrel, ensuring tight tolerances on the diameter. However, since many manufactures use 1.22 m mandrels to produce G10 tubing, and the ends are scrapped, most distributors don't sell the designed 1.22 m (48 in) length. Franklin Fibre sells the full-length pieces, but had very variable stock, and some companies had very limited stock of the 1.22 m length tubes. However, Franklin Fibre and other manufacturers distribute to McMaster Carr which sell G10 in 1.22 m lengths but have a looser tolerance than desired. By coordinating with McMaster Carr tube sections with "over" measurements and not "under" measurements were purchased.

3.4 Testing

To confirm that the mast subsystem will operate as intended in the Antarctic and other applicable field conditions, areas of risk that are difficult to model were identified and the following tests were devised and carried out.

3.4.1 Water Absorption Testing

During initial handling of the HP multijet fusion glass-bead-filled Nylon 12 parts, surface staining from hand oils and moisture such as in Figure 3-13 (a) prompted

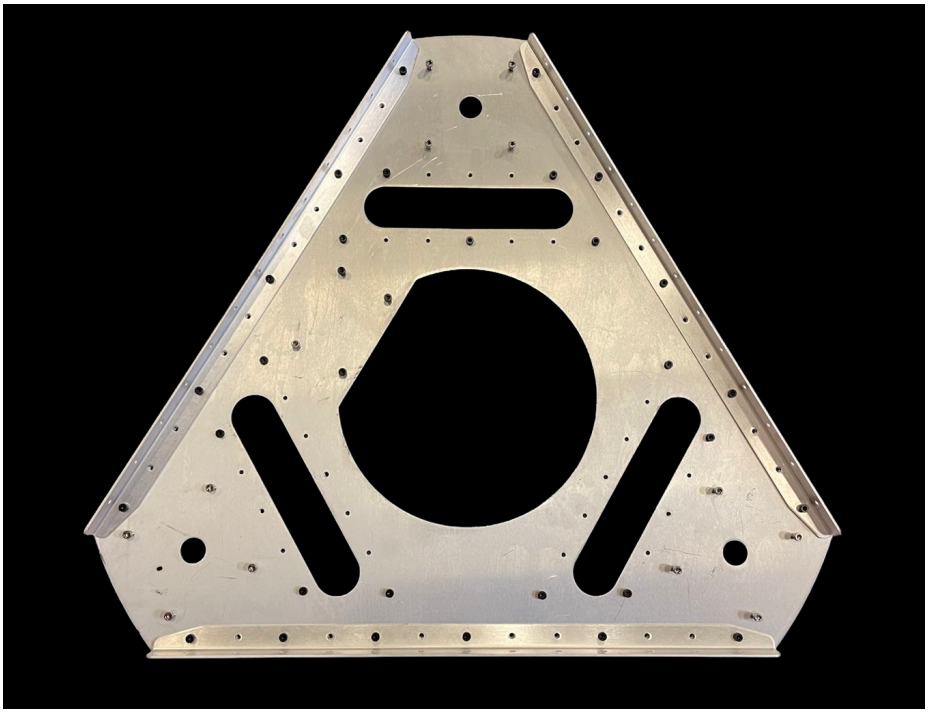
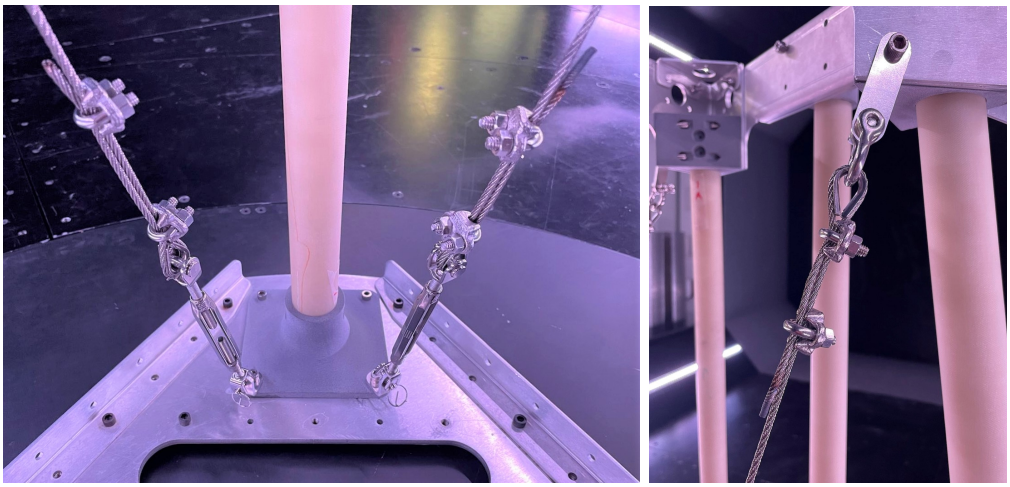


Figure 3-11: A mock flare interface constructed for fixturing and assembly.



(a) (b)

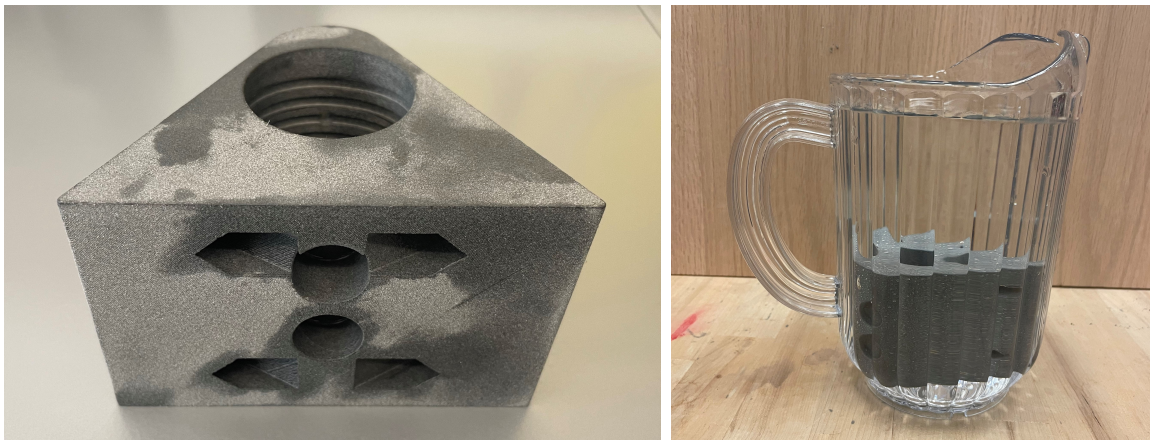
Figure 3-12: Cable structures installed on the SGIP antenna mast. (a) Bottom cable structures including anchor, thimble turnbuckle and saddle clamps. (b) Top cable structure including anchor, shackle, thimble and saddle clamps.

concerns that water could further permeate the part. Despite the parts being printed at 100% infill density, if water were to permeate the part then freeze, then there would be potential for splitting between the layers leading to structural failure. Sections of

Nylon 12 parts are expected to absorb up to 2% of water by mass when saturated in water based on prior manufacturer testing, however absorption in the entire part would be lower if the water doesn't completely permeate it [4]. To test this, the maximum amount of moisture absorption was quantified in a spare prototype corner joint component.

First, the prototype joint was weighed in its dry state at 239 g. After soaking the part in tap water for 60 minutes, as shown in Figure 3-13 (b), the surface of the part was dried off with a paper towel and weighed again at 240 g. During soaking, after bubbles left from interior features in the first 5 min, there were no other bubbles spotted during the duration of the test. There are several interior features which weren't accessible to manual surface drying, so the 1 g of water difference was likely too have been absorbed in the surface and accounted for by excess water stored in interior features. Over the next 20 min, the surface of the part returned to its dry appearance and texture. Even in the worst case scenario, this corresponds to a part volume increase of 1 cm^3. Thus, the changing appearance of the parts when moisture is applied is due to only the surface layer absorbing moisture, not moisture permeating through the bulk part. Based on the part mass increase measured above, and water increasing in volume by 9% when frozen, the part increases by a volume of 0.09 cm^3 in the worst case. This trial was repeated with 24 h of soaking time in the water; the part had the same starting and ending mass during the 24 h trial compared to the 60 minute trial.

To evaluate the impact of freezing and thawing the joint components, the joint was subjected to three cycles of soaking in water for 60 min, freezing in a standard household freezer, then thawing the part. After these cycles, the part had neither cracking nor any other visually apparent changes. The part was struck three times with a 4.5 kg sledgehammer dropped from a height of 30 cm and did not crack. Since the joint parts need to be strongest during the drop phase of operations, there will only be a small number of thermal cycles on the part during this critical phase. However, if field testing uncovers further concerns, then more rigorous thermal cycle testing may be conducted in the future. Furthermore, if absorption of water on the



(a) (b)

Figure 3-13: (a) Temporary surface staining from water on a Nylon 12 multijet fusion part; this staining evaporates on the order of 20 minutes. (b) Water absorption of nylon parts was tested by soaking parts.

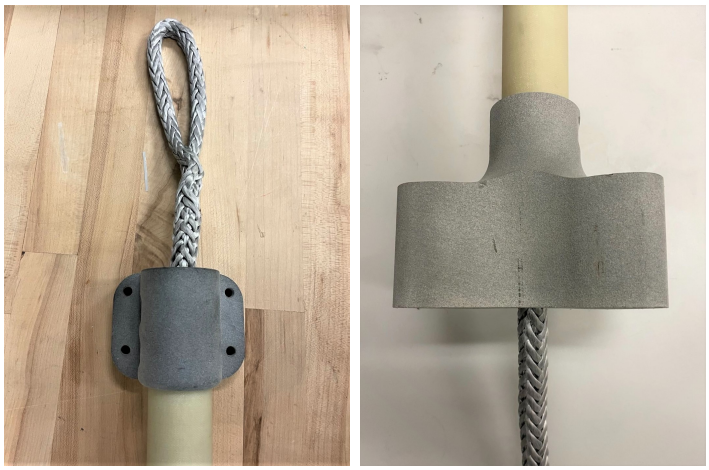
surface features becomes a concern, the parts may be coated in polyurethane, or another spray sealer.

3.4.2 Lanyard Retraction Testing

During the separation of the fore-body and aft-body sections of SGIP, the lanyard which ties the fore-body to the helicopter is rapidly drawn through the mast guide pole and the aft-body. Since this is a rapid event, spanning less that 0.1 s, it is essential that the lanyard passes cleanly through the guide pole without getting caught on the antenna structures or on any of the guide pole interior interfaces as shown in Figure 3-14. Thus, this lanyard retraction was tested by hand-pulling the lanyard through the guide pole assembly 10 times in many different orientations; no snags or other mishaps occurred.

3.4.3 Aerodynamic Testing

Wind tunnel testing was conducted to verify the aerodynamic loads calculated in Section 3.2.3.



(a) Top section. (b) Bottom section.

Figure 3-14: Lanyard passing through guide pole during test.

Wind Tunnel Test Fixture

To secure the mast to the wind tunnel, a test interface plate was constructed which bolts the mock flare plate to the wind tunnel force measurement stand. To preserve flow in the boundary layer as much as possible, machined 9.32 cm standoffs were used to elevate the fixture above the floor, with a gap of 0.29 cm. The fixturing standoffs and test interface plate are pictured in Figure 3-15. To verify that the mast structure would not contact the floor during wind tunnel tests, the top of the payload deck was pull-tested with a force gauge to 10 kg. The mast structure was tested with the cable structures fully installed, and the axes and coordinate system of the wind tunnel are pictured in Figure 3-16, positioned to accommodate the 60 ° yaw angular range of the wind tunnel. The test fixture did not accommodate pitch variation since the mounting structures would cause such a large amount of drag that the results would not be of acceptable accuracy; instead, a safety factor is added to results to account potential pitch angles. The full test configuration in the wind tunnel is pictured in Figure 3-17.

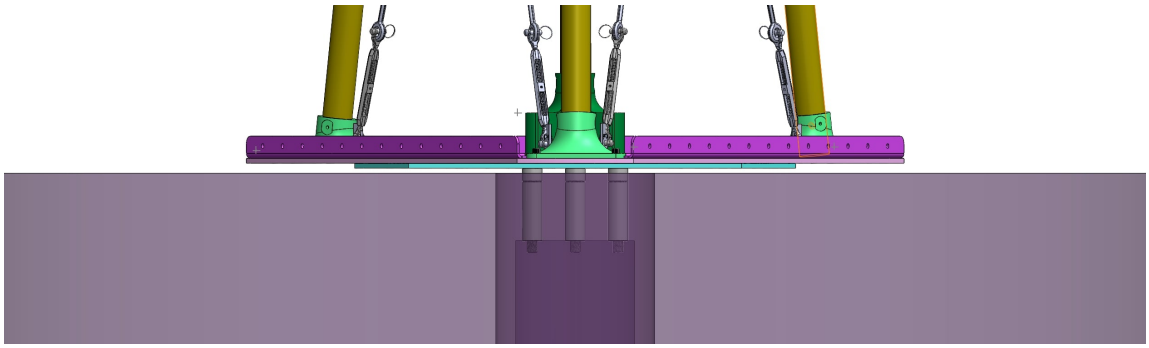


Figure 3-15: Fixturing for the SGIP mast to the wind tunnel force measurement stand, showing the machined standoffs.

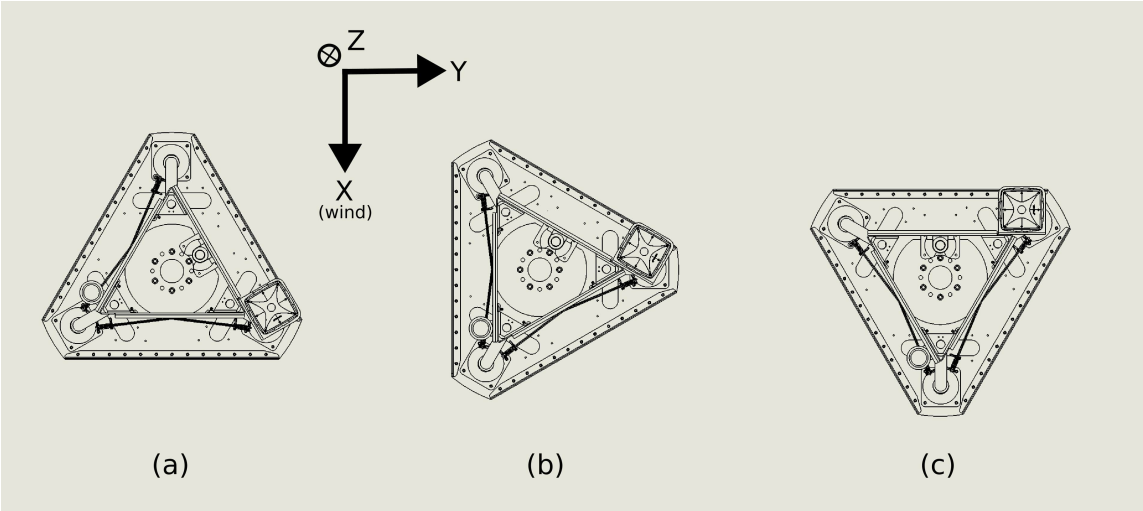


Figure 3-16: Arrangements of SGIP mast in the wind tunnel, showing coordinate systems, with the wind in the +X direction and the mast at angles (a) -30 deg. (b) 0 deg. (c) +30 deg. The mast can be adjusted within this angular range using the wind tunnel servo motors.

Wind Tunnel Test Results

In wind tunnel testing conducted on 02/21/2023 in the MIT Wright Brothers Wind Tunnel, a sweep of five different dynamic pressure values were tested across a range of yaw angles with the extremes shown in Figure 3-16. Due to radial symmetry of the mast structure this range approximates the performance of the mast of any yaw angle.

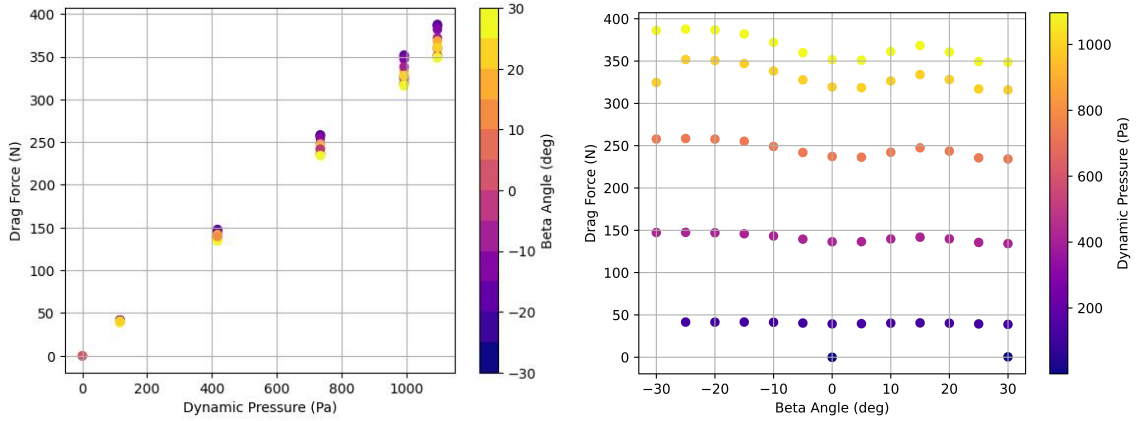
Testing began and ended with a wind-off tare which acquired 30 s of data which was subtracted from all other load cell readings. Five different dynamic pressure



Figure 3-17: SGIP antenna mast in MIT Wright Brothers Wind Tunnel for aerodynamics testing.

values were selected: 116.0, 417.3, 734.6, 993.3, and 1096.3 Pa, fully covering the current operational range of the wind tunnel; at Antarctic conditions calculated in Equation (3.8), these correspond to wind speeds of 12.8, 24.2, 32.2, 37.4, and 39.2 $\mathrm{m\,s^{-1}}$. During testing, the dynamic pressure was measured with a pitot tube and was noted. To calculate the corresponding wind speed, the temperature and barometric pressure were noted before each new wind speed. During the course of the testing, there was significant 6 °C heating due to the increased pressure. In each test, 30 s of data were acquired; in calculating steady state forces and moments these data were time-averaged.

The drag force of the mast system increases linearly with dynamic pressure, with low yaw angles corresponding to drag forces as much 40 N higher than high yaw angles as shown in Figure 3-18. Across the test, the mean $C_D A$ was calculated as



(a) (b)

Figure 3-18: Drag force data from wind tunnel test where (a) frag force increases linearly with dynamic pressure. (b) Drag force varies with azimuth angle within a 40 N range.

0.0337 m^2 with $\sigma = 0.0125$ m^2; as this is a bluff body, this is close to the frontal area of the system.

Unexpectedly, there was significant upwards normal force detected at high dynamic pressures as shown in Figure 3-19; since there are no large flat surfaces on the mast payload deck, this lift was likely due to the mock flare fixture plate shown in Figure 3-15. In the deployed SGIP configuration, the aft-body will not have a large flat exposed underside and should not cause lift. side force and yaw moments were under 20 N m and 10 N m respectively for the dynamic pressures tested and are not significant factors in system design.

In order to calculate the pitch moments experienced by the aft-body section of SGIP, a conversion must be made between the wind tunnel coordinate system in which the moments are measured and the center of mass (COM) of the aft-body, around which the structure would be tilted by the wind; the relevant forces and coordinate systems for this conversion are shown in Figure 3-20 with the calculations performed in Equation (3.12) and Equation (3.13). The coordinate conversion assumes that there are no significant drag moments above the wind tunnel coordinate system, which is appropriate because the wind tunnel frame is only 0.127 m from the top of the mast. Based on these calculations, the center of pressure is calculated in Equation (3.12)

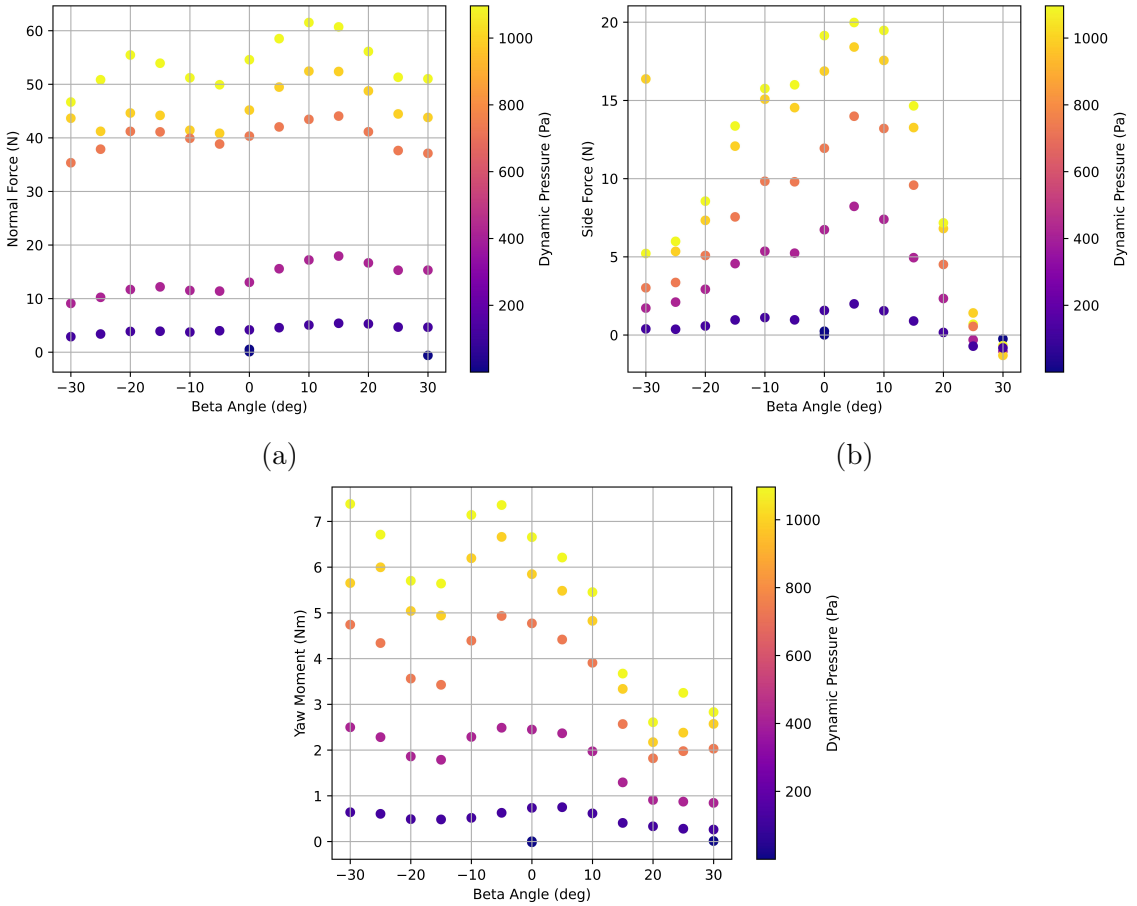


Figure 3-19: Data from wind tunnel testing of SGIP antenna mast showing (a) normal force. (b) side force. (c) yaw moment.

as 0.76 ± 0.20 m above the top of the aft-body, by taking the mean of the center of pressure values throughout the wind tunnel dataset, excluding the wind-off-tare trials. The moments around the aft-body flare COM are calculated using in Equation (3.13). At the maximum dynamic pressure on the Ross Ice Shelf calculated as 891.1 $\mathrm{kg\,m^{-2}}$, the aft-body center of mass experienced a pitch moment of 260 ± 60 N m. Notably, these observed pitch moments are most similar to the hand calculation values in Section 3.2.3 when the payload deck area is doubled. By using this same procedure, the moment around any other point on the aft-body may be calculated.

$$h_{mastCP} = h_{pivot} - \frac{T_{pivot}}{F_{drag}} \quad \approx 0.76 \pm 0.20 \quad \text{m} \tag{3.12}$$

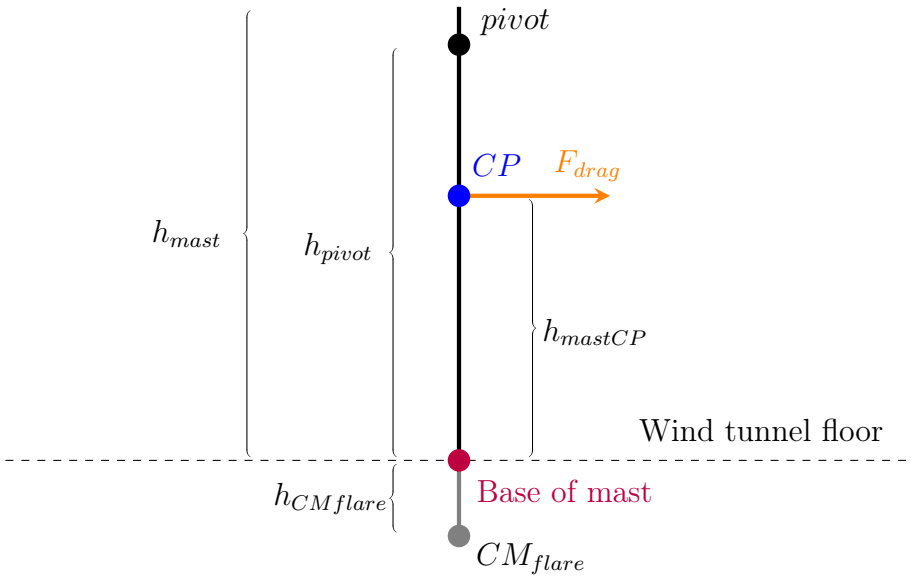


Figure 3-20: Free body diagram showing the mast with the relevant coordinate systems for calculating wind moments on the SGIP antenna mast and aft-body flare, side view.

where

$h_{pivot} \approx 1.1827$ m is the height of the coordinate system origin used by the wind tunnel data system.

T_{pivot} is the torque experienced by the mast, measured in the wind tunnel coordinate system around the pivot shown in Figure 3-20.

F_{drag} is the measured drag force in the wind tunnel, shown in Figure 3-18.

$$T_{CMflare} = F_{wind} \times (h_{mastCP} + h_{CMflare}) \quad \approx 260 \pm 60 \quad \text{N m} \tag{3.13}$$

where

$h_{CMflare} \approx 0.1$ m is the distance between the top and the center of mass of the aft-body flare.

3.4.4 Radio Frequency Interference Testing

Quantifying uncertainty in GNSS measurements is critical for geodesy applications; since antenna performance is affected by all nearby structures and radio signals, the mast structure was evaluated for radio frequency interference. The GNSS antenna was tested on 12/07/2022 and 12/08/2022, then again on 12/10/2022 and 12/11/2022 with a added microwave absorbant material below the GNSS antenna, with data shown in Figure 3-21. With an added microwave absorber, the tail of the post-fit residuals is significantly flattened, and the RMS value is decreased. However, performance without the absorber remains acceptable; the 5 cm thick profile of the absorber and its foam-like elasticity would significantly increase mechanical integration complexity due to the structural shock involved. Therefore, the prototype flight model will be flown without a microwave absorber.

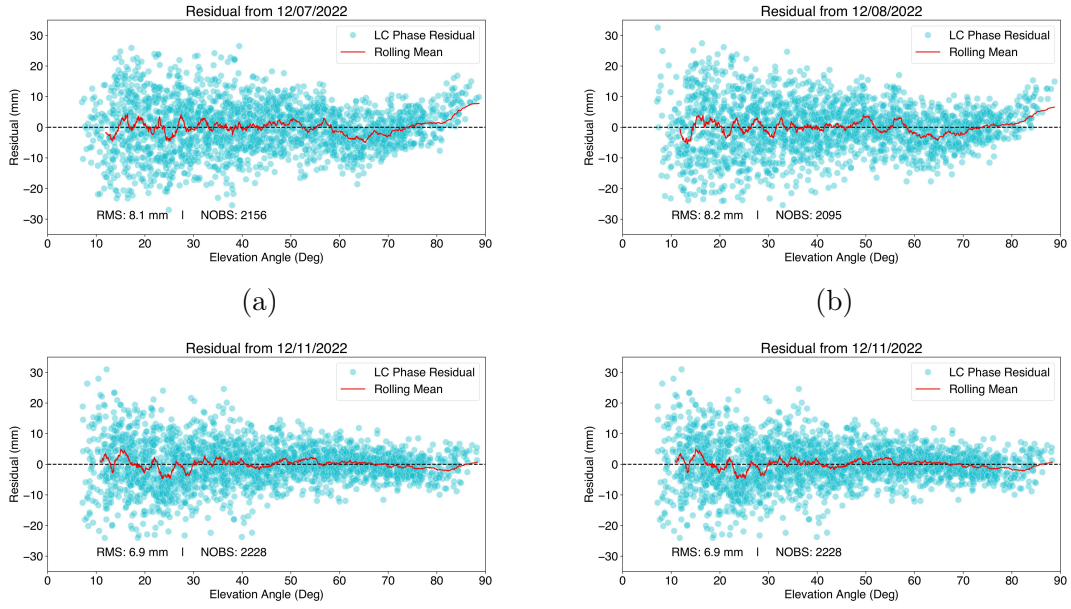


Figure 3-21: Data from GNSS antenna testing on (a) 12/07/2022 and (b) 12/08/2022 without a microwave absober. (c) 12/10/2022 and (d) 12/11/2022 with a added microwave absorbent material below the GNSS antenna.

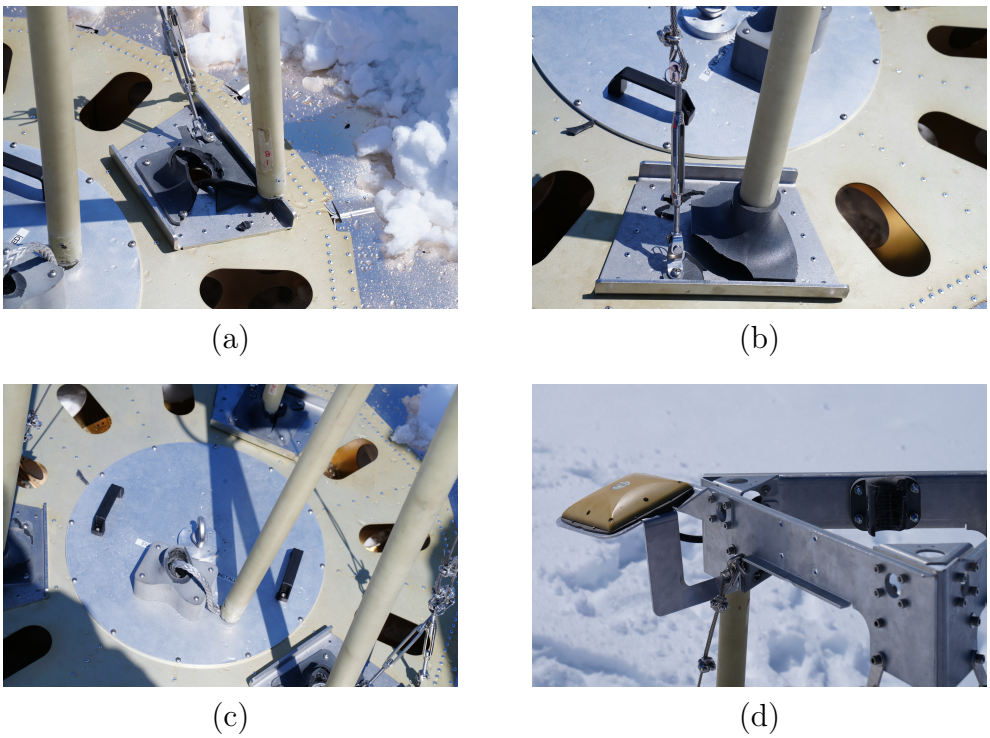
3.4.5 Juneau Full-Scale Testing

While many component tests and areas of areas of analysis were used to rate the SGIP antenna mast for operation during the SGIP drop phase and year-long operations in the Antarctic environment, full-scale testing provides invaluable feedback for how the mast interacts with the rest of the SGIP system during deployment. In a full-scale SGIP drop test conducted in Juneau, Alaska and described in Section 2.7, the SGIP system hit the surface snow at around 15 ° and sustained a larger than expected radial acceleration of 500 $\mathrm{m\,s^{-2}}$. During this impact event, the bottom 3D printed MJF Nylon 12 parts experienced a brittle fracture event near the tubing interface and also near the bolt holes. The mast remained held on by the cable structures. The payload deck MJF joints, fiberglass tubing, payload deck, Iridium antenna mount and Iridium antenna were undamaged. The GNSS antenna mount experienced moderate deformation and around 20 ° of tilt. This damage is shown in Figure 3-22.

As shown in Figure 2-16, the penetrator was spinning significantly and angled during impact causing substantially higher radial and shear loads than expected. Nevertheless, previous simulation and testing didn't explore brittle fracture, and this is a valuable learning before future deployments.

3.5 Proposed Design Changes After Field Testing

To strengthen the SGIP mast system for high radial loads such those in the first Alaska drop test, the material of the bottom-side mast joint components should be replaced. During a radial shock loading such as that in Figure 2-16, the mass of the payload deck loads the bottom joints with the mast as a lever. To prevent fracture incidents in future skewed impacts, it is proposed that the three bottom tubing joint structures shown in Figure 3-9 (a) be replaced by an version CNC machined out of 6061 aluminum. Since the guide pole is not needed after impact, the guide pole joints do not need to be replaced. By reducing the footprint of the part to 10.2 cm from the original 12.7 cm the aluminum version would have a mass of 0.41 kg compared to 0.19 kg per joint. If at least six units were purchased, the price would be equal to



(a) (b) (c) (d)

Figure 3-22: SGIP antenna mast after first prototype deployment on the Juneau Ice Field with an angled impact of around 15 °with an acceleration profile on the nose shown in Figure 2-16. Shear loads were much higher expected and caused (a, b, c) fracture on the MJF bottom components both at the site of the fiberglass tubes and the fastener holes. (d) bending of the antenna support mount. The structure was kept held down by the cable structures. The top MJF parts, fiberglass tubes and the payload deck were all intact.

the nylon version, and if more were purchased it would be cheaper.

3.6 Conclusions

An static antenna mast for kinetic penetrators was designed, developed, analyzed, built and tested. This antenna mast is suitable for SGIP and similar designs may be modified for other applications with similarly high axial loads. For future polar or planetary applications, the mast may hold other payloads such as vertically oriented solar panels, anemometers, or communications devices.

Chapter 4

Design and Construction of Snow Spikes

4.1 Introduction and Snow Spike Requirements

To continue operations on the Antarctic surface for a year requires the SGIP antenna system to have minimal movement and to stay upright. Additionally, accurate GNSS requirements of the ice shelf require a stationary antenna structure with minimal movement or wobble. Aerodynamic testing, described in Section 3.4.3, showed that the center of pressure of the SGIP antenna mast will be subjected wind forces up to 300 N. Taking into account the compressive properties of the surface firn, the flare is most likely to pivot around the inner "solid" area with a pivot point 0.5 ± 0.1 m from the center of the flare depending on the firn properties. While the as-built prototype pictured in Figure 1-3 has an aft-body mass of 68 kg, the future versions must have a lower center of mass, necessitating an aft-body mass closer to the original design mass of 25 kg. This section performs calculations using a 25 kg example aft-body, which is generalized in Table 4.5.

A free body diagram showing the location of this pivot relative to the wind force is depicted in Figure 4-1. Using this free body diagram, the torque caused by the wind is calculated as 230 ± 60 N m, notably larger than the 123 ± 26 N m of righting moment provided by a 25 kg aft-body flare.

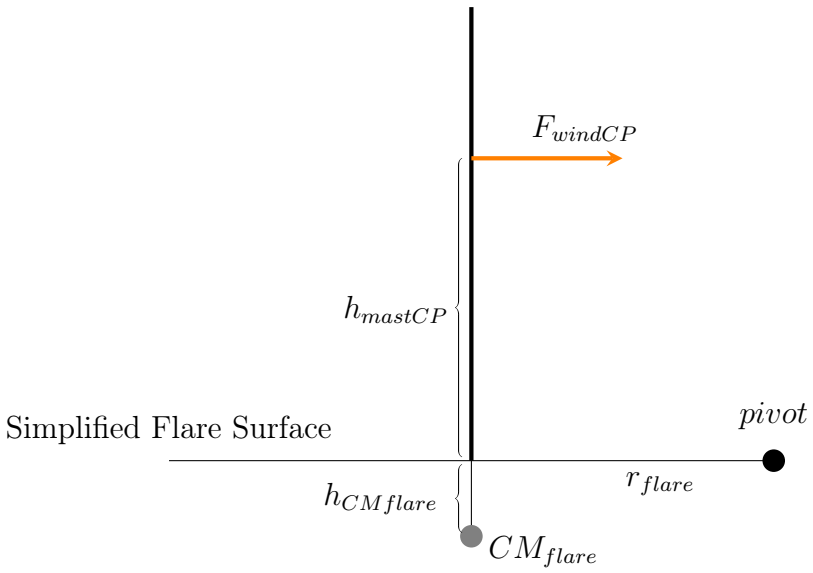


Figure 4-1: Free body diagram depicting wind force on SGIP mast, with torques defined on around the pivot.

$$T_{wind} = F_{wind}\left|\sqrt{r_{flare}^2 + h_{mastCP}^2}\right| \cos\left[\tan^{-1}\left(\frac{r_{flare}}{h_{mastCP}}\right)\right] \quad \approx 230 \pm 60 \quad \text{N m} \quad (4.1)$$

where

$F_{wind} \approx 300$ N, is the maximum wind force at the mast center of pressure, as shown in Section 3.4.3.

$r_{flare} \approx 0.5 \pm 0.1$ m, is the distance to the pivot point where the aft-body flare would tip over, here approximated as the end of the solid flare area.

$h_{mastCP} \approx 0.76 \pm 0.20$ m, is the center of pressure of the SGIP mast, calculated in Equation (3.12), averaged across wind tunnel testing data.

$$T_{flare} = m_{flare}g\left|\sqrt{h_{CMflare}^2 + r_{flare}^2}\right| \sin\left[\tan^{-1}\left(\frac{r_{flare}}{h_{CMflare}}\right)\right] \quad \approx 123 \pm 26 \quad \text{N m} \quad (4.2)$$

where

$m_{flare} \approx 25 \pm 2$ kg, is the mass of the aft-body flare.

$h_{CMflare} \approx 0.1 \pm 0.05$ m, is the distance from the top of the aft-body to its center of mass.

Since the mass of the flare itself is not enough to prevent the mast from being blown over, a set of snow spikes is proposed, designed, built and tested. The goal of these snow spikes is to provide a minimally invasive way of adding additional righting moment to the aft-body flare and mast system. Requirements for snow spike structures are detailed in Table 4.1.

Examples of exterior stabilization spikes on an air-dropped penetrator are not available in existing penetrator design literature [36]. In ADIOS, the main tubing section of the sensor acted as a spike; the flare core in SGIP acts similarly but is much smaller, and in any cases insufficient [28]. Many space penetrators incorporated intentional spin stabilzation during the drop and involve harder impact materials, prohibiting spike use. Furthermore, the lack of snow accumulation in Martian environments means that a low antenna may be used, reducing the moments caused by wind. Thus, stability enhancement using snow spikes is a new feature proposed in the SGIP design.

4.2 Design of Snow Spikes

From the requirements described in Section 4.1, three snow spike options were designed and selected for prototyping. These designs all have a compatible interface to the aft-body with bolts in a pattern designed to reinforce the four major stringer junctions in the aft-body.

The first option, in Figure 4-2 (a) features a tubular design, with a spike on the end similar to an ice axe handle used in the "piolet canne" technique for plunging. The tubular portion is affixed to the interface plate using a set of aluminum blind rivets. A threaded insert allows for different tip geometries to be used or for the spike to be removed entirely. The tip may be replaced with a with a conical shape, such as

Table 4.1: Requirements for SGIP snow spikes.

Requirement	Description
SGIP-SS-1: Load bearing	In conjunction with the aft-body structures, snow spikes must bear 300 N force on the mast center of pressure when planted in 350 $\mathrm{kg\,m^{-3}}$ firn.
SGIP-SS-2: Low insertion force	Snow spikes must be inserted into surface snow of 500 $\mathrm{kg\,m^{-3}}$ with <200 N each.
SGIP-SS-3: Replaceable and removable	Snow spikes must be removable from the aft-body and replaceable in case of damage or different snow conditions. A configuration must exist where the penetrator may be dropped with no spikes and still be fully structurally capable.
SGIP-SS-4: Rapid assembly	Snow spikes must be assemblable <30 minutes each, and must be swappable on the aft-body in <10 minutes each by a team of two people.
SGIP-SS-5: Mass	Snow spikes must be under 2 kg each.
SGIP-SS-6: Aerodynamics	SGIP must stabilize <3 s longer with spikes than without spikes during helicopter drop.

in Figure 4-2 (b), to promote backfill and to increase the amount of force required to pull the spike out. Another design, in Figure 4-2 (c) involves a single bent aluminum spike which is modeled after snow modern mountaineering snow picket anchors. This design is optimized for low insertion force due to the low cross-sectional area, and is made shorter than the designs in (a) and (b) due to its higher surface area.

4.3 Testing of Snow Spikes

Due to the high variability of surface firn and the difficulties in modeling firn structural response at low deflections, snow spike performance was quantified in testing. Snow spike tests were performed on 3/8/2023 and 3/9/2023 in Big Sky, Montana. These tests take force measurements during individual snow spike insertion, shear and removal in two different snow density profiles which are representative of operating surface firn conditions.

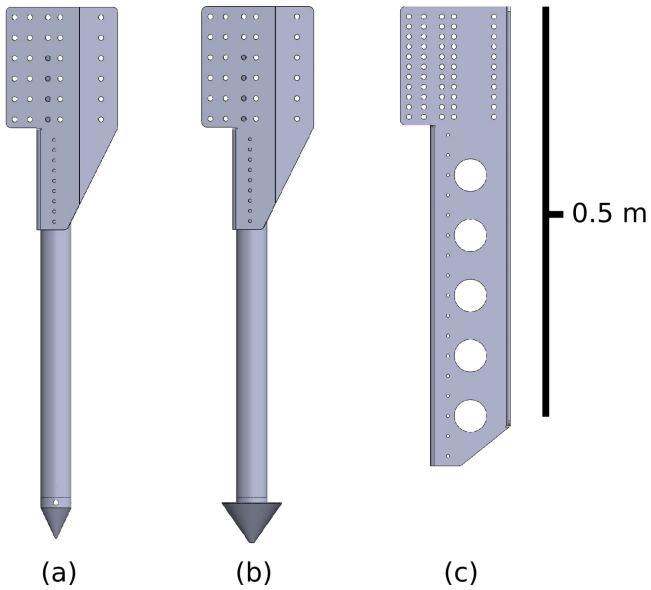


Figure 4-2: (a) Tubular snow spike design with a straight tip. (b) Tubular snow spike design with a large conical tip. (c) Bent sheet metal snow spike design.

4.3.1 Snow Density Measurement

Snow density measurement is generally conducted by taking a sample in a specialized container, then weighting the sample. Containers have been developed in tube, rectangular and triangle shaped packages, with triangle samplers being used to sample small volumes of snow [29]. For field testing of SGIP subsystems it was essential to be able to work in tight sampling spaces; thus, a custom-made 31.2 cm^3 triangle sampling scoop, pictured in Figure 4-3, was constructed out of sheet brass rather than using a standard pre-made 1000 cm^3 model. This scoop was made by folding a sheet of brass, soldering the edges to be water-tight, then coating the scoop in enamel to prevent corrosion and lead exposure. By filling the scoop with water and weighing the water, the scoop was determined to have a volume of 31.2 ± 0.05 cm^3.

To measure the density of snow pack, the scoop is plunged into the ground, then a plastic scraper is used to remove excess snow from on top of the scoop, and the sample is weighed using a scale, as depicted in Figure 4-4. Care must be taken to avoid compressing excess snow into the scoop during the scraping process. If there is excess snow that sticks to the exterior of the scoop surfaces, it is often necessary

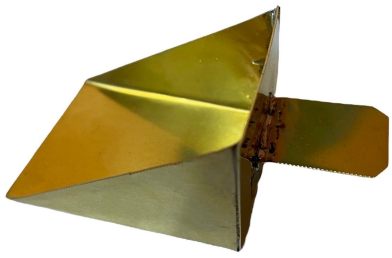


Figure 4-3: Custom-made snow scoop for measuring snow density.

to scrap the other surfaces of the scoop. When in tight spaces, such as sampling the inside of a hole made by a penetrator, the hole is bisected by a shovel to make a pit for easy access as shown in Figure 4-4 (a).



Figure 4-4: Illustration of the density measurement during field testing. (a) A sample is taken from the snow pack at the desired depth. (b) Alternatively a sample may be taken from the surface. (c) A plastic scraper is used to remove excess snow from the measurement scoop. (d) The sample is weighed using a scale.

4.3.2 Experimental Procedure for Snow Spike Test

The goal of the snow spike test is to test how difficult it is to place different snow spike designs into the snowpack, and whether they can take a sufficient degree of loading to be used to stabilize the SGIP mast under wind loading. The following procedure was followed during field testing, and is depicted in Figure 4-5.

1. Use the density measurement kit to measure the density of the snow pack in

the test site of choice.

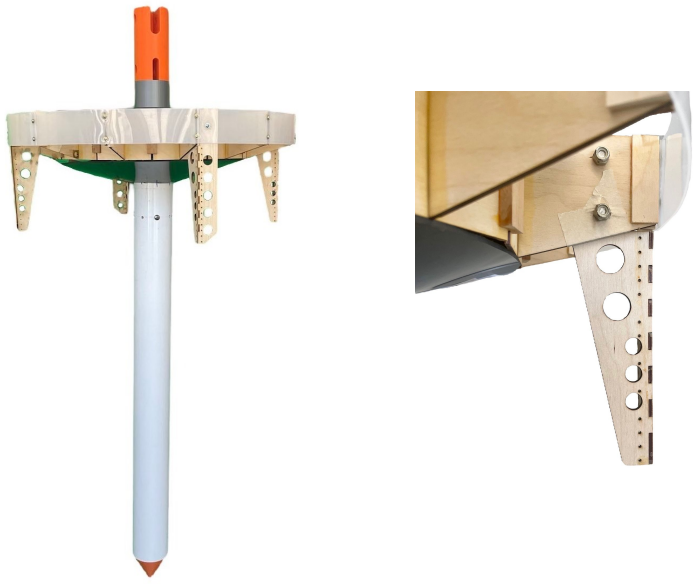
2. Attach extender bar to top of the snow spike under test.
3. Set up video camera and tripod aimed at snow spike and extender bar. Place ruler or other scaling device next to snow spike to measure deflections.
4. Plant the snow spike under test 0.2 m into the snow, and record the maximum insertion force using the force guage.
5. Using the hook attachment for the force guage pull on sideways on the snow spike extender bar, with the force gauge pointing towards the video camera. If needed to maintain space in the test environment, fasten the force gauge to the extender bar using paracord. In addition to the video camera, record the maximum force reading in data table.
6. Test the force that it takes to pull the snow spike out. If the previous step overly disturbed the spike, then replant the spike before this test.
7. Repeat steps 1-6 with the other snow spike designs. Do multiple trials if time allows.
8. Repeat steps 1-7 with a different snow density.



Figure 4-5: Testing snow spikes with a digital force gauge. (a) Insertion testing with the force gauge used to drive the spike into the snow. (b) Sideways pull testing with a 0.91 m lever arm. (c) Vertical pull testing, lifting the spike out of the snow.

4.3.3 Aerodynamics of Snow Spikes with SGIP System

While snow spikes can be used to help increase the tipping moment of the SGIP mast system, it is critical that the spikes do not interfere with the SGIP aerodynamic stability during the drop phase. To evaluate the effect on snow spikes on the system aerodynamics, a wind tunnel test was conducted in the MIT Wright Brothers Wind Tunnel on 5/12/2023 using a scale-model SGIP mockup shown in Figure 4-6. The scale-model was tested at dynamic pressures of 130, 268, 530 Pa, corresponding to approximate wind speeds of 15, 22 and 31 $\mathrm{m\,s^{-1}}$. At each of these windspeeds yaw angles $0 — 30\,^{\circ}$ were tested with and without snow spikes. These tests were calibrated using a zero-wind tare which was taken at every angle values in the range. The testing design, process and analysis is described in detail by Makikalli [37], and mirrors the analysis done in Section 3.4.3.



(a) (b)

Figure 4-6: Scale model (0.41x) of SGIP used for testing aerodynamic stability in the wind tunnel. (a) Full assembly. (b) Scaled spike model.

Wind tunnel test data were taken for each wind speed, yaw angle and spike configuration for 20 s, and were averaged over that time period to reduce the effect of high frequency noise. A complete suite of tests were taken with and without snow

spikes to compare the effect of spikes on SGIP stability forces and moments. Like a generic bluff body, the drag forces on SGIP vary linearly with the dynamic pressure; the drag force also increases with yaw angle, which is partially due to the shape of the flare structure and likely partially due to the mounting faring structure in the wind tunnel. Roll moments, which can contribute to the spinning of the penetrator are plotted in Figure 4-7 (c). For small yaw angles these moments are similar in magnitude and opposite in direction with and without snow spikes. However, for the highest yaw angle of 25 °, the roll moment reaches up to >5 N m. With the full-size penetrator roll moment of inertia of 12.46 $\mathrm{kg\,m^2}$, this may be enough to cause a spinning event such as that detailed in Section 2.7 in some wind and drop conditions. Plots of these data are presented in Figure 4-7.

4.3.4 Snow Spike Field Test Results

From the field testing of snow spikes a set of data are presented in Table 4.2, Table 4.3 and Table 4.4. All spikes were tested in both a firm and soft snowpack to compare performance; data were noted by carefully reviewing video of the force gauge, and corresponding uncertainties noted in table headers are due to difficulty in identifying the time of maximum force. To capture the variation between measurements, the mean and standard deviation are noted for each category of test. In the insertion tests, all spikes had a performance which was approximately proportionate to frontal area. The large conical spike was too difficult to insert into firm snow using body weight and thus was only characterized in softer snow across all tests. In the shear tests, the "sheet metal" spike slightly outperformed the "small spike" and "large spike" designs, but the results are not statistically significant. The ice axe was not tested under shear due to difficulties in affixing the lever arm. In removal testing, the "sheet metal" design also performed better than the "small spike", with the "large spike" performing the best due to exhibing some backfill, as seen in Figure 4-8. However, this backfill was much less dramatic than expected, and had only a minor difference on results. Due to its high performance in insertion, shear and removal testing as well as ease of manufacturing, the "sheet metal" design was selected as the

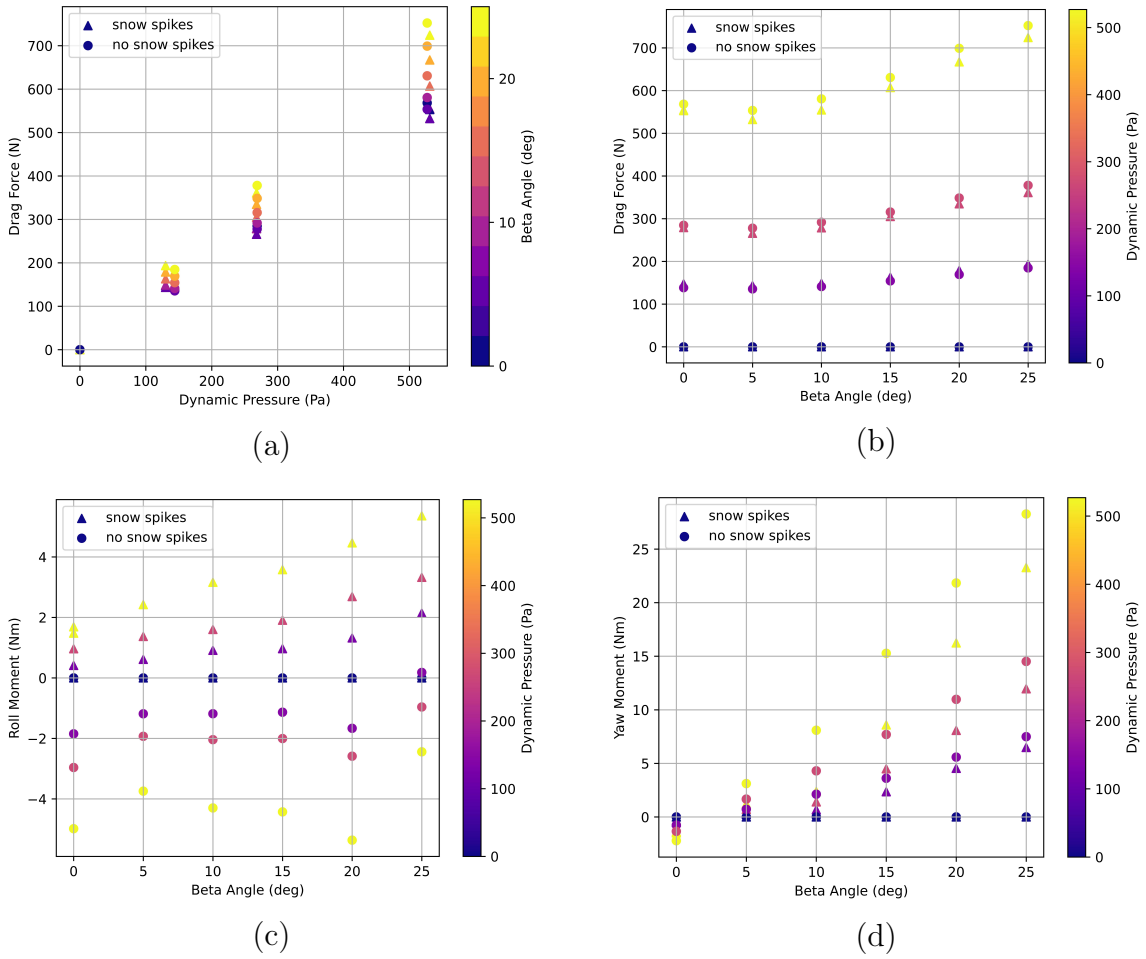


Figure 4-7: Wind tunnel data taken on 5/12/2023 of a scale-model SGIP prototype with and without snow spikes. Data are scaled to the full-scale prototype. (a) Drag force varies linearly with dynamic pressure. (b) Higher yaw (beta) angles lead to higher drag force. (c) Roll moments with and without snow spikes trend in the opposite direction, but are both very low in magnitude. (d) Yaw moments increase with yaw angle.

best candidate.

By contextualizing the lever arm onto which the shear tests were performed with the rest of the aft-body flare assembly, the shear forces and pull forces are mapped onto the aft-body in Figure 4-9. The spikes are numbered from 1 to 4, and are used to calculate the corresponding torques contributed by each spike in Equation (4.3a). For operations on the Ross Ice Shelf and field testing on the Juneau Ice Field, data from the denser $335 \pm 40\ \mathrm{kg\,m^{-3}}$ (N=6) snowpack were used to quantify performance. The

Table 4.2: Insertion force testing of snow spikes.

Test ♯	Snowpack	Spike model	Frontal area (cm^2)	Insertion force (N) ± 10 N	Mean (N)
1	0 - 0.15 m: $335 \pm 40\ kg\,m^{-3}$ (N=6) 0.15 - 1.0 m: $413 \pm 26\ kg\,m^{-3}$ (N=4)	small spike	11.4	50	140 ± 64
2				150	
3				160	
4				200	
5		ice axe	5.6	60	70 ± 14
6				80	
7		sheet metal	8.3	130	140 ± 14
8				150	
9		big spike	30.8	>250	NA
10	0 - 0.15 m: $170 \pm 21\ kg\,m^{-3}$ (N=4) 0.15 - 1.0 m: $283 \pm 9\ kg\,m^{-3}$ (N=4)	small spike	11.4	10	10 ± 0
11				10	
12				10	
13		sheet metal	8.3	5	8 ± 3
14				10	
15				10	
16		ice axe	5.6	10	12 ± 3
17				10	
18				15	
19		big spike	30.8	25	32 ± 8
20				30	
21				40	



Figure 4-8: Test of snow spike design with large conical tip, shown in Figure 4-2 (b), where only minimal backfill was observed.

Table 4.3: Shear force testing of snow spikes.

Test ♯	Snowpack	Spike model	Insertion depth (m)	Shear force (N) ± 10 N	Mean (N)
1		small spike	0.32	15	
2			0.37	25	30 ± 18
3			0.32	50	
4	0 - 0.15 m:		0.47	100	100 ± 0
5	335 ± 40 kg m^{-3} (N=6)	sheet metal	0.10	10	10 ± 0
6	0.15 - 1.0 m:		0.26	25	
7	413 ± 26 kg m^{-3} (N=4)		0.24	25	
8			0.24	25	34 ± 17
9			0.24	30	
10			0.29	65	
11		small spike	0.5	5	8 ± 4
12			0.51	10	
13	0 - 0.15 m:	sheet metal	0.43	10	
14	170 ± 21 kg m^{-3} (N=4)		0.43	10	10 ± 0
15	0.15 - 1.0 m:		0.43	10	
16	283 ± 9 kg m^{-3} (N=4)	large spike	0.51	5	
17			0.51	10	8 ± 3
18			0.51	10	

uncertainty from variance between different snow spike tests, SGIP design parameters, and wind tunnel data were propagated throughout all performance calculations. In addition to the snow spikes, the torques provided by the aft-body core structure are also included in Equation (4.3a) (g) and (h).

After calculating a total "restoring" torque from the flare mass, snow spikes and aft-body core in Equation (4.4), a design margin is calculated in Equation (4.5) by comparing the wind torque with the previously calculated "restoring" torque; for a 25 kg aft-body with sheet metal spikes, this margin is 2.3 ± 1.1. A complete list of performance margins calculated using the previously described method is listed in Table 4.5. Despite the large uncertainties in snow spike performance during field testing both the small spike design and the sheet metal spike design can be expected to prevent the SGIP aft-body from tipping across the full range of Ross Ice Shelf wind conditions. Furthermore, it is noted that with the uncertainties, torques provided by the aft-body mass and core structure provide insufficient stabilization alone for

Table 4.4: Removal testing of snow spikes.

Test Number	Snowpack	Spike model	Pull force (N), ± 5 N	Mean (N)
1	0 - 0.15 m: 335 ± 40 kg m^{-3} (N=6) 0.15 - 1.0 m: 413 ± 26 kg m^{-3} (N=4)	small spike	10	17 ± 6
2			20	
3			20	
4		ice axe	20	43 ± 25
5			40	
6			70	
7		sheet metal	70	60 ± 46
8			100	
9			10	
10	0 - 0.15 m: 170 ± 21 kg m^{-3} (N=4) 0.15 - 1.0 m: 283 ± 9 kg m^{-3} (N=4)	small spike	10	13 ± 3
11			15	
12			15	
13		ice axe	5	5 ± 0
14			5	
15			5	
16		sheet metal	10	17 ± 12
17			10	
18			30	
19		large spike	20	25 ± 5
20			25	
21			30	

aft-body mass <55 kg; thus, snow spikes are a critical part of the SGIP aft-body system. When viewed in context of the entire SGIP system, inclusion of snow spikes allows for the rest of the aft-body system to have less mass, thus facillitating a lower center of gravity and more stable drop.

$$T_{shear1} = F_{shear} \left| \sqrt{h_{spike}^2 + (2r_{flare})^2} \right| \cos\left[\tan^{-1}\left(\frac{h_{spike}}{2r_{flare}} \right) \right] \quad \approx 34 \pm 18 \quad \text{N m} \quad (4.3a)$$

where

$h_{spike} \approx 0.914 \pm 0.01$ m is the length of the lever arm attached to each snow spike during field testing.

$F_{shear} \approx 34 \pm 17$ N is the tested mean and standard deviation shear force during

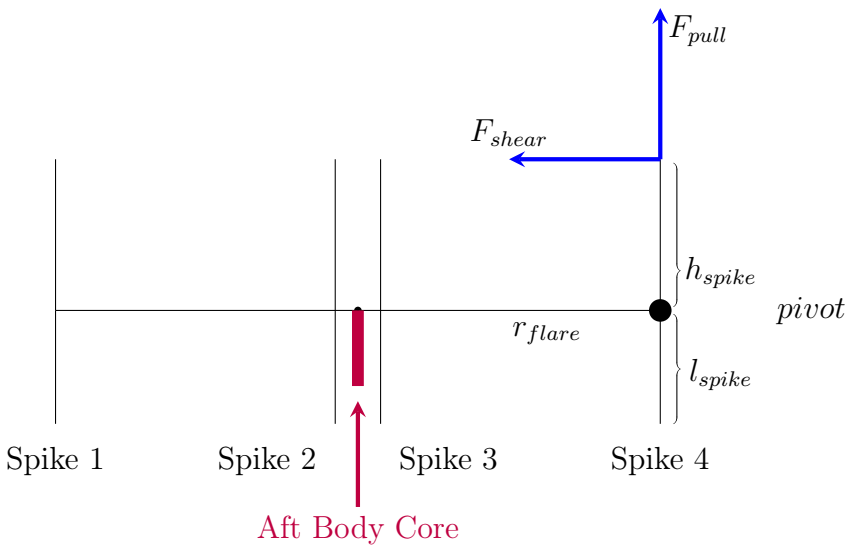


Figure 4-9: Free body diagram illustrating the snow spikes and attached lever arms used to conduct force and moment tests in the field. Static equations are defined around the pivot shown.

field testing of the bent sheet metal design, as shown in Table 4.3.

$$T_{shear2} = T_{shear3} = F_{shear} \left| \sqrt{h_{spike}^2 + r_{flare}^2} \right| \cos \left[\tan^{-1} \left(\frac{h_{spike}}{r_{flare}} \right) \right] \quad \approx 17 \pm 9 \quad \text{N m} \tag{4.3b}$$

$$T_{shear4} = F_{shear} h_{spike} \quad \approx 31 \pm 16 \quad \text{N m} \tag{4.3c}$$

$$T_{pull1} = F_{pull} \left| \sqrt{h_{spike}^2 + (2r_{flare})^2} \right| \sin \left[\tan^{-1} \left(\frac{h_{spike}}{2r_{flare}} \right) \right] \quad \approx 50 \pm 40 \quad \text{N m} \tag{4.3d}$$

where

$F_{pull} \approx 60 \pm 46$ N is the tested mean and standard deviation pull force during field testing of the bent sheet metal design, as shown in Table 4.3.

$$T_{pull2} = T_{pull3} = F_{pull} \left| \sqrt{h_{spike}^2 + r_{flare}^2} \right| \sin \left[\tan^{-1} \left(\frac{h_{spike}}{r_{flare}} \right) \right] \quad \approx 50 \pm 40 \quad \text{N m} \tag{4.3e}$$

$$T_{pull4} \approx 0 \quad \text{N m} \tag{4.3f}$$

$$T_{shearCore} \approx K_{areaMultiplier} T_{pull2} \approx 31 \pm 17 \quad \text{N m} \tag{4.3g}$$

where

$K_{areaMultiplier} \approx 1.8 \pm 0.2$ is the approximate ratio of area of the aft-body core structure to a single bent sheet metal snow spike.

$$T_{pullCore} \approx K_{areaMultiplier} T_{pull2} \approx 100 \pm 80 \quad \text{N m} \tag{4.3h}$$

$$\begin{aligned} T_{opposing} = {} & T_{flare} + T_{shear1} + T_{shear2} + T_{shear4} + \\ & T_{pull1} + T_{pull23} + T_{pull4} + T_{shearCore} + T_{pullCore} \quad \approx 500 \pm 220 \quad \text{N m} \end{aligned} \tag{4.4}$$

$$Margin = \frac{T_{opposing}}{T_{wind}} \quad \approx 2.3 \pm 1.1 \tag{4.5}$$

4.4 As-built Snow Spike Design for Alaska

Based on field test results, a prototype snow spike design was synthesized, as shown in Figure 4-10 for the Alaska field tests detailed in Section 2.7. This design is based on the bent sheet metal design in Figure 4-2 (c), but it incorporates an additional interface which permits the spike section to be replaced without removing the aft-body attachment point. Since the stringer junction at the aft-body attachment point

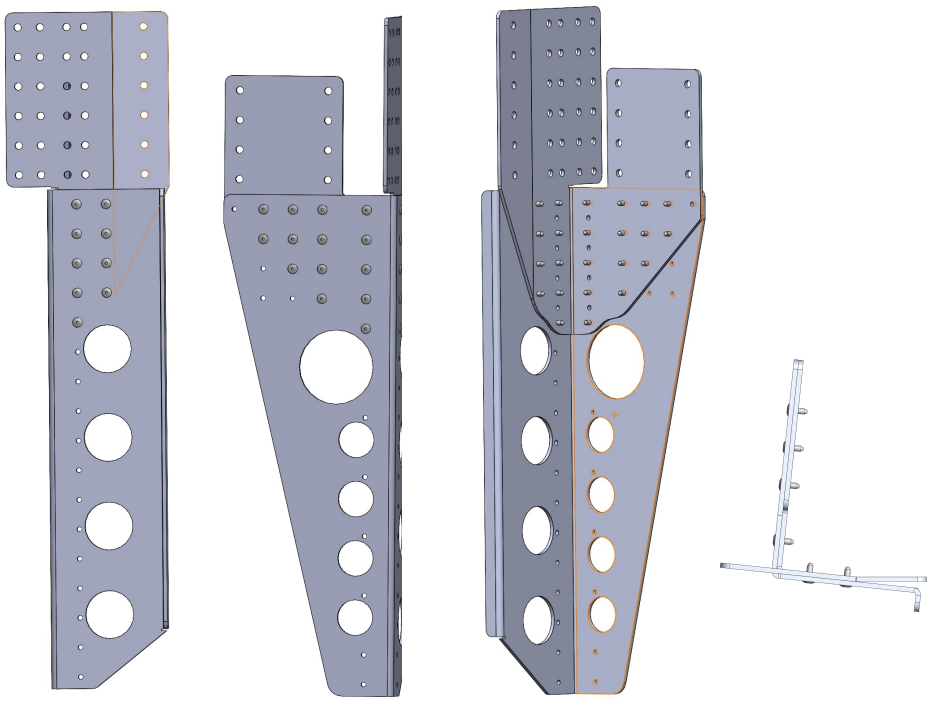
Aft-body mass (kg)	Margin, no flare core, no spikes	Margin, flare core, no spikes	Margin, flare core, small spike	Margin, flare core, sheet metal
15	0.3 ± 0.1	0.9 ± 0.4	1.2 ± 0.5	2.1 ± 1.1
25	0.5 ± 0.2	1.1 ± 0.5	1.4 ± 0.5	2.3 ± 1.1
35	0.8 ± 0.3	1.3 ± 0.5	1.6 ± 0.6	2.5 ± 1.2
45	1.0 ± 0.3	1.5 ± 0.6	1.8 ± 0.6	2.7 ± 1.2
55	1.2 ± 0.4	1.8 ± 0.6	2.0 ± 0.7	2.9 ± 1.3
65	1.4 ± 0.5	2.0 ± 0.7	2.2 ± 0.8	3.1 ± 1.3
75	1.6 ± 0.5	2.2 ± 0.8	3.5 ± 0.8	3.4 ± 1.3

Table 4.5: Margin calculations for SGIP snow spikes, assuming 0.5 m radius from center of flare to structural tipping point.

may bend with impact, this additional interface makes the snow spike system more modular. In addition, this added interface allows spike designs such as those featured in Figure 4-2 (a) and (b) to be mounted in case they are deemed more appropriate for local operating conditions or future manufacturing constraints. Compared to the initial version of the design, additional bends were made in the mounting structure to better conform to the aft-body mounting area.

4.5 Conclusions

This section presents a snow spike design which has been tested on a component level with calculations showing that it meets the requirements for stabilizing the SGIP antenna mast across the complete range of Ross Ice Shelf wind conditions. Using the testing done for snow spikes, the effect of the aft-body core on stability is also quantified, showing that for aft-body mass >55 kg, not including cabling, spikes are not needed to keep the antenna upright. The leading sheet metal Figure 4-2 (c) spike design has sufficient margin to stabilize an aft-body >25 kg in surface winds up to 35 $\mathrm{m\,s^{-1}}$. While the spike design detailed in Figure 4-2 (c) has the best stabilization performance, and was successfully tested on the Juneau Icefield as detailed in Section 2.7, it may contribute to penetrator roll during drop. An alternate design shown in Figure 4-2 (a) also had sufficient performance margin for aft-body



(a) Front view. (b) Side view. (c) Angled rear view. (d) Top view.

Figure 4-10: As-built snow spike design featuring additional detachable interface used in Alaska drop tests.

mass >45 kg, as shown in Table 4.5, and is symmetric, reducing the possibility of causing roll moments during the drop.

For any planetary penetrator of any scale, a similar process may be used to ensure appropriate stability performance. In addition to the entirely passive designs previously discussed, active designs may achieve a significantly higher mass and insertion force efficiency by having a heater which temporarily heats the surrounding snowpack, then turns off to allow for refreezing. This system could be entirely self-contained, and for an application with a known deployment time, would not need any significant electrical interfaces to the rest of the penetrator. Such a design was considered too complex for the first SGIP iterations, but could be considered in the future, particularly for future systems with lower total mass.

Chapter 5

Discussion and Conclusions

5.1 Conclusions

This work presents calculations which predict the impact of an air-dropped ice penetrator into snow, as well as development of a rigid antenna mast and accompanying snow spike system to prevent the mast from tipping in high surface winds. Discussion, limitations and future work of these are discussed in previous respective sections.

5.2 Discussion

5.2.1 Minimum SGIP path to Antarctica

While the as-built SGIP structural prototype has been demonstrated in a successful structural system deployment on the Juneau Icefield, additional testing and verification is required prior to the planned year-long scientific operating deployment in Antarctica. The Juneau prototype drop test did not include batteries, electronics or a seismometer. Using the data presented in Section 2.7, specifications of a seismometer for procurement will be further negotiated with suppliers. Battery modules such as those pictured in Figure 1-4 will be tested using the shock response and impact data from the Alaska drop tests as well. Embedded electronics to manage

battery consumption, read the seismometer and GNSS receiver, cache the data and transmit it will be developed. Minor modifications to the aft-body and mast design can yield a lighter package which is more aerodynamically stable, and modifications to the shear block system may be made to better accommodate angled and rotating impacts.

5.2.2 Proposed System Design Changes

In a full scientific deployment, in-situ sensor data will be most useful with tens to hundreds of deployed sensors; additionally variable snow pack and surface hazards call for a large deployment to ensure that enough units survive to transmit data. While the SGIP as-built prototype was built as a single unit, developing multiple penetrators for widespread glacial deployment will require significant reductions in size, weight, power and mass compared to the current prototype unit. While the existing design can be modified, further system improvements will be accessible with a deeper architectural redesign.

Aft-body Mass

The as-built prototype aft-body section has a mass of 68 kg, much more than the originally planned 25 kg [43]. This makes SGIP much less stable during the drop phase and makes transport, shipping and deployment more labor intensive [37]. The current as-built aft-body serves two primary purposes: a snow-brake to allow the antennas to stay at the surface and a hard aerodynamic structure to slow the terminal velocity. Currently, the size of aerodynamic surface necessary is much larger than the size of the snow brake; by converting these aerodynamic surfaces to a flexible structure like the disk-gap parachute used in ADIOS, a significant mass reduction may be attained [28]. Even without using a parachute, in a one-use deployment of SGIP there is significant allowance for deformation in the aft-body during impact, and outer aerodynamic structures can be allowed to deform more than the inner cabling housings and shear pin block sections. By keeping a rigid center core and intentionally

deformable outer structure, the aft-body may be redesigned in a significantly lower mass form. Communication system restructuring discussed in Section 5.2.2 would reduce the power budget and battery mass, further simplifying the aft-body mass problem for future iterations.

GNSS and Seismometer Sensor Systems

A key feature of the SGIP system design is the inclusion of both a geodesy-grade GNSS receiver and a broadband seismometer payload. Most of the systems design of SGIP revolves around the main seismic payload package, with the seismometer dictating the radius of the fore-body, acceleration and cushioning requirements, large transmission data volume and thus power requirements, as well as drop location selection. In the as-built SGIP prototype, the specification that the SGIP mast be fully rigid in the deployed position is driven by a requirement that the GNSS receiver not sway in wind or other disturbance. A useful systems simplification to the SGIP architecture would be replacing the geodesy-grade GNSS receiver with a consumer-level GNSS receiver, and using the GNSS data only to contextualize the seismic data rather than for geodesy. As shown by the ADIOS architecture, a GNSS-only air-dropped penetrator probe can be smaller and more affordable than SGIP, and having a separate sensor deployment for GNSS can allow for the use of two simpler systems rather than one more complex one [28]. Thus, two lower-cost penetrators would be deployed: a GNSS-only model for geodesy and a seismic model with a consumer-grade GNSS receiver. On the seismic penetrator model, the mast structure may be slightly flexible in the deployed position, opening up significantly lighter and more compact flexible deployable options. Less rigid antenna mast designs can play into a more airplane-deployable architecture as well.

Communication System Restructuring

In the current SGIP architecture, Iridium satellite communications consume around 80 % of the 17.7 kW h power budget. Due to the continuous high-frequency data collection of seismic data that needs to be transmitted, this leads to a power budget

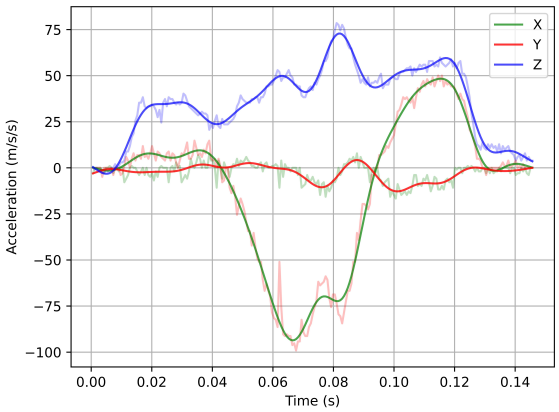
around 20x higher compared to the ADIOS system [28]. The large number of batteries in the as-built system drive the large size and mass of SGIP. To reduce size and mass, the sensor systems may be decoupled from the long-distance communication systems. One possible scheme for this would be a second air-dropped package which has a large parachute to land gently on the ice shelf, containing a large amount of batteries, a local communications radio system and an Iridium transmitter. This base station would receive transmissions from multiple SGIP units over a low-power shorter-range radio and then would relay those data over Iridium to the operations team. Since this relay station would experience significant impact loads, it could be constructed out of simple commercial off the shelf (COTS) components. In potential future deployments to less-remote glaciated areas such as mountain glaciers, this base-station could also be located off of the ice. In a similar theme, an autonomous aerial vehicle such as a consumer drone or a larger plane like SACOS [41] may be used to collect data from SGIP units in the field. This would likely require more software infrastructure to ensure that the SGIP units are ready to transmit when the transient aircraft is overhead but may present a flexible solution for remote areas.

Helicopter to Cargo Airplane

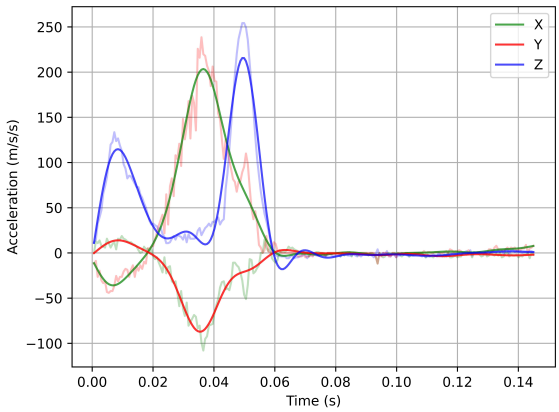
Due to surface hazards, variable snow pack and challenging-to-predict operating conditions, penetrator architectures require many units to reach a robust deployment. To deploy tens to hundreds of SGIP units, the deployment process must be conducted from a cargo plane rather from a helicopter. Towards this end, structural changes to SGIP will be needed to ease deployment. For instance, a stowable aft-body section which unfurls into the aerodynamic and snow-brake configuration using springs mid-air could allow for SGIP to be stored in deployment tubes in a similar method to ADIOS [28]. Additionally, further aerodynamic analysis and testing may be conducted to validate SGIP stability over a wide range of initial angles and wind speeds.

Appendix A

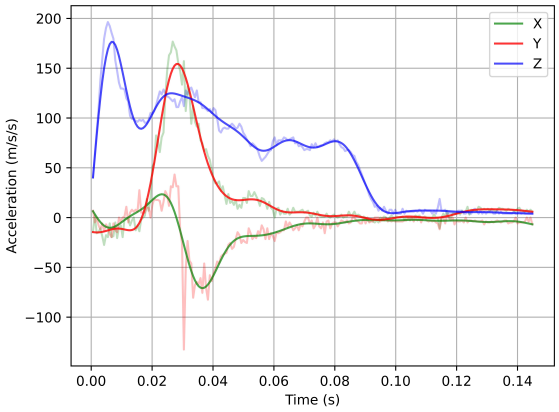
Small Drop Test Plots



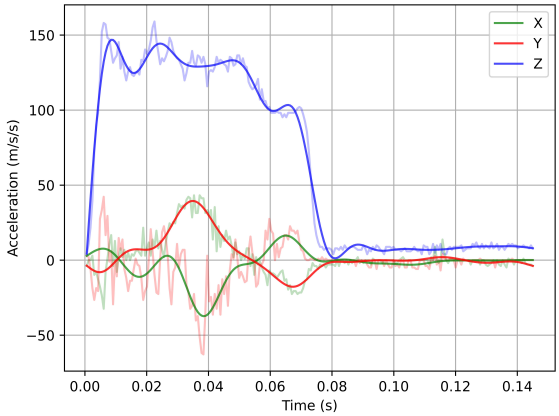
(a) Drop 1



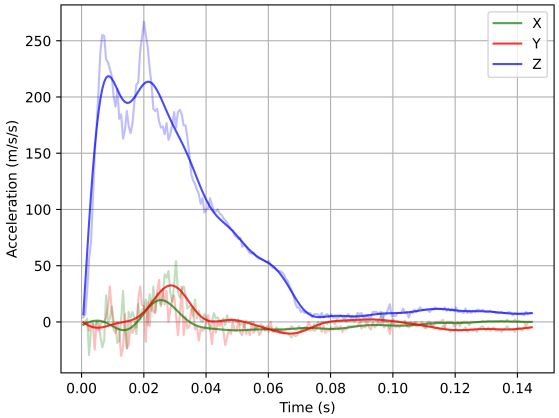
(b) Drop 2



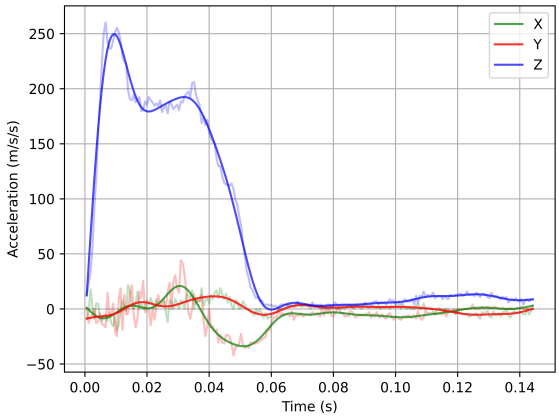
(c) Drop 3



(d) Drop 3

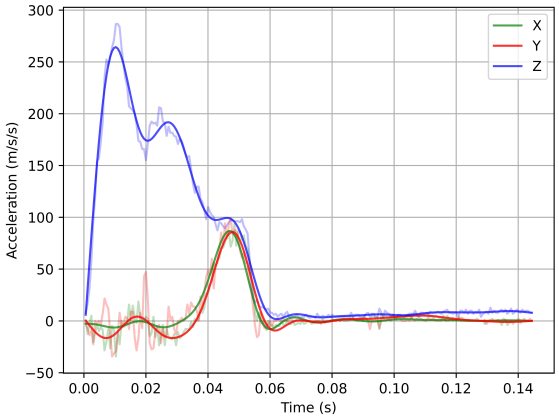


(e) Drop 5

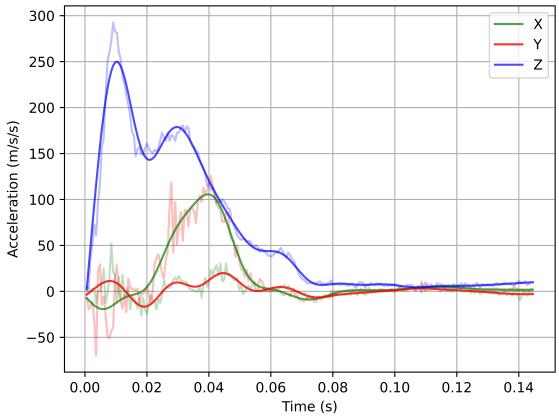


(f) Drop 6

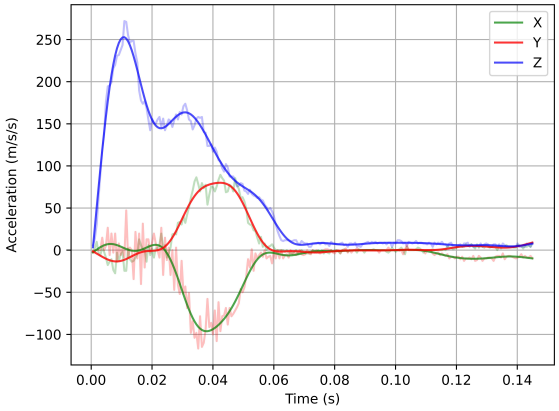
Figure A-1: Example drop test data referencing to Table 2.2.



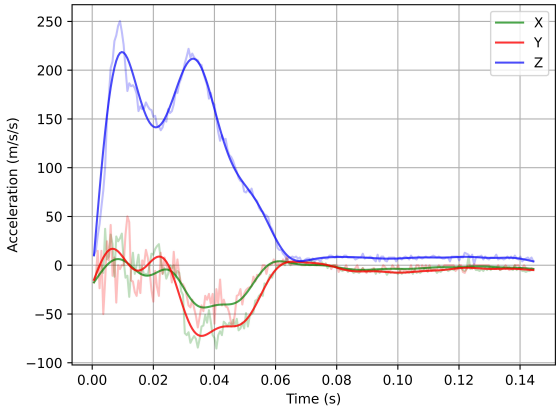
(a) Drop 7



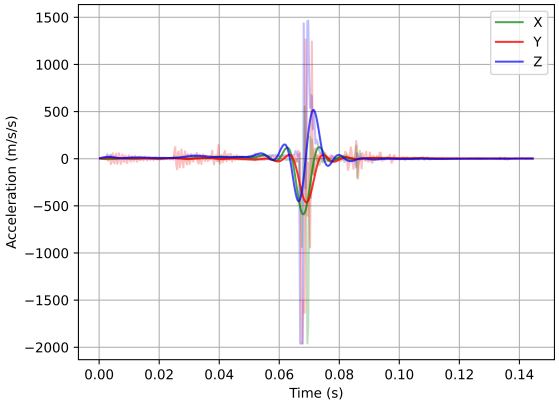
(b) Drop 8



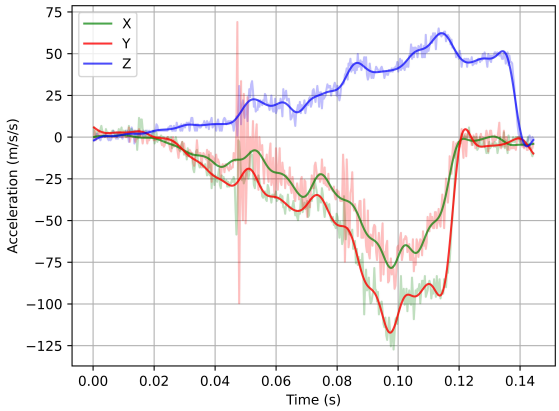
(c) Drop 9



(d) Drop 10

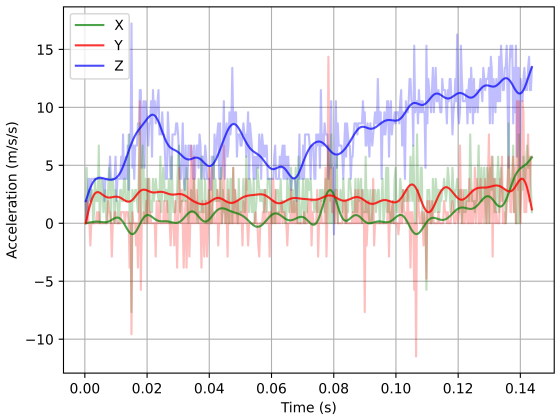


(e) Drop 11

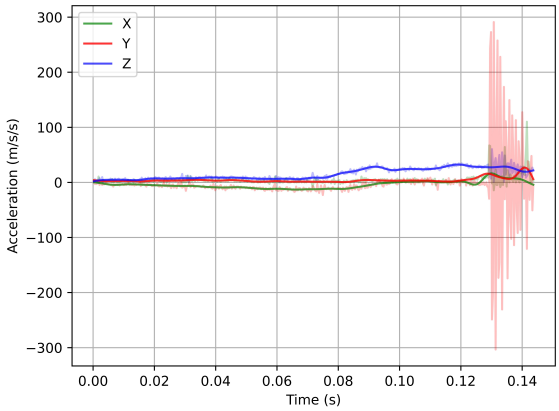


(f) Drop 12

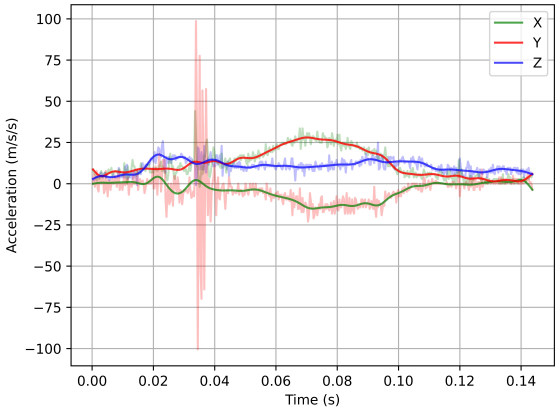
Figure A-2: Example drop test data referencing to Table 2.2.



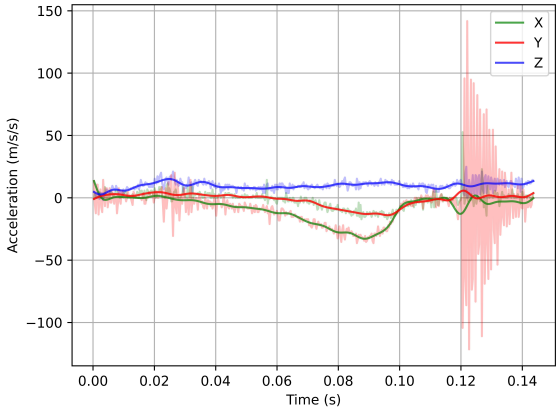
(a) Drop 13



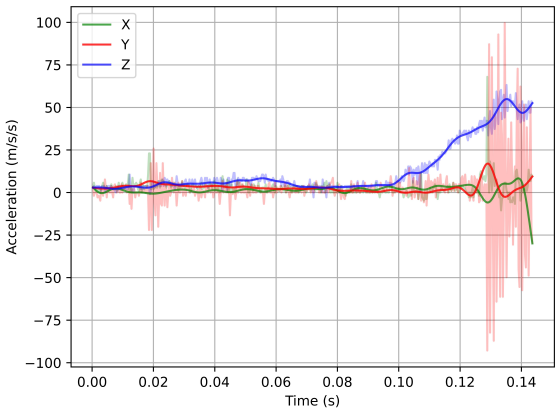
(b) Drop 14



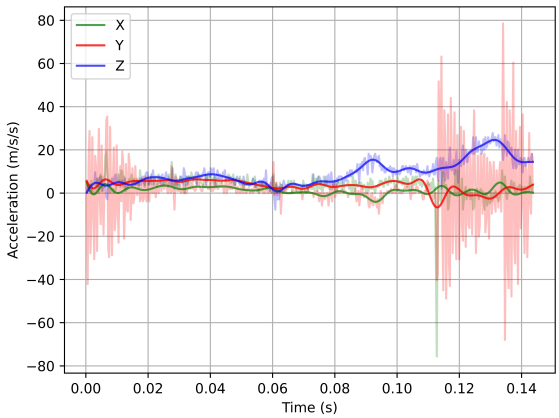
(c) Drop 14



(d) Drop 16

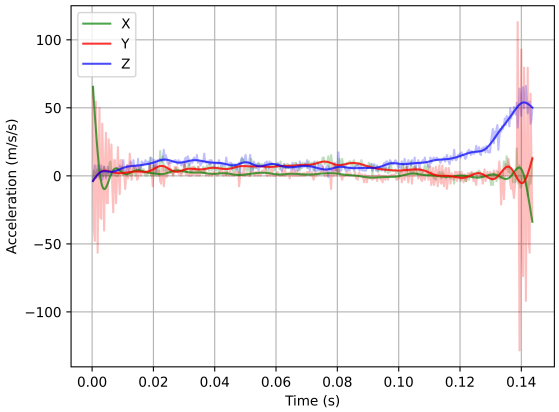


(e) Drop 17

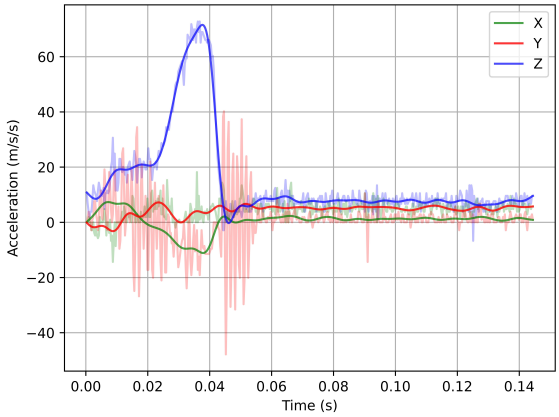


(f) Drop 18

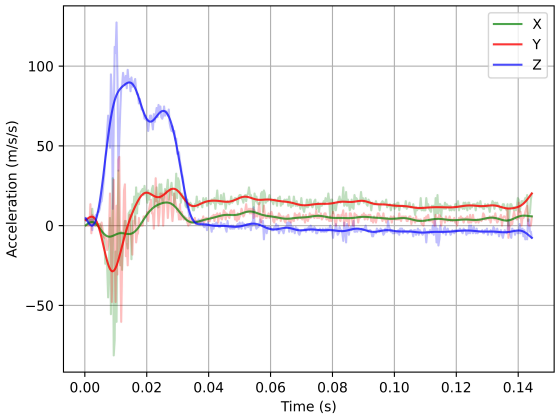
Figure A-3: Example drop test data referencing to Table 2.2.



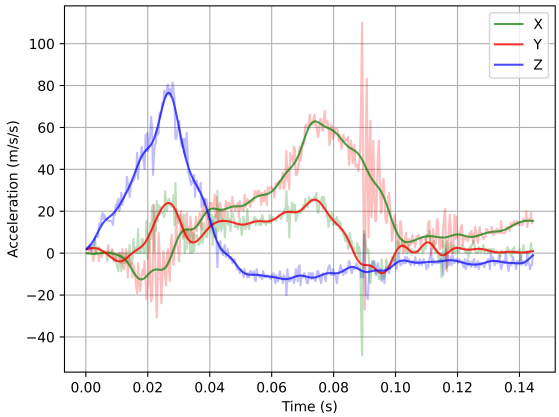
(a) Drop 19



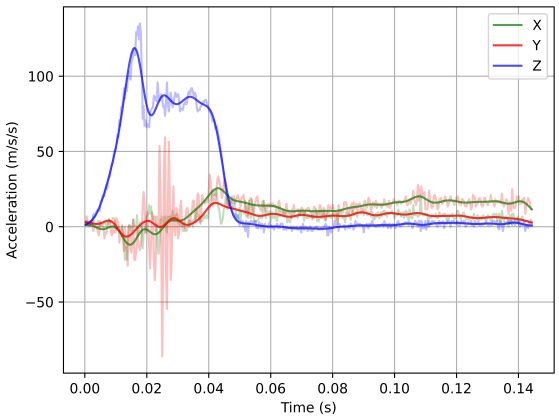
(b) Drop 20



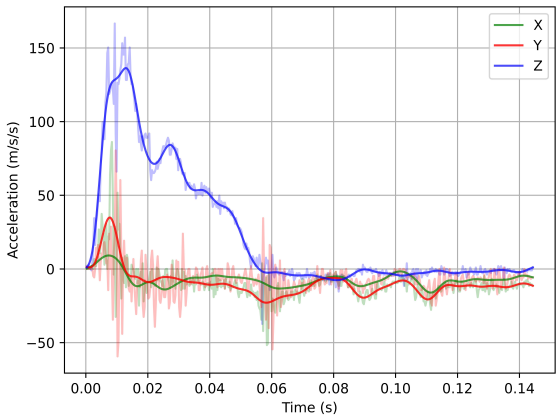
(c) Drop 21



(d) Drop 22

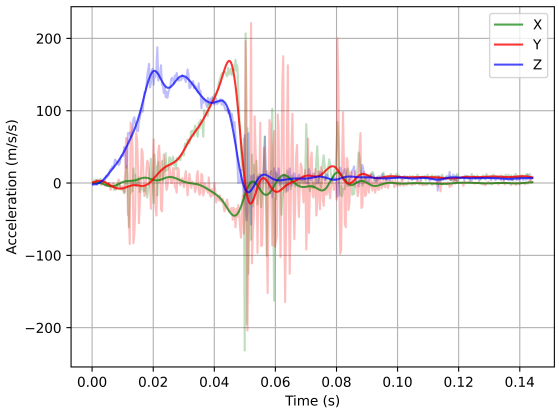


(e) Drop 23

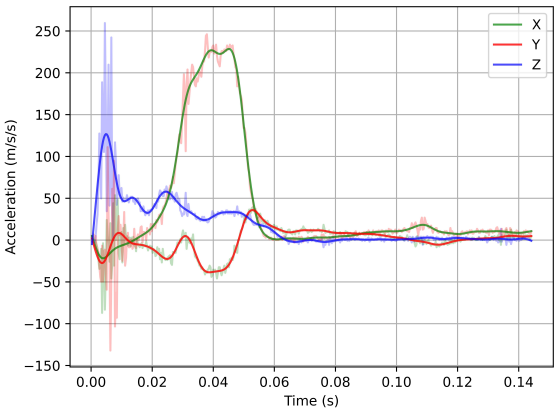


(f) Drop 24

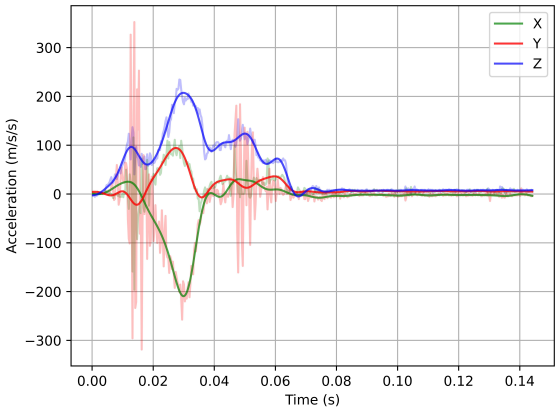
Figure A-4: Example drop test data referencing to Table 2.2.



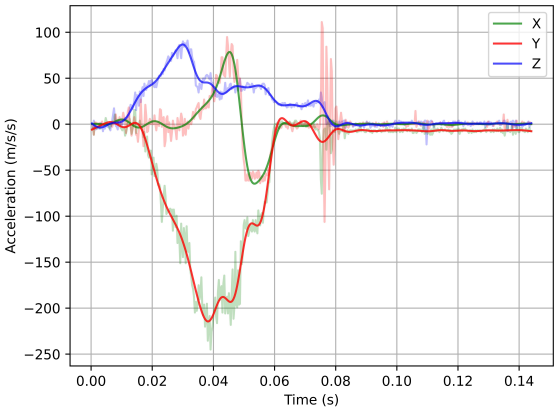
(a) Drop 25



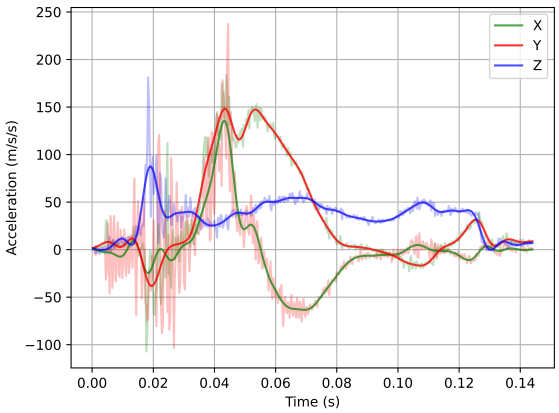
(b) Drop 26



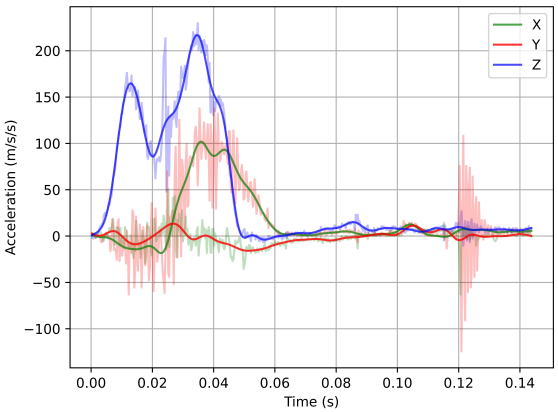
(c) Drop 27



(d) Drop 28

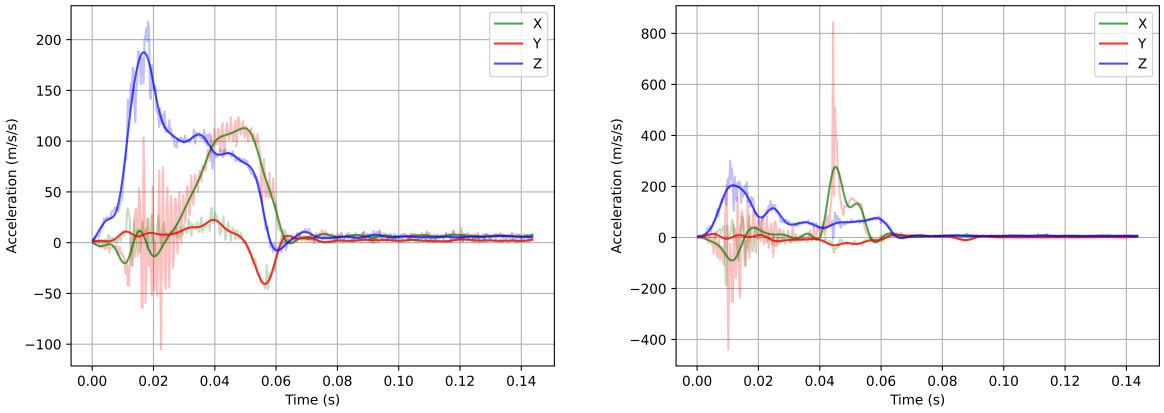


(e) Drop 29



(f) Drop 30

Figure A-5: Example drop test data referencing to Table 2.2.



(a) Drop 31

(b) Drop 32

Figure A-6: Example drop test data referencing to Table 2.2.

Appendix B

Resources

Code for plots presented in this thesis is available at: `https://github.com/MIT-SGIP/impact-mechanics` and `https://github.com/MIT-SGIP/aerodynamics`. Additional questions about this work may be directed to the author at asmiller [at] mit [dot] edu.

Bibliography

[1] G-10 Fiberglass Epoxy Laminate Sheet. URL: https://www.matweb.com/search/datasheet_print.aspx?matguid=8337b2d050d44da1b8a9a5e61b0d5f85.

[2] GNSS Geodetic Antenna. URL: http://www.terrisgps.com/wp-content/uploads/2021/06/topcon-pg-f1-datasheet.pdf.

[3] Minimum Bending Radius. URL: https://www.anixter.com/content/dam/anixter/resources/wire-wisdom/anixter-minimum-bending-radius-wire-wisdom-en.pdf.

[4] Nylon 12 Product Data Sheet, January 2015. URL: https://plastim.co.uk/wp-content/uploads/2019/07/Nylon-12-Technical-Data-Sheet.pdf.

[5] Masterbond EP40 Technical Data Sheet, 2022. URL: www.masterbond.com.

[6] Arden Albee, Steven Battel, Richard Brace, Garry Burdick, Peter Burr, John Casani, Dipprey Duane, Jeff Lavell, Charles Leising, Duncan MacPherson, Wesley Manard, Richard Rose, Robert Sackheim, Al Schallenmuller, and Charles Whetsel. Report on the Loss of the Mars Polar Lander and Deep Space 2 Missions. JPL Special Review Board Report JPL D-18709, Jet Propulsion Laboratory, March 2000.

[7] Robert E. Anthony, Richard C. Aster, Douglas Wiens, Andrew Nyblade, Sridhar Anandakrishnan, Audrey Huerta, J. Paul Winberry, Terry Wilson, and Charlotte Rowe. The Seismic Noise Environment of Antarctica. *Seismological Research Letters*, 86(1):89–100, November 2014. doi:10.1785/0220140109.

[8] Richard C. Aster, Bradley P. Lipovsky, Hank M. Cole, Peter D. Bromirski, Peter Gerstoft, Andrew Nyblade, Douglas A. Wiens, and Ralph Stephen. Swell-Triggered Seismicity at the Near-Front Damage Zone of the Ross Ice Shelf. *Seismological Research Letters*, 92(5):2768–2792, April 2021. doi:10.1785/0220200478.

[9] Jonathan L. Bamber, Richard M. Westaway, Ben Marzeion, and Bert Wouters. The land ice contribution to sea level during the satellite era. *Environmental Research Letters*, 13(6):063008, June 2018. Publisher: IOP Publishing. URL: https://dx.doi.org/10.1088/1748-9326/aac2f0, doi:10.1088/1748-9326/aac2f0.

[10] M. J. Brevoort and U. T. Joyner. Experimental Investigation of the Robinson-Type Cup Anemometer, January 1936. NTRS Author Affiliations: NTRS Report/Patent Number: NACA-TR-513 NTRS Document ID: 19930091586 NTRS Research Center: Legacy CDMS (CDMS). URL: https://ntrs.nasa.gov/citations/19930091586.

[11] P. D. Bromirski, A. Diez, P. Gerstoft, R. A. Stephen, T. Bolmer, D. A. Wiens, R. C. Aster, and A. Nyblade. Ross ice shelf vibrations. *Geophysical Research Letters*, 42(18):7589–7597, 2015. _eprint: https://onlinelibrary.wiley.com/doi/pdf/10.1002/2015GL065284. URL: https://onlinelibrary.wiley.com/doi/abs/10.1002/2015GL065284, doi:10.1002/2015GL065284.

[12] Michael Brown. Mechanical Shock Analysis and Testing of an Air-Dropped Antarctic Ice Penetrator. Master's thesis, Massachusetts Institute of Technology, May 2023.

[13] L. M. Cathles IV, Emile A. Okal, and Douglas R. MacAyeal. Seismic observations of sea swell on the floating Ross Ice Shelf, Antarctica. *Journal of Geophysical Research: Earth Surface*, 114(F2), 2009. _eprint: https://onlinelibrary.wiley.com/doi/pdf/10.1029/2007JF000934. URL: https://onlinelibrary.wiley.com/doi/abs/10.1029/2007JF000934, doi:10.1029/2007JF000934.

[14] J. Chaput, R. C. Aster, D. McGrath, M. Baker, R. E. Anthony, P. Gerstoft, P. Bromirski, A. Nyblade, R. A. Stephen, D. A. Wiens, S. B. Das, and L. A. Stevens. Near-Surface Environmentally Forced Changes in the Ross Ice Shelf Observed With Ambient Seismic Noise. *Geophysical Research Letters*, 45(20):11,187–11,196, 2018. _eprint: https://onlinelibrary.wiley.com/doi/pdf/10.1029/2018GL079665. URL: https://onlinelibrary.wiley.com/doi/abs/10.1029/2018GL079665, doi:10.1029/2018GL079665.

[15] Z. Chen, P. D. Bromirski, P. Gerstoft, R. A. Stephen, W. S. Lee, S. Yun, S. D. Olinger, R. C. Aster, D. A. Wiens, and A. A. Nyblade. Ross Ice Shelf Icequakes Associated With Ocean Gravity Wave Activity. *Geophysical Research Letters*, 46(15):8893–8902, 2019. _eprint: https://onlinelibrary.wiley.com/doi/pdf/10.1029/2019GL084123. URL: https://onlinelibrary.wiley.com/doi/abs/10.1029/2019GL084123, doi:10.1029/2019GL084123.

[16] Gareth S. Collins, Dirk Elbeshausen, Thomas M. Davison, Kai Wünnemann, Boris Ivanov, and H. Jay Melosh. iSALE-Dellen manual. page 2354288 Bytes, 2016. Artwork Size: 2354288 Bytes Publisher: figshare. URL: https://figshare.com/articles/journal_contribution/iSALE-Dellen_manual/3473690, doi:10.6084/M9.FIGSHARE.3473690.

[17] Fastener Components. Plastic materials: FR-4 Plastic Fasteners, October 2015. URL: http://www.fastenercomponents.com/news/fr-4-g10/.

[18] Carol A. Costanza, Matthew A. Lazzara, Linda M. Keller, and John J. Cassano. The surface climatology of the Ross Ice Shelf Antarctica. *International Journal of Climatology*, 36(15):4929–4941, 2016. _eprint: https://onlinelibrary.wiley.com/doi/pdf/10.1002/joc.4681. URL: https://onlinelibrary.wiley.com/doi/abs/10.1002/joc.4681, doi:10.1002/joc.4681.

[19] Mariah Danner. *Cratering Characteristics of the Europa Kinetic Ice Penetrator*. Thesis, 2018. Accepted: 2018-04-24T22:15:43Z. URL: https://digital.lib.washington.edu:443/researchworks/handle/1773/41699.

[20] Annick Dewald and R J. Hansman. A Multidisciplinary Analysis of a Stratospheric Airborne Climate Observatory System for Key Climate Risk Areas. In *AIAA SCITECH 2023 Forum*, National Harbor, MD & Online, January 2023. American Institute of Aeronautics and Astronautics. URL: https://arc.aiaa.org/doi/10.2514/6.2023-2603, doi:10.2514/6.2023-2603.

[21] M. Fulchignoni, F. Ferri, F. Angrilli, A. J. Ball, A. Bar-Nun, M. A. Barucci, C. Bettanini, G. Bianchini, W. Borucki, G. Colombatti, M. Coradini, A. Coustenis, S. Debei, P. Falkner, G. Fanti, E. Flamini, V. Gaborit, R. Grard, M. Hamelin, A. M. Harri, B. Hathi, I. Jernej, M. R. Leese, A. Lehto, P. F. Lion Stoppato, J. J. López-Moreno, T. Mäkinen, J. a. M. McDonnell, C. P. McKay, G. Molina-Cuberos, F. M. Neubauer, V. Pirronello, R. Rodrigo, B. Saggin, K. Schwingenschuh, A. Seiff, F. Simões, H. Svedhem, T. Tokano, M. C. Towner, R. Trautner, P. Withers, and J. C. Zarnecki. In situ measurements of the physical characteristics of Titan's environment. *Nature*, 438(7069):785–791, December 2005. Number: 7069 Publisher: Nature Publishing Group. URL: https://www.nature.com/articles/nature04314, doi:10.1038/nature04314.

[22] Johan Gaume, Alec van Herwijnen, Ted Gast, Joseph Teran, and Chenfanfu Jiang. Investigating the release and flow of snow avalanches at the slope-scale using a unified model based on the material point method. *Cold Regions Science and Technology*, 168:102847, December 2019. URL: https://www.sciencedirect.com/science/article/pii/S0165232X19302149, doi:10.1016/j.coldregions.2019.102847.

[23] Geet George, Bjorn Stevens, Sandrine Bony, Robert Pincus, Chris Fairall, Hauke Schulz, Tobias Kölling, Quinn T. Kalen, Marcus Klingebiel, Heike Konow, Ashley Lundry, Marc Prange, and Jule Radtke. JOANNE: Joint dropsonde Observations of the Atmosphere in tropical North atlaNtic meso-scale Environments. *Earth System Science Data*, 13(11):5253–5272, November 2021. Publisher: Copernicus GmbH. URL: https://essd.copernicus.org/articles/13/5253/2021/, doi:10.5194/essd-13-5253-2021.

[24] B. Gerling, H. Löwe, and A. van Herwijnen. Measuring the Elastic Modulus of Snow. *Geophysical Research Letters*, 44(21):11,088–11,096, 2017. _eprint: https://onlinelibrary.wiley.com/doi/pdf/10.1002/2017GL075110. URL: https://onlinelibrary.wiley.com/doi/abs/10.1002/2017GL075110, doi:10.1002/2017GL075110.

[25] T. S. Hudson, A. F. Baird, J. M. Kendall, S. K. Kufner, A. M. Brisbourne, A. M. Smith, A. Butcher, A. Chalari, and A. Clarke. Distributed Acoustic Sensing (DAS) for Natural Microseismicity Studies: A Case Study From Antarctica. *Journal of Geophysical Research: Solid Earth*, 126(7):e2020JB021493, 2021. _eprint: https://onlinelibrary.wiley.com/doi/pdf/10.1029/2020JB021493. URL: https://onlinelibrary.wiley.com/doi/abs/10.1029/2020JB021493, doi:10.1029/2020JB021493.

[26] Athanasios P. Iliopoulos, John C. Steuben, and John G. Michopoulos. Determination of anisotropic mechanical properties of G-10 composite via Direct Strain Imaging. *Polymer Testing*, 50:64–72, April 2016. URL: https://linkinghub.elsevier.com/retrieve/pii/S0142941815301094, doi:10.1016/j.polymertesting.2015.12.002.

[27] Muhammad Ilyas, Michael H. Meylan, Bishnu Lamichhane, and Luke G. Bennetts. Time-domain and modal response of ice shelves to wave forcing using the finite element method. *Journal of Fluids and Structures*, 80:113–131, July 2018. URL: https://www.sciencedirect.com/science/article/pii/S0889974617307582, doi:10.1016/j.jfluidstructs.2018.03.010.

[28] David H. Jones and G. Hilmar Gudmundsson. Aircraft-Deployable Ice Observation System (ADIOS) for instrumenting inaccessible glaciers. *Journal of Glaciology*, 59(218):1129–1134, 2013. Publisher: Cambridge University Press. doi:10.3189/2013JoG13J112.

[29] N. J. Kinar and J. W. Pomeroy. Measurement of the physical properties of the snowpack. *Reviews of Geophysics*, 53(2):481–544, 2015. _eprint: https://onlinelibrary.wiley.com/doi/pdf/10.1002/2015RG000481. URL: https://onlinelibrary.wiley.com/doi/abs/10.1002/2015RG000481, doi:10.1002/2015RG000481.

[30] Shelley L. Knuth, Gregory J. Tripoli, Jonathan E. Thom, and George A. Weidner. The Influence of Blowing Snow and Precipitation on Snow Depth Change across the Ross Ice Shelf and Ross Sea Regions of Antarctica. *Journal of Applied Meteorology and Climatology*, 49(6):1306–1321, June 2010. Publisher: American Meteorological Society Section: Journal of Applied Meteorology and Climatology. URL: https://journals.ametsoc.org/view/journals/apme/49/6/2010jamc2245.1.xml, doi:10.1175/2010JAMC2245.1.

[31] Andreas Köhler, Michał Pętlicki, Pierre-Marie Lefeuvre, Giuseppa Buscaino, Christopher Nuth, and Christian Weidle. Contribution of calving to frontal

ablation quantified from seismic and hydroacoustic observations calibrated with lidar volume measurements. *The Cryosphere*, 13(11):3117–3137, November 2019. Publisher: Copernicus GmbH. URL: https://tc.copernicus.org/articles/13/3117/2019/, doi:10.5194/tc-13-3117-2019.

[32] Sebastien Lebonnois and Gerald Schubert. The deep atmosphere of Venus and the possible role of density-driven separation of CO2 and N2. *Nature Geoscience*, 10(7):473–477, July 2017. Number: 7 Publisher: Nature Publishing Group. URL: https://www.nature.com/articles/ngeo2971, doi:10.1038/ngeo2971.

[33] Matti Leppäranta, Yan Sun, and Jari Haapala. Comparisons of Sea-Ice Velocity Fields from ERS-1 SAR and a dynamic model. *Journal of Glaciology*, 44(147):248–262, 1998. Publisher: Cambridge University Press. doi:10.3189/S0022143000002598.

[34] S. R. M. Ligtenberg, M. M. Helsen, and M. R. van den Broeke. An improved semi-empirical model for the densification of Antarctic firn. *The Cryosphere*, 5:809–819, October 2011. ADS Bibcode: 2011TCry....5..809L. URL: https://ui.adsabs.harvard.edu/abs/2011TCry....5..809L, doi:10.5194/tc-5-809-2011.

[35] W. F. Lindsey. Drag of cylinders of simple shapes, January 1938. NTRS Author Affiliations: NTRS Report/Patent Number: NACA-TR-619 NTRS Document ID: 19930091694 NTRS Research Center: Legacy CDMS (CDMS). URL: https://ntrs.nasa.gov/citations/19930091694.

[36] Ralph D. Lorenz. Planetary penetrators: Their origins, history and future. *Advances in Space Research*, 48(3):403–431, August 2011. URL: https://linkinghub.elsevier.com/retrieve/pii/S0273117711002146, doi:10.1016/j.asr.2011.03.033.

[37] Aaron Makikalli. Aerodynamic and Thermal Considerations for an Antarctic Ice Penetrator. Master's thesis, Massachusetts Institute of Technology, May 2023.

[38] Takeshi Matsushima, Mikiya Yamashita, Tatsuji Yasuhara, Koh Horiguchi, Hiroki Miyamachi, Shigeru Toda, Masamitsu Takada, Atsushi Watanabe, and Kazuo Shibuya. Observation tests of the Antarctic penetrator on the Mizuho Plateau in JARE-43 summer operation. *Antarctic Record*, 47(3):395–408, November 2003. Publisher: National Institute of Polar Research. URL: http://doi.org/10.15094/00009275, doi:10.15094/00009275.

[39] Daniel McGrath, Louis Sass, Shad O'Neel, Anthony Arendt, Gabriel Wolken, Alessio Gusmeroli, Christian Kienholz, and Christopher McNeil. End-of-winter snow depth variability on glaciers in Alaska. *Journal of Geophysical Research: Earth Surface*, 120(8):1530–1550, 2015. _eprint: https://onlinelibrary.wiley.com/doi/pdf/10.1002/2015JF003539. URL: https://onlinelibrary.wiley.com/doi/abs/10.1002/2015JF003539, doi:10.1002/2015JF003539.

[40] Fatemeh Mehdipour, Ulrike Gebhardt, and Markus Kästner. Anisotropic and rate-dependent mechanical properties of 3D printed polyamide 12 - A comparison between selective laser sintering and multi jet fusion. *Results in Materials*, 11:100213, September 2021. URL: https://www.sciencedirect.com/science/article/pii/S2590048X21000467, doi:10.1016/j.rinma.2021.100213.

[41] Brent M. Minchew, Annick Jade Dewald, R. John Hansman, and Charles L. Werner. Continuous high spatial and temporal resolution remote sensing observations will allow rapid learning of physics from data. AGU, December 2022. URL: https://agu.confex.com/agu/fm22/meetingapp.cgi/Paper/1187627.

[42] M. Pelto, J. Kavanaugh, and C. McNeil. Juneau Icefield Mass Balance Program 1946–2011. *Earth System Science Data*, 5(2):319–330, November 2013. Publisher: Copernicus GmbH. URL: https://essd.copernicus.org/articles/5/319/2013/essd-5-319-2013.html, doi:10.5194/essd-5-319-2013.

[43] Daniel Pekka Poe. *Aerodynamics and Impact Simulation of an Air-Dropped Ice Penetrator*. Thesis, Massachusetts Institute of Technology, June 2021. Accepted: 2022-01-14T15:12:01Z. URL: https://dspace.mit.edu/handle/1721.1/139447.

[44] Martin Pratt, J. Winberry, Douglas Wiens, Sridhar Anandakrishnan, and Richard Alley. Seismic and geodetic evidence for grounding-line control of Whillans Ice Stream stick-slip events: Whillans Ice Stream Stick-Slip Events. *Journal of Geophysical Research: Earth Surface*, 119, February 2014. doi:10.1002/2013JF002842.

[45] A. Richter, D. V. Fedorov, M. Fritsche, S. V. Popov, V. Ya Lipenkov, A. A. Ekaykin, V. V. Lukin, A. Yu Matveev, V. P. Grebnev, R. Rosenau, and R. Dietrich. Ice flow velocities over Vostok Subglacial Lake, East Antarctica, determined by 10 years of GNSS observations. *Journal of Glaciology*, 59(214):315–326, 2013. Publisher: Cambridge University Press. doi:10.3189/2013JoG12J056.

[46] Tessa Robinson. *Europa Kinetic Ice Penetrator System for Hyper Velocity Instrument Deposition*. Thesis, March 2016. Accepted: 2016-04-06T16:29:14Z. URL: https://digital.lib.washington.edu:443/researchworks/handle/1773/35520.

[47] Ted Scambos and Agnieszka Gautier. UK and US polar scientists team up to study Antarctica's "wild card". URL: https://nsidc.org/news-analyses/news-stories/uk-and-us-polar-scientists-team-study-antarcticas-wild-card.

[48] Mark W. Seefeldt, Taydra M. Low, Scott D. Landolt, and Thomas H. Nylen. Remote and autonomous measurements of precipitation for the northwestern Ross Ice Shelf, Antarctica. *Earth System Science*

Data, 13(12):5803–5817, December 2021. Publisher: Copernicus GmbH. URL: https://essd.copernicus.org/articles/13/5803/2021/, doi:10.5194/essd-13-5803-2021.

[49] O. V. Sergienko. Behavior of flexural gravity waves on ice shelves: Application to the Ross Ice Shelf. *Journal of Geophysical Research: Oceans*, 122(8):6147–6164, 2017. _eprint: https://onlinelibrary.wiley.com/doi/pdf/10.1002/2017JC012947. URL: https://onlinelibrary.wiley.com/doi/abs/10.1002/2017JC012947, doi:10.1002/2017JC012947.

[50] Mehdi Setareh, Nicolas Polys, Brett Jones, Felipe Bacim, Bobby Orsa, and Matt Tiller. Buckling of Compression Members::Fundamentals::Knowledgebase::SAFAS, August 2010. Publisher: Virginia Polytechnic Institute and State University. URL: https://www.setareh.arch.vt.edu/safas/007_fdmtl_16_buckling_of_compression_members.html.

[51] Suzanne Smrekar, David Catling, Ralph Lorenz, Julio Magalhães, Jeffrey Moersch, Paul Morgan, Bruce Murray, Marsha Presley, Albert Yen, Aaron Zent, and Diana Blaney. Deep Space 2: The Mars Microprobe Mission. *Journal of Geophysical Research: Planets*, 104(E11):27013–27030, 1999. _eprint: https://onlinelibrary.wiley.com/doi/pdf/10.1029/1999JE001073. URL: https://onlinelibrary.wiley.com/doi/abs/10.1029/1999JE001073, doi:10.1029/1999JE001073.

[52] Wen-Zhan Song, Renjie Huang, Mingsen Xu, Andy Ma, Behrooz Shirazi, and R. Lahusen. Air-dropped Sensor Network for Real-time High-fidelity Volcano Monitoring. pages 305–318, June 2009. doi:10.1145/1555816.1555847.

[53] Reto Stockli, Eric Vermote, Nazmi Saleous, Robert Simmon, and David Herring. The Blue Marble Next Generation - A true color earth dataset including seasonal dynamics from MODIS. *EOS*, 87(5)(49):55, 2006.

[54] Alexey Stomakhin, Craig Schroeder, Lawrence Chai, Joseph Teran, and Andrew Selle. A material point method for snow simulation. *ACM Transactions on Graphics*, 32(4):102:1–102:10, July 2013. URL: https://dl.acm.org/doi/10.1145/2461912.2461948, doi:10.1145/2461912.2461948.

[55] Tom Benson. Shape Effects on Drag. URL: https://www.grc.nasa.gov/www/k-12/VirtualAero/BottleRocket/airplane/shaped.html.

[56] F. Walter, D. Gräff, F. Lindner, P. Paitz, M. Köpfli, M. Chmiel, and A. Fichtner. Distributed acoustic sensing of microseismic sources and wave propagation in glaciated terrain. *Nature Communications*, 11(1):2436, May 2020. Number: 1 Publisher: Nature Publishing Group. URL: https://www.nature.com/articles/s41467-020-15824-6, doi:10.1038/s41467-020-15824-6.

[57] Wen L. Wang. Experimental study of projectile penetration in Ottawa sand at low velocities. *Journal of Spacecraft and Rockets*, 6(4):497–498, April 1969. Publisher: American Institute of Aeronautics and Astronautics. URL: https://arc.aiaa.org/doi/10.2514/3.29692, doi:10.2514/3.29692.

[58] CW Young. Penetration Equations, October 1997. URL: https://www.osti.gov/servlets/purl/562498.

[59] Ali Zolfagharian, Mohammad Reza Khosravani, and Akif Kaynak. Fracture Resistance Analysis of 3D-Printed Polymers. *Polymers*, 12(2):302, February 2020. Number: 2 Publisher: Multidisciplinary Digital Publishing Institute. URL: https://www.mdpi.com/2073-4360/12/2/302, doi:10.3390/polym12020302.